Abstract

Global Analysis of the Biophysical Effects of Deforestation in a Changing Climate

Natalie Marie Schultz

2017

The biophysical effects of land cover change, summarized as changes in albedo, surface roughness, and evapotranspiration (ET), have been shown to be more important in influencing local to regional climate than the changes in biogeochemical processes associated with land cover change. However, uncertainties remain in the understanding of the biophysical effects of land cover change, both in the present climate, and under future climate scenarios. This dissertation investigates the biophysical of drivers of the day and nighttime surface temperature response to deforestation in the present climate, and develops a modeling framework to isolate and evaluate the biophysical effects of land cover change within a global climate model.

There is a general consensus on the broad spatial patterns of the surface temperature response to land cover change, in that deforestation results in localized warming in the tropics and cooling in the high latitudes. However, a diurnal asymmetry exists in the surface temperature response to deforestation (ΔT_S), and the biophysical drivers of those patterns are not well understood. Using satellite observations, reanalysis data, and in-situ measurements, we investigate the day and nighttime drivers of ΔT_S. Our findings confirm that the strongest daytime warming occurs in the tropics, where ΔT_S can reach 6 K and above. In the mid and high-latitudes, the average daytime ΔT_S is 3.1 ± 0.07 and 1.4 ± 0.10 K, respectively. We find that daytime ΔT_S is driven by changes in absorbed solar radiation and the latent heat flux. In contrast to daytime conditions, nighttime ΔT_S is negative over most regions, indicating that open lands are cooler than forests, with the strongest cooling observed at high latitudes (-1.4 ± 0.04 K). We find that the magnitude and spatial pattern of ΔT_S is related to the strength of the nocturnal inversion, which is stronger in

high latitudes and weaker in the tropics. Additionally, nighttime ΔT_S is related to the relative amount of heat stored in forests and open lands during the day.

Quantifying the biophysical effects of land cover change using global climate models has its own set of methodological challenges, including isolating the biophysical effects from model variability or other large-scale atmospheric changes. We modify the sub-grid configuration of the Community Land Model (CLM4.5) such that each plant functional type (PFT) is independent from other PFTs in the same grid cell, allowing for direct comparison of their differing response to the same atmospheric forcing data. In comparing this modified version to the default configuration where all PFTs are situated on a single soil column, we find that the soil column configuration has a significant effect on PFT-level air temperature and surface energy fluxes. We examine the sub-grid difference in air temperature between grass and tree PFTs (ΔT_{GT}), a measure of the effects of sub-grid deforestation and find that the magnitude and spatial pattern of ΔT_{GT} agrees more closely with observations, ranging from -1.5 K in boreal regions to +0.6 in the tropics. We conclude that the separate column configuration provides an opportunity to isolate the effects of land cover change from other forcings and feedbacks in climate model simulations.

There is still substantial disagreement among models when it comes to the regional climate response to land cover change, and calls for rigorous evaluation of land surface models are ongoing. We investigate the sub-grid differences in land surface climatology (e.g. ΔT_S) between PFTs in CLM4.5 as a metric of model performance, and examine whether the accuracy in the representation of individual PFTs translates to the accurate simulation of the climate response of the transition between two land cover types. Our results show that this is not the case, and that small biases in the surface processes of a single PFT can compound into larger errors when examined against different PFTs, highlighting the value of the sub-grid comparison as a model performance tool. Additionally, our results show the importance of model evaluation at sub-daily scales, as daily mean values obscure information about model biases during the day and night.

The modeling framework and metrics developed here can be used to evaluate future model developments. Because CLM and other land surface models calculate surface processes at the PFT-level, model evaluation at this scale is able to identify potential biases at their source, thereby improving both sub-grid and grid-averaged output. In this work, we highlight the utility of sub-grid data for understanding the biophysical effects of land cover change. This sub-grid framework could be applied to future climate scenarios and used to understand how the biophysical effects of land cover change compare to other anthropogenic forcings. Future work will focus on investigating the relative impacts of land cover change and rising greenhouse gas concentrations on local climate, and the response of different land cover types to extreme events.

Global Analysis of the Biophysical Effects of Deforestation in a Changing Climate

A Dissertation

Presented to the Faculty of the Graduate School

of

Yale University

in Candidacy for the Degree of

Doctor of Philosophy

by

Natalie Marie Schultz

Dissertation Director: Xuhui Lee

December 2017

Table of Contents

Acknowledgements

First, I would first like to express my sincere appreciation and gratitude to my advisor, Prof. Xuhui Lee. He encouraged me to think big, and his expert knowledge and guidance gave me the tools and confidence to pursue my research goals. I benefited greatly from his thinking, his teaching, and his advice, all of which inspired me to grow as both a scientist and a person. I feel truly fortunate to have worked with him and learned from him through the course of this PhD program.

I would also like to thank my committee members, Prof. Ron Smith, Prof. Nadine Unger, and Dr. Peter Lawrence for their insightful comments, challenging questions, and encouragement over the years. I owe Dr. Peter Lawrence a special thank-you for giving me the opportunity to broaden my PhD experience by hosting me at NCAR. In our many conversations, his knowledge and enthusiasm inspired me to keep pushing forward. I would also like to acknowledge NCAR Scientists Drs. Dave Lawrence and Keith Oleson for their collaborations and contributions to my dissertation research.

I thank the many fellow students, lab mates, professors, and colleagues who have enriched my time at Yale. I am grateful to have the opportunity to work closely and become great friends with my former lab mate, Dr. Lei Zhao. I would also like to thank Mr. Larry Bonneau for his support, advice, and encouragement over the years.

Last but not least, I need to acknowledge the never-ending support from my family. To my fiancé, Doug Rudolph: thank you for always being there for me, providing love, support, and patience through both the good times and the bad, and for making each day better than the last. To my eternal cheerleaders, my parents, Barb Schultz (“PhD Partner”) and Steve Schultz: thank you for your unconditional support. Without the two of you, I wouldn’t be who or where I am today.

List of Figures

List of Tables

Chapter 1: Introduction

Land cover change influences climate by altering the exchange of CO_2 and other trace gases (*biogeochemical effect*), and through modifications to surface radiation and turbulent fluxes (*biophysical effect*). The biogeochemical effects of land cover change are global in nature because greenhouse gases are well mixed in the atmosphere. In contrast, the biophysical effects of land cover change, which include changes to the surface fluxes of radiation, heat, moisture, and momentum [*Pielke et al., 1998*], are highly localized, with the relative importance of competing biophysical effects varying with geographic location and regional climate. While carbon sequestration and storage are important for global climate change, the biophysical effects of land cover change may be more important in influencing climate at local to regional scales.

The effect of land cover change on climate can be quantified by changes in surface temperature [*Bonan, 2008; Mahmood et al., 2014*]. Generally, the biophysical effects of land cover change can be summarized by changes in (1) surface albedo, (2) surface roughness, and (3) evapotranspiration. Land cover change that leads to changes in these three biophysical processes affects surface temperature in competing ways. Deforestation, a major driver of land cover, reduces evapotranspiration and surface roughness, which increases the surface temperature. On the other hand, deforestation generally increases surface albedo which decreases the surface temperature. The relative importance of these biophysical processes varies geographically, and may amplify or dampen changes in climate caused by greenhouse gas emissions. According to published studies, the consensus is that tropical deforestation has a warming effect on local air temperatures due to the reduction of ET, while boreal deforestation has a cooling effect due to large increases in albedo [*Bala et al., 2007; Betts, 2000; Bonan, 2008; Davin and de Noblet-Ducoudré, 2010; Lee et al., 2011*].

However, uncertainties regarding the spatial pattern and magnitude of the biophysical effects of deforestation remain. In many regards, these uncertainties remain because of methodological constraints. Due to the lack of suitable long-term datasets, many studies have adopted a paired-

site approach to investigate the potential impacts of land cover change using in-situ or satellite observations [*Juang et al.*, 2007; *Lee et al.*, 2011; *Li et al.*, 2015; *N.M. Schultz et al.*, 2017; *Teuling et al.*, 2010]. This type of methodology substitutes space for time, and compares the land surface response of different land cover types exposed to the same or similar atmospheric conditions. This could be two flux towers situated in close proximity to each other, or satellite-derived values of land surface climate from different land cover types within a defined geographical region.

Utilizing global climate models to assess the biophysical effects of land cover change poses its own set of challenges. Traditionally, modeling studies have used paired simulations to evaluate the biophysical effects of historical land cover change: the first simulation run with potential (pre-industrial) vegetation cover and the second simulation with present day land cover. The biophysical effects of land cover change are isolated by prescribing the same concentrations of atmospheric constituents (greenhouse gases and aerosols) with both sets of land cover maps. However, quantifying the impact of the biophysical effects as the difference between two model scenarios is complicated by the other factors, including unforced model variability or non-local effects of large-scale land cover change such as changes to atmospheric or ocean circulation [*Pielke et al., 2011; Pitman et al., 2009*].

Sub-grid information from climate models can be a powerful tool for investigating the biophysical effects of land cover change, yet sub-grid data has been under-utilized in land cover change modeling studies, in favor of grid-averaged output. The sub-grid approach can be considered analogous to the observational space-for-time methodology, in that the land cover change signal is calculated as the difference in climatology between two sub-grid land cover types (plant functional types, PFTs). Utilizing sub-grid information from land surface models allows for the direct comparison of the land surface response of different PFTs to the same atmospheric conditions, either a prescribed atmospheric dataset or a dynamic atmosphere model.

By directing comparing the response of one land cover type to another within the same grid cell, the complicating factors that arise from multiple simulations are removed. Further, the analysis of sub-grid data may be particularly useful in future climate projection simulations to understand how the local biophysical effects of land cover change compare to other large scale forcings, such as rising greenhouse gas concentrations.

There is still substantial disagreement among models when it comes to the regional climate response to land cover change [*Pitman et al., 2009*]. In particular, in context of the Land Use and Climate, Identification of Robust Impacts (LUCID) project, *de Noblet-Ducoundé et al.* [2012] found that there was no consistency among land surface models in their representation of the partitioning of available energy between latent and sensible heat fluxes in response to land cover change. As such, rigorous evaluation of land surface models is needed to develop metrics and diagnostic protocols to quantify model performance when it comes to the simulated response to land cover change [*Lawrence, D.M. et al.,* 2016].

This dissertation seeks to address unanswered questions about the biophysical drivers of the surface temperature response to deforestation in the present climate, and develop a sub-grid modeling framework by which to isolate the biophysical effects of land cover change within a changing climate system. Additionally, it proposes a sub-grid methodology for evaluating the simulated effects of land cover change at a global scale.

This dissertation is organized into three main chapters:

Chapter 2 is guided by the question: What are the biophysical drivers of the day and nighttime surface temperature response to deforestation? Global satellite observations, reanalysis data, and in-situ observations from flux tower sites are used to quantify and compare the relative strength of biophysical effects from a surface energy balance perspective. With particular attention paid to the drivers of the nighttime surface temperature response to deforestation, two hypotheses that

have been proposed for nighttime forest warming are investigated: (1) turbulence in a stably stratified atmospheric boundary layer, and (2) heat release from daytime heat storage.

Chapter 3 is focused on developing a sub-grid modeling framework by which to investigate the biophysical effects of land cover change. The Community Land Model (CLM4.5) represents land surface heterogeneity as a mosaic of sub-grid land cover types. The vegetated fraction of the grid cell contains up to 16 PFTs. By default in CLM4.5, all PFTs share a single soil column, which does not allow the complete separation of the PFTs from one another. Here, the sub-grid configuration of CLM4.5 is modified, so that each PFT is assigned to an individual soil column, making each PFT independent from the other PFTs within the grid cell. The overall objectives of this chapter is to examine the effect of sub-grid configuration on sub-grid and grid-averaged surface air temperature and energy fluxes, and to examine if the modified configuration provides advantages for land cover change experiments.

Chapter 4 proposes a new method for evaluating model performance of the biophysical effects of land cover change. While land surface models are routinely evaluated for each PFT, this chapter proposes utilizing the sub-grid differences in land surface climatology between PFTs as a metric of model performance. It specifically examines whether the accuracy in the representation of individual PFTs translates to the accurate simulation of the climate response of the transition between two land cover types. Further, the model evaluation is conducted at sub-daily scales, and the ability of the model to reproduce the biophysical effects is investigated.

The dissertation concludes with **Chapter 5**, summarizing the major results of this research and discussing future research directions. **Appendix A** reports the preliminary results of the effect of sub-grid configuration on sub-grid land cover change in a coupled model environment, as well as the effects of sub-grid configuration on grid-averaged carbon fluxes and storage.

Chapter 2: Global satellite data highlights the diurnal asymmetry of the surface temperature response to deforestation

Published as: Schultz, N. M., P. J. Lawrence, X. Lee, Global satellite data highlights the diurnal asymmetry of the surface temperature response to deforestation. *J. Geophys. Res. Biogeo.*, 122, 903-917, doi: 10.1002/2016JG003653

Abstract

Uncertainties remain about the spatial pattern and magnitude of the biophysical effects of deforestation. In particular, a diurnal asymmetry in the magnitude and sign of the surface temperature response to deforestation (ΔT_S) has been observed, but the biophysical processes that contribute to day and nighttime ΔT_S are not fully understood. In this study, we use a space-for-time approach with satellite and reanalysis data to investigate the biophysical processes that control the day and nighttime ΔT_S. Additionally, we incorporate flux-tower data to examine two hypotheses for nighttime forest warming relative to open lands: (1) that forests generate turbulence in the stable nocturnal boundary layer, which brings heat aloft down to the surface, and (2) that forests store more heat during the day and release it at night. Our results confirm a diurnal asymmetry in ΔT_S. Over most regions of the world, deforestation results in daytime warming and nighttime cooling. The strongest daytime warming is in the tropics, where the average ΔT_S is 4.4 ± 0.07 K. The strongest nighttime cooling is observed in the boreal zone, where open lands are cooler than forests by an average of 1.4 ± 0.04 K. Daytime patterns of ΔT_S are explained by differences in the latent heat flux (ΔLE) and absorbed solar radiation (ΔK_a). We find that nighttime ΔT_S is related to the strength of the nocturnal temperature inversion, with stronger temperature inversions at high latitudes, and weak inversions in the tropics. Forest turbulence at night combined with stored heat release drives nighttime ΔT_S patterns.

Introduction

Forests influence climate through the exchange of carbon dioxide, energy, and water vapor with the atmosphere [*Bonan*, 2008; *Mahmood et al.*, 2014; *Pielke et al.*, 1998]. Land cover change, in the form of deforestation, alters the terrestrial carbon cycle and surface biophysical processes [*Bala et al.*, 2007]. In contrast to changes in the global carbon cycle, the climate impacts of changes in biophysical processes tend to be more important at the local or regional scale [*Alkama and Cescatti*, 2016; *Bonan*, 2008; *Jackson et al.*, 2008]. The biophysical effects of deforestation influence surface temperature, and include changes in albedo, roughness, and evapotranspiration (ET) [*Lee et al.*, 2011; *Li et al.*, 2015]. On the one hand, forests have a low albedo compared to deforested or open lands, particularly in high latitudes where they can mask the high albedo of snow [*Betts*, 2000]. On the other hand, forests are more efficient at removing heat from the surface due to their larger surface roughness [*Lee et al.*, 2011], and in humid climates, through a higher latent heat flux [*Anderson et al.*, 2011].

Until recently, much of our knowledge about the biophysical effects of deforestation came from sensitivity experiments with global climate models, with one simulation serving as a control against another with contrasting forest cover [e.g. *Lawrence and Chase*, 2010]. Model results tend to agree that the albedo effect dominates at high latitudes, resulting in a local cooling from deforestation, and that a reduction in ET from deforestation in the tropics results in local warming [*de Noblet-Ducoudré et al.*, 2012]. However, there are inconsistencies in the sign, magnitude, and spatial distribution of the biophysical effects between models, some of which may be due to the differences in the parameterizations of different land cover types and the implementation of land cover change in land models [*de Noblet-Ducoudré et al.*, 2012; *Pitman et al.*, 2009]. In particular, the modeling results of deforestation tend to be inconsistent with observations in temperate forests. In contrast to the observational study of *Wickham et al.* [2013], who showed that surface temperature declines as forest extent increases, most models show that temperate

forests are a source of heat relative to other types of land cover. Additional uncertainties may result from the paired simulation approach, in which biophysical effects need to be distinguished from unforced model variability or the non-local effects of land cover change, such as changes to ocean or atmospheric circulation [*Pielke et al.*, 2011]. To remove these additional uncertainties from paired simulations, a sub-grid modeling approach has been proposed as a means to isolate the biophysical effects of deforestation or other land use change within a global climate model [*Malyshev et al.*, 2015; *Schultz et al.*, 2016]. *Winckler et al.* [2017] used a complementary approach to distinguish local vs. non-local effects of land cover change on local climate by selectively changing land surface properties in selected grid cells, while leaving the surrounding grids unchanged.

Observational methods of the biophysical effects are needed to constrain model results, and reduce the uncertainty of model ensembles [*Alkama and Cescatti*, 2016]. Global or regional observational studies of the biophysical effects of deforestation or land use change have used a space-for-time approach, comparing the surface temperature of different land cover types within close proximity to each other, assuming differences in the environmental or atmospheric conditions are negligible [*Lee et al.*, 2011; *Li et al.*, 2015; *Peng et al.*, 2014; *Zhang et al.*, 2014]. An alternative approach was developed to investigate the biophysical climate effects of regions that had recent forest gains or losses [*Alkama and Cescatti*, 2016].

In-situ measurements have shown that the biophysical effects of deforestation on surface air temperature follow a latitudinal pattern. Across North and South America, the temperature effect from deforestation changes from net warming to net cooling around 35^{o} N [*Lee et al.*, 2011]. A similar pattern is observed in East Asia, with net cooling observed in site pairs north of 35.5^{o} N [*Zhang et al.*, 2014]. Interestingly, each of these studies found that a diurnal asymmetry exists in the biophysical effect, and that the diurnal temperature range (DTR) is reduced with forest cover. In northern sites (>45^{o}N), the net cooling from deforestation is driven by minimum temperature

differences, with similar temperatures observed between the open and forest sites during mid-day [*Lee et al.*, 2011; *Zhang et al.*, 2014]. The opposite is true in the tropics (15°S to 20°N), where the net warming from deforestation is largely a result of a difference in maximum air temperature, with similar temperatures observed overnight [*Zhang et al.*, 2014].

One proposed hypothesis for the nighttime warming of forests in high latitudes is that the presence of trees causes turbulence, bringing heat from aloft to the surface during stable atmospheric conditions [*Lee et al.*, 2011]. At night, as the surface cools due to longwave emission, an inversion develops, and the surface layer becomes stable, inhibiting vertical and horizontal mixing. Strong nocturnal inversions are common in dry or desert environments because the radiative cooling is unrestricted, whereas weak inversions are expected under humid or cloudy conditions. As a radiation inversion develops, turbulence is diminished in the mixed-layer, and only roughness-generated turbulence persists near the surface [*Oke*, 1987]. Indeed, it has been shown that wind turbine-enhanced vertical mixing produces local nighttime surface warming [*Zhou et al.*, 2012].

The spatial patterns of the biophysical effects of deforestation and afforestation from satellite data are in general agreement with the in-situ and modeled results [*Li et al.*, 2015]. Satellite data analyses show that the daytime cooling by forests in low latitudes is driven by higher ET, while the daytime warming in high latitudes is driven by a lower albedo [*Li et al.*, 2015; *Peng et al.*, 2014]. Nighttime warming of forests follows a latitudinal pattern, with strong warming in high latitudes, and minimal differences in nighttime temperature between forests and open lands in the tropics [*Li et al.*, 2015]. During the nighttime, albedo is irrelevant and ET is generally negligible, yet observed annual mean nighttime land surface temperature differences are as large as 2 K [*Li et al.*, 2015]. An alternative hypothesis to explain nighttime warming of forests is the release of heat energy stored during the day, related to the low albedo of the forests [*Michiles and Gielow*, 2008; *Peng et al.*, 2014]. *Peng et al.* [2014] found that there was reduced nighttime warming

where forests had a larger ET relative to the excess absorbed solar radiation, suggesting that nighttime warming reflects the release of daytime heat storage.

In this study, our overall goal is to investigate the biophysical drivers of the day and nighttime surface temperature response to deforestation. We extend the work of *Li et al.* [2015] by incorporating reanalysis datasets and in situ observations from flux tower sites into a satellite data-based analysis. We quantify and compare the relative strength of biophysical effects from a surface energy balance perspective. Additionally, as we are particularly interested in exploring the drivers of the nighttime response to deforestation, we investigate two complementary hypotheses that have been proposed for nighttime forest warming: (1) turbulence in a stably stratified atmospheric boundary layer, and (2) heat release from daytime heat storage. To the best of our knowledge, the near surface inversion pattern across latitude, and its relation to land surface temperature, has not yet been investigated.

Methods

Data sources

To investigate the biophysical drivers of the surface temperature response to deforestation, this analysis incorporates global satellite and reanalysis data, as well as measurements from a network of flux towers. For our satellite data analysis, we utilized data products from the Moderate Resolution Imaging Spectroradiometer (MODIS), including MODIS-Collection 5 products of land surface temperature (T_S), land cover classification, latent heat flux (LE), and white-sky albedo (α) from the years 2003-2013 at 1 km resolution. For T_S, we used the 8-day average product (MYD11A2) [*Wan*, 2008] from the Aqua satellite, which contains a daytime (~13:30 local time) and a nighttime (~01:30 local time) measurement, approximating the times of daily maximum and minimum temperatures. We limit our analysis to include only the data that the associated Quality Control (QC) flags indicated to have an average error of ≤ 1 K. The MODIS evapotranspiration (ET) product (MOD16) is calculated as a combination of soil evaporation,

canopy evaporation, and plant transpiration [*Mu et al.*, 2011]. While the land cover type does have a direct influence on the behavior of the MODIS ET, the ET is also strongly constrained by the MODIS fractional photosynthetically active radiation (FPAR), albedo, and leaf area index (LAI) products and by the meteorological inputs from the reanalysis data. White-sky albedo (MCD43B3) was obtained at 8-day intervals, a product from both Aqua and Terra satellites, which has a bias mostly less than 5% [*Schaaf et al.*, 2002]. The MODIS land cover classification (MCD12Q1) is produced on an annual basis. We used the primary classification scheme, defined by the International Geosphere Biosphere Programme (IGBP), which has a typical accuracy across all classes of 75% for a single year [*Friedl et al.*, 2010], to distinguish forests from non-forested pixels. From the 11 years of data, we created a single land cover map, selecting the dominant land cover type across all years as the primary land cover.

Data from the Modern Era Retrospective-Analysis for Research and Applications (MERRA) [*Rienecker et al.*, 2011] include monthly 2 m air temperature and incoming solar radiation at the surface, as well as hourly surface temperature and 10 m air temperature for the years 2003-2013. The MERRA data were downloaded at a spatial resolution of 1/2^{o} latitude by 2/3^{o} longitude. From the hourly data, we used a single hour—01:30 local time, to agree with the overpass time of the satellite observations. Similarly, for integration with the satellite data, the MERRA products were screened to include only clear-sky conditions.

We collected observational data from 32 flux towers in the United States, Canada, Australia, Brazil, and Germany (Table 2.1) from the FLUXNET15 Tier 1 dataset (http://fluxnet.fluxdata.org/data/fluxnet2015-dataset/) and the Ameriflux database [*Baldocchi et al.*, 2001]. Flux tower sites were selected under the criteria that they had at least one year of available data, they had measurements of longwave radiation, and they were situated in a location classified as either grassland or forest. Of these sites, 15 were classified as grassland, and 17 were classified as forest (deciduous, conifer, or mixed forest). With the exception of a single site

(site ID: US-MMS), which has hourly measurements, the flux tower data are reported at 30-minute intervals. From this half-hourly or hourly data, we selected an hour of data (01:00 local time) to coordinate with the satellite observations and reanalysis data. From these 32 sites, we used the longwave radiation components to calculate radiative surface temperature (discussed in more detail in next section), and air temperature above the canopy. Two site pairs, each consisting of adjacent forest and grassland towers, (US-Dk1 and US-Dk2 [*Novick et al.*, 2004; *Pataki and Oren*, 2003]; US-Seg and US-Mpj [*Anderson-Teixeira et al.*, 2011]), were included in these 32 flux sites In addition to these 32 sites, we calculated the 01:00 (LST) above-canopy air temperature gradient for five tower sites (Table S2.1), where air temperature was measured at multiple heights above the canopy (3 forest, 2 grassland).

Site Name	Site ID	Lat (ºN)	Lon (ºE)	Land cover	Γ (K)	Reference
Grasslands						
Rollesbroich	DE-RuR	50.62	6.30	GRA	-1.78	*Post et al.* [2015]
Fort Peck	US-FPe	48.31	-105.10	GRA	-1.82	*Thompson et al.* [2011]
KUOM Turfgrass Field	US-KUT	45.00	-93.19	GRA	-3.45	*Hiller et al.* [2010]
Brookings	US-Bkg	44.35	-96.84	GRA	-1.36	*Gilmanov et al.* [2005]
Canaan Valley	US-CaV	39.06	-79.42	GRA	-2.16	*Wilson and Meyers* [2007]
Vaira Ranch	US-Var	38.41	-120.95	GRA	-1.98	*Xu and Baldocchi* [2004]
Duke Forest - Open Field	US-Dk1	35.97	-79.09	GRA	-2.29	*Novick et al.* [2004]
Sevilleta Grassland	US-Seg	34.36	-106.71	GRA	-2.43	*Anderson-Teixeira et al.* [2011]
Goodwin Creek	US-Goo	34.25	-89.87	GRA	-2.81	*Wilson and Meyers* [2007]
Walnut Gulch Kendall Grasslands	US-Wkg	31.74	-109.94	GRA	-2.99	*Krishnan et al.* [2012]
Audubon Research Ranch	US-Aud	31.59	-110.51	GRA	-2.66	*Krishnan et al.* [2012]
Santarem-Km77-Pasture	BR-Sa2	-3.01	-54.54	CRO	-0.11	*Sakai et al.* [2004]
Fazenda Nossa Senhora cattle ranch	n/a	-10.75	-62.37	GRA	-0.14	*von Randow et al.* [2004]
Sturt Plains	AU-Stp	-17.15	133.35	GRA	-1.22	*Beringer* [2013]
Arcturus Emerald	AU-Emr	-23.86	148.47	GRA	-1.71	*Schroder* [2014]
Forests						

Western Boreal - Mature Black Spruce	CA-Obs	53.99	-105.12	ENF	-0.20	*Jarvis et al.* [1997]
Western Boreal - Mature Aspen	CA-Oas	53.62	-106.2	DBF	-0.70	*Blanken et al.* [1997]
Eastern Boreal - Mature Black Spruce	CA-Qfo	49.69	-74.34	ENF	-1.37	*Bergeron et al.* [2007]
Groundhog River Mixedwood	CA-Gro	48.21	-82.16	MF	-1.30	*Coursolle et al.* [2006]
Sylvania Wilderness Area	US-Syv	46.24	-89.35	MF	0.12	*Tang et al.* [2008]
Willow Creek	US-Wcr	45.81	-90.08	DBF	-0.68	*Davis et al.* [2003]
Univ. of Mich. Biological Station	US-UMB	45.56	-84.71	DBF	-0.75	*Schmid* [2003]
Howland Forest (Main Tower)	US-Ho1	45.2	-68.74	ENF	-0.97	*Hollinger et al.* [2004]
Black Hills	US-Blk	44.16	-103.65	ENF	-1.00	*Wilson and Meyers* [2007]
Silas Little - New Jersey	US-Slt	39.91	-74.6	DBF	-0.89	*Clark et al.* [2010]
Morgan Monroe State Forest	US-MMS	39.32	-86.41	DBF	0.19	*Schmid et al.* [2000]
Missouri Ozark Site	US-MOz	38.74	-92.2	DBF	-0.84	*Gu et al.* [2006]
Duke Forest - Hardwoods	US-Dk2	35.97	-79.1	DBF	-0.70	*Pataki and Oren* [2003]
Walker Branch Watershed	US-WBW	35.96	-84.29	DBF	-0.50	*Wilson and Meyers* [2007]
Chestnut Ridge	US-ChR	35.93	-84.33	DBF	-1.13	*Wilson and Meyers* [2007]
Mountainair Pinyon-Juniper Woodland	US-Mpj	34.44	-106.24	WSA	-1.07	*Anderson-Teixeira et al.* [2011]
Rebio Jaru forest	n/a	-10.07	-61.93	EBF	0.61	*von Randow et al.* [2004]

Table 2.1. The details of the flux tower sites. The surface inversion, Γ, was standardized to 10 m above the displacement height. The Γ was calculated individually for each site, except for the Fazenda Nossa Senhora cattle ranch and the Rebio Jaru forest, where Γ was estimated using the values reported in *von Randow et al.* [2004].

Analysis methodology

We use the space-for-time approach, comparing T_S and the biophysical drivers of the T_S response to deforestation over geographical space, rather than over time (Figure 2.1). We created 0.5º latitude × 0.5º longitude grids, calculating the average T_S, *LE*, and albedo for both forests and open land pixels within each grid. Using the IGBP land cover classification scheme, forests were defined using the five forest classes, while open lands were defined as one of three land cover classes: savanna, grasslands, and cropland/natural vegetation mosaic (Table S2.2). The definition of open land and forest were chosen for ease of presentation of results, and to obtain a broader spatial distribution of grid cells than what would have been available for individual land cover classes. The 0.5º analysis window was chosen as it provided the greatest number of analysis grids with useful data while ensuring similar meteorological influences. Smaller analysis windows reduced down the number of analysis grids that met all the criteria to be included in the final analysis.

We calculated the space-for-time deforestation signal as Δ = open – forest. For all 0.5º × 0.5º grids that contained both forest and open-land cover pixels, we obtained values for day and nighttime ΔT_S (K), ΔLE (W m^{-2}), and Δα (dimensionless). We corrected any elevation biases using the Shuttle Radar Topography Mission (SRTM) Global Digital Elevation Model (DEM) at 1km resolution (SRTMGL30). To remove temperature differences in the 1 km pixels due to elevation differences, all 1 km pixels in the 0.5 degree analysis grid were adjusted to the mean elevation of the analysis grid using an elevation correction. As the environmental temperature gradient with elevation of the analysis grid was unknown, the temperature to elevation relationships were calculated for each land cover type separately and then combined to give a single analysis grid temperature elevation gradient which was applied to each of the pixels for that time period. This prevented assumptions as to the environmental temperature gradients where inversions or complex topography deviated from average climate lapse rates.

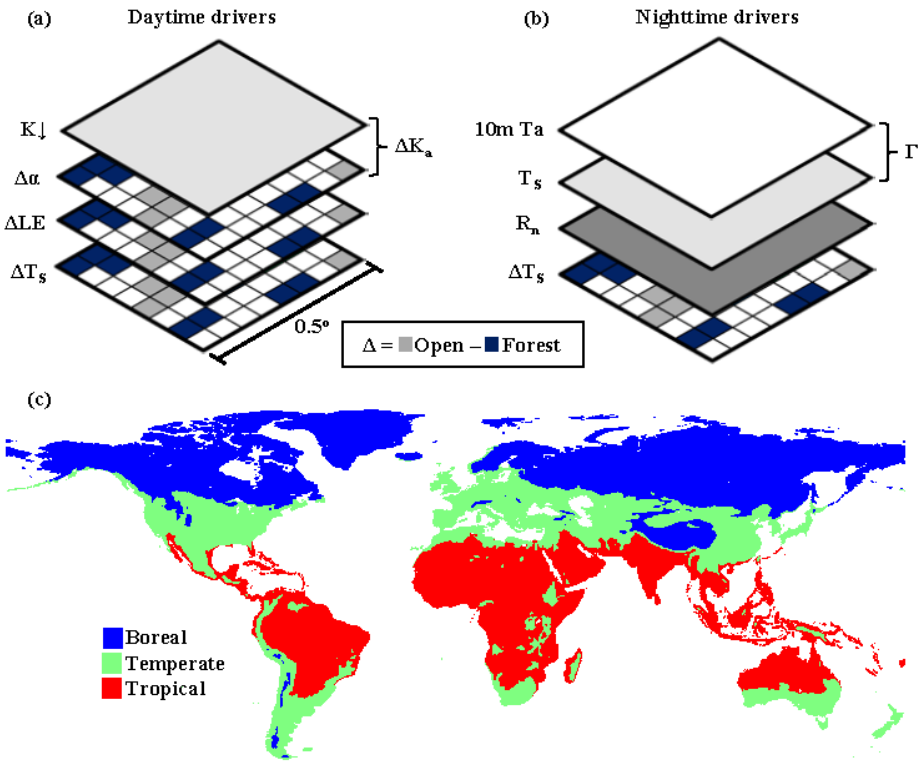

Figure 2.1. A schematic of the data sources used to investigate the (a) daytime and (b) nighttime drivers of ΔT_S, and (c) the geographic extent of the three broad climate zones defined using the MERRA 2 m air temperature data.

The MERRA data was resampled to $0.5^o \times 0.5^o$ to correspond to the satellite data grid resolution. The incoming solar radiation data ($K\downarrow$) was used to calculated the difference in absorbed solar radiation between forests and non-forested pixels ($\Delta K_a = K\downarrow(1 - \Delta\alpha)$). This calculation allows us to directly compare the relative importance of albedo and latent heat flux on ΔT_S. We define a heating potential term as the difference in absorbed solar radiation and latent heat fluxes between open and forested lands ($\Delta H_P = \Delta K_a - \Delta LE$). The ΔH_P combines two daytime drivers, and is a measure of the energy available to warm or cool the surface [*Li et al.*, 2015]. Forests generally have a lower albedo than open lands, absorbing more solar radiation than adjacent non-forested areas. Therefore, a positive ΔH_P indicates that open lands have excess energy compared to forests, and a negative ΔH_P indicates that open lands have a lower energy load compared to forests. Although the ΔH_P does not account for all terms of the surface energy budget, it allows us to directly compare the relative effects of albedo and latent heat flux differences on the surface temperature response to deforestation.

MERRA 01:30 surface temperature and 10 m air temperature were used to calculate the nocturnal surface temperature inversion. We define the surface temperature inversion as the difference between MERRA T_S and 10 m T_a ($\Gamma = T_S$ – 10 m T_a). The 10 m T_a is defined by MERRA as 10 m above the displacement height ($d \approx 2/3h$), where h is canopy height. We also use flux tower observations to calculate the nocturnal surface inversion, using measurements of air temperature above the canopy and surface temperature, calculated from the longwave radiation components,

$$T_S = \left[\frac{L_\uparrow - (1 - \varepsilon)\, L_\downarrow}{\varepsilon\sigma}\right]^{(1/4)} \quad (1)$$

where $L_\uparrow$ and $L_\downarrow$ are the upward and downward longwave radiation fluxes, ε is the surface emissivity (assumed here to be 0.98), and σ is the Stefan-Boltzmann constant (5.67×10^{-8} W m^{-2} K^{-4}). As the measurement height of air temperature at the tower sites varied, we standardized the

air temperature to 10 m above d using the average nocturnal air temperature gradient from the sites in Table S2.1 (for further details, see Supporting Information). The correction of Γ to 10 m above d was small, averaging -0.39 K for grassland sites and 0.34 K for forest sites (Tables S2.3-S2.4).

Finally, as it has been shown that the local response to deforestation depends on background climate [*Li et al.*, 2016; *Li et al.*, 2015; *Pitman et al.*, 2011], we used the monthly 2 m air temperature from MERRA to define three general climate zones (Figure 2.1). We define the boreal zone as grids that have an 11-year average of 2 m $T_a < 3.5$ ^oC. The tropical region is defined with annual 2 m temperatures > 24.0 ^oC. The temperate region is defined as the transitional zone between the tropical and boreal regions, with average annual between 3.5 and 24.0 ^oC. The temperature thresholds were chosen to highlight the differences in the surface temperature response to deforestation across distinct geographical regions, in an analogous method to previous studies that summarize geographical patterns using latitudinal bands [*Lee et al.*, 2011; *Li et al.*, 2015; *Zhang et al.*, 2014]. Our tropical and boreal regions are in general agreement with the tropical (A) and cold (D) climate zones from the Köppen-Geiger climate classification system [*Peel et al.*, 2007]. Although our tropical and boreal zones are farther reaching than the Köppen zones in some regions such as northern Africa and the Tibetan Plateau, we do not include satellite data from those regions because the land cover types that we are examining in this study do not coexist.

Results

Patterns and drivers of daytime ΔT_S

Over most regions of the world, open lands are warmer than forests during mid-day (13:30), with the strongest warming in dry regions (western United States) and in the tropics, where ΔT_S can reach 6 K and above (Figure 2.2a). At high latitudes (> ~50^{o}N) in western North America and

central Asia, open lands are cooler than forests by up to 2 K. The magnitude of zonal mean ΔT_S follows a latitudinal pattern, with strong warming in low latitudes and slight cooling in high latitudes in the northern hemisphere (Figure 2.3a). Averaged across climate zones, the average daytime ΔT_S for the tropical, temperate, and boreal zones is 4.4 ± 0.07, 3.1 ± 0.06, and 1.4 ± 0.10 K, respectively. The parameter bounds here and following represent the 95% confidence intervals of the mean difference in each climate zone. The ΔH_P follows a similar pattern to ΔT_S, with large positive values in tropical regions and negative values at high latitudes (Figure 2.2b). However, the sign of ΔT_S and ΔH_P do not agree in all regions. First, ΔT_S only becomes negative at high latitudes (> ~50^{o}N), whereas ΔH_P changes sign from positive to negative in the temperate region, as low as 20-30^{o}N (Figure 2.3b). Second, in arid or semi-arid regions (i.e. western United States, southern Europe, and the Middle East), there is a large positive ΔT_S, while the ΔH_P is negative.

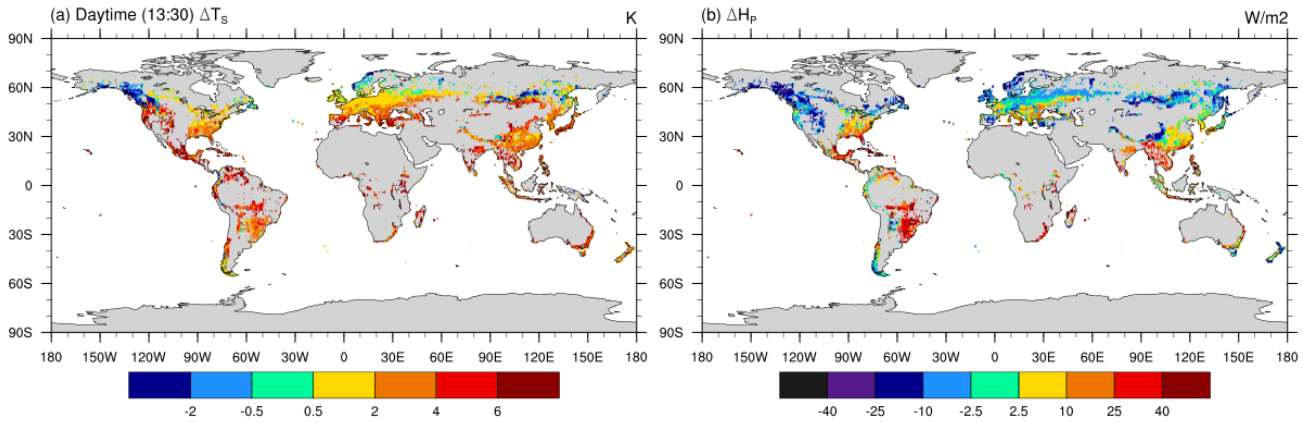

Figure 2.2. The 11-year annual differences (open – forest) in the (a) daytime surface temperature (ΔT_S), and the (b) heating potential (ΔH_P).

Climate zone	13:30 ΔT_S (K)			ΔK_a (W m^{-2})			ΔLE (W m^{-2})			ΔH_P (W m^{-2})		
	annual	JJA	DJF	annual	JJA	DJF	annual	JJA	DJF	annual	JJA	DJF
Boreal	1.4	3.1	-0.9	-13.2	-8.9	-15.9	-6.0	-11.7	0.0	-7.2	2.8	-15.9
Temperate	3.1	3.7	2.0	-7.8	-8.2	-7.9	-14.0	-19.6	-7.3	6.2	11.4	-0.6
Tropical	4.4	4.0	4.2	-5.4	-4.5	-5.9	-38.2	-31.7	-38.1	32.8	27.2	32.2

Table 2.2. Annual mean and seasonal statistics for daytime ΔT_S and drivers.

We can further investigate the pattern of ΔH_P by examining the magnitude and spatial pattern of the difference in absorbed shortwave radiation (ΔK_a) and latent heat flux (ΔLE) separately. Comparing the magnitudes of ΔK_a and ΔLE allows us to determine the relative importance of each biophysical process to the surface energy budget (Figure 2.3c, Figure S2.1). Over most latitudes, the magnitude of ΔLE is larger than that of ΔK_a, showing that although open lands absorb slightly less solar radiation, which would result in relative cooling, their surface cooling through latent heat release is much smaller, resulting in overall warming. The largest contrast between these two biophysical processes is in the tropics, and that difference gradually decreases with latitude. At high latitudes (~50° N/S) ΔK_a becomes more important than ΔLE. Here, the reduction in absorbed solar radiation is the dominant process, leading to a local cooling response to deforestation. Averaged across the climate zones, the annual ΔK_a for the tropical, temperate, and boreal regions is -5.6 ± 0.17, -7.8 ± 0.11, and -13.2 ± 0.22 W m^{-2}, respectively. In the temperate and boreal zones, these differences are amplified during the winter season, because forests mask the high albedo of snow (Table 2.2). The annual ΔLE for the tropical, temperate, and boreal regions is -38.2 ± 0.71, -14.0 ± 0.29, and -6.0 ± 0.17 W m^{-2}. A seasonal cycle exists in ΔLE in the temperate and boreal zones, where the contrast is larger during summer months (Table 2.2).

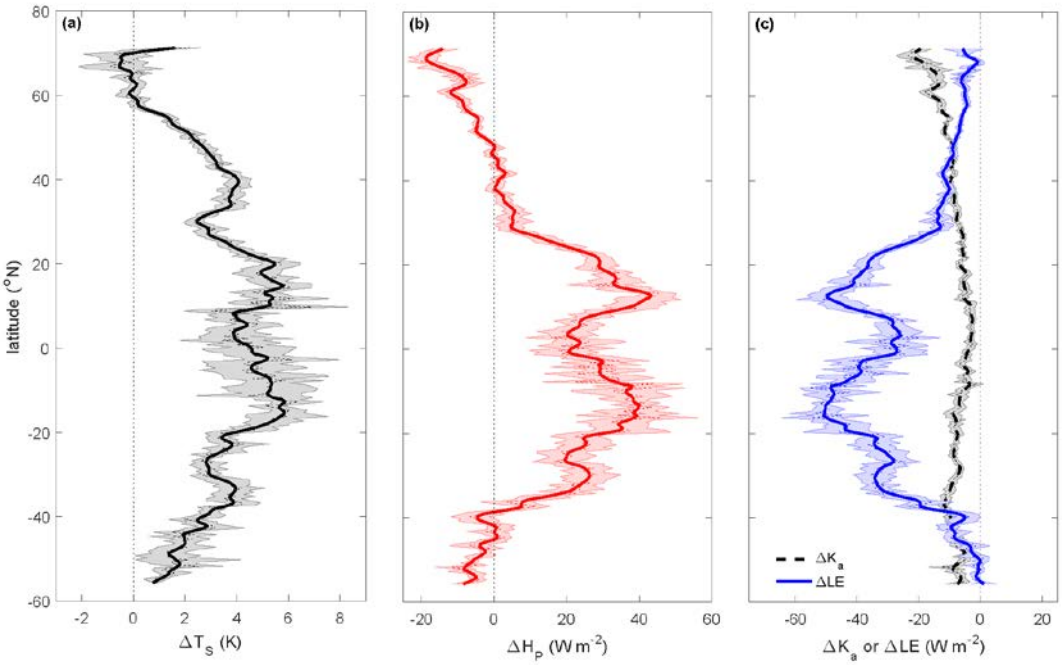

Figure 2.3. The 11-year annual zonal mean of the differences in the (a) daytime surface temperature (ΔT_S), (b) heating potential (ΔH_P), and (c) the absorbed shortwave radiation (ΔK_a) and the latent heat flux (ΔLE). The shaded regions represent the 95% confidence intervals, and for clarity, the thick lines show the running mean of the zonal data.

It is clear that both biophysical processes contribute to ΔT_S, although their relative importance varies geographically. As ΔK_a is a surface warming process and ΔLE is a cooling process, we find that ΔT_S is positively correlated ($R^2 = 0.17$, $p < 0.001$) with ΔK_a (Figure S2.2a) and negatively correlated ($R^2 = 0.22$, $p < 0.001$) with ΔLE (Figure S2.2b). Combining these processes into the single ΔH_P term ($\Delta H_P = \Delta K_a - \Delta LE$) allows us to compare the net effect of these two competing processes. We find that there is a positive relationship between ΔH_P and ΔT_S ($R^2 = 0.27$, $p < 0.001$; Figure 2.4), and it explains the spatial variance in ΔT_S better than ΔK_a or ΔLE alone.

If ΔT_S was only influenced by ΔK_a and ΔLE, then ΔT_S should exactly follow the pattern of ΔH_P: ΔT_S would always be positive where ΔH_P is positive (and vice versa), and the intercept of the regression would go through the origin point. While this significant relationship shows that ΔK_a and ΔLE are major drivers of ΔT_S, the offset of the y-intercept of nearly 2 K from zero indicates the contribution of other surface processes to ΔT_S. Surface roughness is the third biophysical process that is known to influence the surface temperature response to deforestation. The larger aerodynamic roughness of forests allows them to more effectively dissipate sensible heat from the surface to the atmosphere. The 2 K of warming above what the ΔH_P predicts is likely due to differences in surface roughness between the open lands and forests.

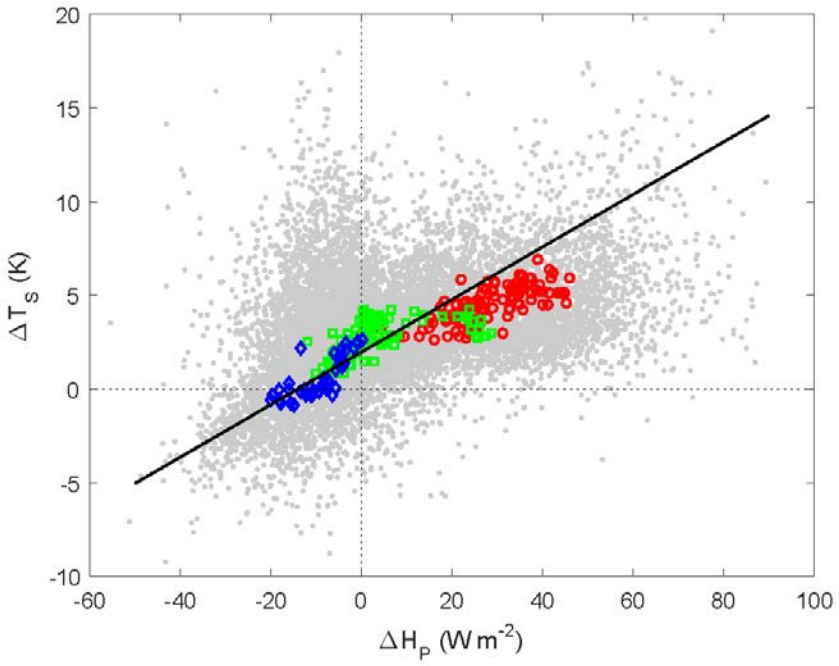

Figure 2.4. The daytime ΔT_S is positively correlated with heating potential ΔH_P (= ΔK_a – ΔLE): y = 0.140 (±0.002) x + 1.973 (±0.01) (R^2 = 0.27, $p < 0.001$). Parameter bounds in the regression are for the 95% confidence intervals. As ΔH_P is a measure of the energy available to heat the surface, a positive ΔH_P indicates that grasslands have more energy to warm the surface than trees (and vice-versa for a negative ΔH_P). If ΔT_S were influenced only by ΔK_a and ΔLE, the intercept of the regression should go through the origin point. The offset of nearly 2 K likely points to the contribution of differences in roughness/convection efficiency between open lands and trees.

Patterns and drivers of nighttime ΔT_S

In contrast to daytime ΔT_S, the nighttime (01:30) ΔT_S is negative over most regions, indicating that open lands are cooler than forests overnight (Figure 2.5a). The strongest cooling is observed at high latitudes (Figure 2.6a). In contrast to high latitudes, a slight warming occurs the tropics. The average ΔT_S across the entire tropical zone is 0.2 ± 0.05 K, while the average nighttime cooling in the temperate and boreal zones is -0.7 ± 0.03 K and -1.4 ± 0.04 K, respectively (Table 2.3). During the night, with no solar radiation and negligible ET, we examine the hypothesis that forests may be warmer at because their larger roughness can generate turbulence in the stable atmosphere, bringing warmer air aloft down to the surface. The nighttime ΔT_S does follow a similar pattern of the surface temperature inversion, Γ (Figure 2.5b, Figure 2.6a). The strength of the inversion ranges from -0.9 ± 0.02 K in the tropical zone to -1.5 ± 0.02 K and -2.3 ± 0.02 K in the temperate and boreal zones, respectively. Nighttime ΔT_S and Γ are enhanced in mid to high latitudes during winter months, with the average ΔT_S reaching -1.9 K and Γ reaching -2.9 K in the boreal zone.

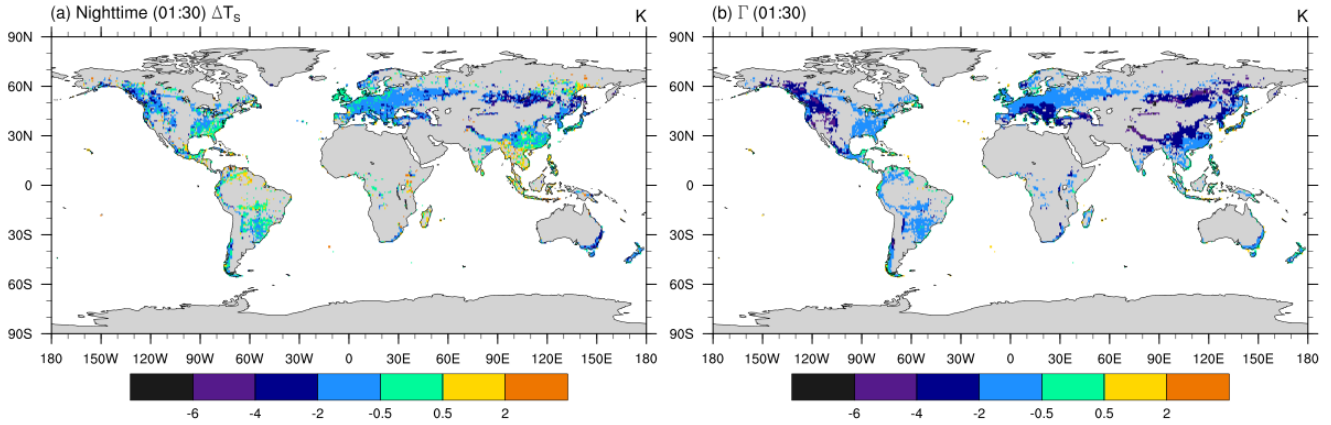

Figure 2.5. The 11-year annual (a) nighttime ΔT_S and (b) surface temperature inversion (Γ, MERRA T_S – 10 m T_a).

	01:30 ΔT_S (K)			Γ (K)			R_n (W m^{-2})		
Climate zone	annual	JJA	DJF	annual	JJA	DJF	annual	JJA	DJF
Boreal	-1.4	-0.8	-1.9	-2.3	-2.0	-2.9	-38.3	-41.9	-32.2
Temperate	-0.7	-0.5	-0.9	-1.5	-1.5	-1.6	-48.8	-49.5	-47.6
Tropical	0.2	0.3	0.2	-0.9	-0.8	-1.1	-43.0	-42.0	-44.6

Table 2.3. Annual mean and seasonal statistics for nighttime ΔT_S and drivers.

In-situ measurements support the latitudinal pattern of Γ (Figure 2.6a). Calculated from flux tower measurements of T_S and T_a (standardized to 10 m above *d*), the Γ above open lands is stronger in high latitudes than it is in the tropics. We choose the sites classified as grassland or cropland for comparison with MERRA in Figure 2.6a because they represent the larger spatial pattern of the nocturnal inversion, unlike forest sites, which according to our hypothesis, may generate turbulence under stable nighttime conditions, thus affecting the nocturnal vertical temperature profile. With the exception of a tower site (US-KUT, lat = 45.0°N, Γ = -3.45 K), the observations of Γ agree relatively well with the MERRA data. However, this outlier may be partially explained by the fact that the measurements were taken over a turfgrass field within a first-ring suburb of a major metropolitan area (Minneapolis – St. Paul, MN, USA) [*Hiller et al.*, 2010]. Surface and air temperature at this site may have been influenced by anthropogenic heat sources including vehicle exhaust and residential heating and cooling systems. The strength of the inversion across these open sites ranges from -0.14 to -2.99 K, if excluding the suburban outlier (Table 1), resulting in a mean Γ of -1.93 K across all sites. In contrast, the surface inversion was much weaker over 17 forest sites, ranging from -1.37 to 0.61 K, resulting in a mean Γ of -0.66 K (Table 2). This shows that averaged across similar latitudes, site measurements support the hypothesis of forest warming via enhanced vertical mixing of a stable nighttime atmosphere. Further, within this network of flux towers, we collected two "site pairs", each consisting of a set of a forest site and a grassland site, situated in close proximity of each other. Each of these site pairs can be expected to be exposed to similar atmospheric conditions. For the site pair in North Carolina, USA (Dk1 and Dk2), we found that the Γ (standardized to 10 m above *d*) above the open and forested sites was -2.52 and -0.73 K, respectively. For the pair in New Mexico, USA (Seg and Mpg), the Γ for the open and forested sites were -2.62 and -1.07 K (Figure S2.3).

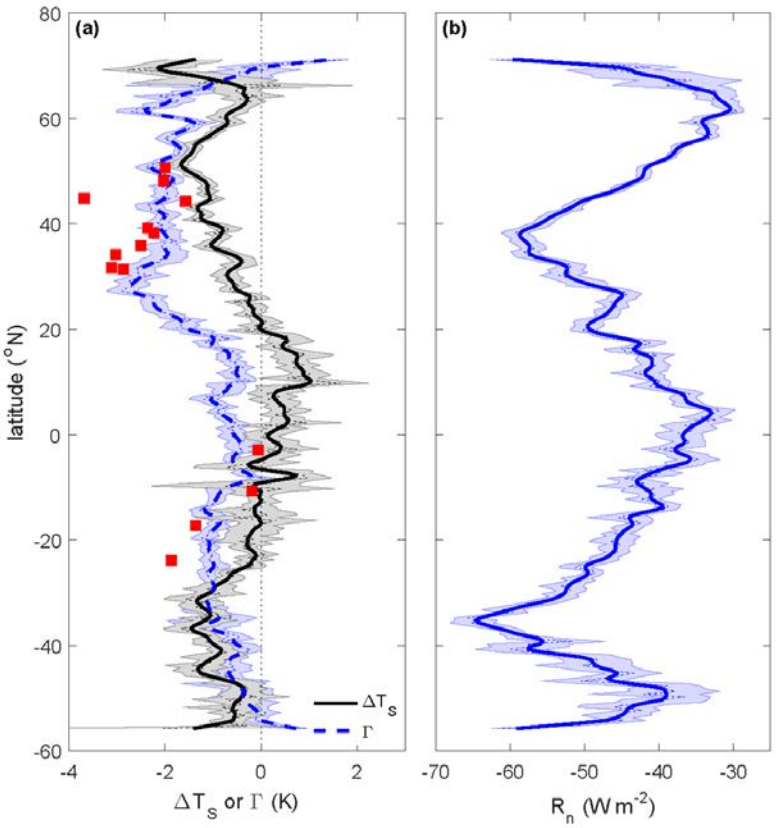

Figure 2.6. Annual (11-year) zonal means for (a) nighttime ΔT_S and inversion strength Γ, and (b) net radiation, $R_n = L\uparrow - L\downarrow$ The shaded regions represent the 95% confidence intervals, and the thick lines show the running mean of the zonal data. The red squares in (a) display the Γ, standardized to 10 m above the displacement height, from the grassland flux tower sites.

There is a positive relationship (R^2 = 0.14, p < 0.001) between Γ and nighttime ΔT_S (Figure 2.7a). That the most pronounced surface cooling from deforestation is correlated with strong nighttime surface temperature inversions supports the hypothesis that forests are warmer at night because of enhanced turbulence over forest canopies. The contrast between the magnitudes of warming observed in the tropics compared to higher latitudes relates to the relative strength of the temperature inversion between those regions. The zonal pattern of the nighttime net longwave flux (R_n – the difference between outgoing longwave radiation at the surface and incoming longwave radiation) indicates increased radiative cooling in the sub-tropics (~30-40° N/S) (Figure 2.6b). The zonal mean pattern of nighttime R_n follows that of the Hadley cell circulation. We hypothesized that patterns of R_n would drive the nighttime temperature inversion and ΔT_S, and although there is a positive relationship between R_n and ΔT_S (geometric mean regression: y = 0.122x (±0.002) + 4.602 (±0.08), p < 0.001), there is significant scatter around the regression line, resulting in an R^2 of < 0.01 (Figure S2.4).

There is also a positive relationship (R^2 = 0.19, p < 0.001) between ΔH_P and nighttime ΔT_S (Figure 2.7b). While ΔH_P is only a proxy of heat storage, this significant correlation indicates that heat storage during the day contributes to nighttime warming of the land surface. Forests in the boreal region absorb and store more energy than open lands, and the release of this heat during the night causes the forests to be warmer than the open lands. However, the amount of excess heat stored in open lands in the tropics is larger than the heat storage deficit of open lands in the boreal zone. Despite this, nighttime ΔT_S in the tropics in minimal. This shows that daytime heat storage alone cannot fully explain the spatial patterns of nighttime ΔT_S, and highlights the additional influence of forest-generated turbulence on nighttime ΔT_S patterns. Together, using multiple linear regression, Γ and ΔH_P explain 26% of the spatial variance in nighttime ΔT_S (R^2 = 0.26, p < 0.001).

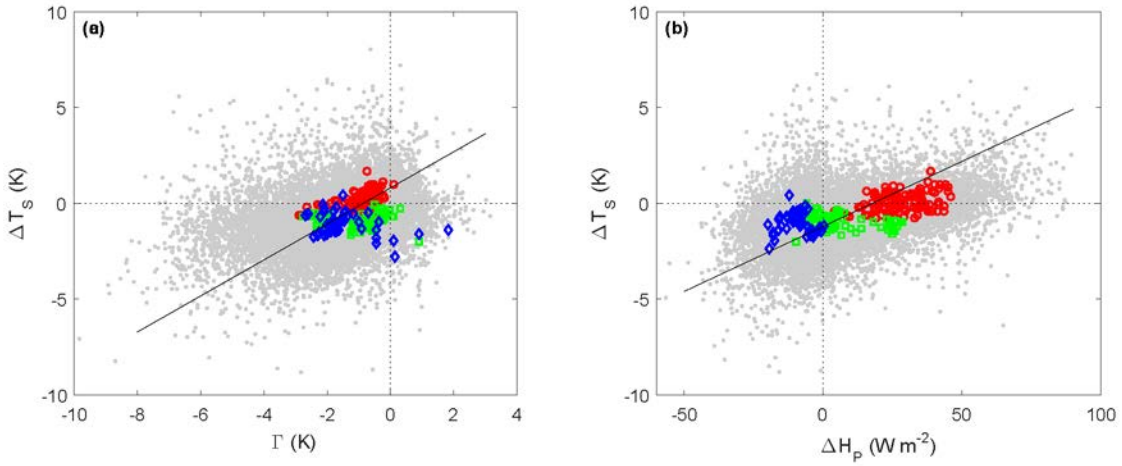

Figure 2.7. The nighttime ΔT_S is positively correlated with (a) the inversion strength Γ and (b) the heating potential ΔH_P. All data points in (a) and (b) are shown as the gray dots, while the zonal means of each climate zone are shown as the red circles (tropical), green squares (temperate), and blue diamonds (boreal). The black solid lines in (a) $y = 0.941$ (± 0.014) x - 0.806(± 0.023) ($R^2 = 0.14$, $p < 0.001$) and (b) $y = 0.068$ (± 0.001) x – 1.208 (± 0.006) ($R^2 = 0.19$, p < 0.001) represent the geometric mean regression for all sample grids (gray dots) Parameter bounds in the regression are for the 95% confidence intervals.

Discussion

This study builds upon the works of others who have used regional and global satellite observations to explore the surface temperature response to deforestation or afforestation [*Alkama and Cescatti*, 2016; *Li et al.*, 2015; *Peng et al.*, 2014]. Our goal was to examine the biophysical processes that drive day and nighttime ΔT_S, using global satellite data in coordination with reanalysis and flux tower observations. Of particular interest in this study was to investigate two hypotheses for the relative nighttime warming of forests compared to open lands: (1) that the larger roughness of forests generates turbulence which brings warm air aloft down to the surface, and (2) that the lower albedo of forests contributes to increased heat storage, which is then released at night. This is the first study to investigate the global pattern of the nocturnal surface inversion, and its relation to surface temperature and nighttime ΔT_S.

Our results highlight the diurnal asymmetry in the magnitude and sign of the surface temperature response to deforestation. In the tropics, daytime warming dominates the overall warming signal from deforestation, with minimal difference in surface temperature at night. In contrast, the nighttime ΔT_S dominates the overall pattern of the surface cooling response to deforestation in the boreal zone. These results show the importance of both daytime and nighttime measurements to understand the drivers behind the surface temperature response to deforestation.

Although tropical forests have a lower albedo and therefore absorb more solar radiation than adjacent open lands, they are able to access soil water and maintain a consistent latent heat flux even during a prolonged dry season [*von Randow et al.*, 2004], which results in lower surface temperatures. Our results are in general agreement with *Li et al.* [2015], who showed that the ET of tropical forests is greater than that of open areas by up to 500 mm/year. Climate models tend to agree that deforestation in the tropics results in a reduction in the latent heat flux [*Lawrence and Chase*, 2010; *Snyder et al.*, 2004]; however, due to the varying implementation and physical representation of land use and land cover change in models, there are inconsistencies in the

partitioning of energy into latent and sensible heat fluxes across the annual cycle [*de Noblet-Ducoudré et al.*, 2012].

Previous work has suggested that nighttime warming of forests is largely due to the release of daytime heat storage [*Peng et al.*, 2014]. The energy storage rates of forests can comprise a significant portion of net radiation; however, the largest energy storage rates occur during sunrise and sunset, and during rainy or cloudy periods [*Michiles and Gielow*, 2008]. The larger biomass and moisture content of forest canopies would increase the heat capacity of forests, slowing down their cooling rate overnight. However, comparative measurements over a tropical forest and pasture showed that storage rates between a tropical forest and pasture were similar at approximately 01:30 (the time of MODIS overpass) [*von Randow et al.*, 2004]. These results are in line with *Bastable et al.* [1993], who compared the available energy at a tropical forest and clearing site, finding that the difference in available energy (including the change in heat storage) between the sites at 01:00 was approximately 10 W m^{-2} during the dry season and negligible during the wet season. While forest canopies may have a higher moisture content than grasslands, soil water storage is higher in tropical grasslands than under forest canopies. *von Randow et al.* [2004] found that in the upper 2 m of soil, water storage was similar under the tropical forests and pasture sites. In the deeper layers (2-3.4 m), forest soil water storage decreased during the dry season, while the water content under the pasture remained relatively constant. Further, measurements show nighttime canopy heat storage rates in a boreal aspen forest of less than 10 W m^{-2} [*Blanken et al.*, 1997], and nighttime storage rate differences of only 3.1 W m^{-2} between forests and open lands at a boreal site cluster in Saskatchewan [*Lee et al.*, 2011].

Our results here show that despite a large positive ΔH_P in the tropics (32.8 W m^{-2}), the nighttime surface temperature difference between open lands and forests is close to zero. In the boreal zone, the ΔH_P is negative (-7.2 W m^{-2}), although to a lesser magnitude than the tropical ΔH_P. Yet,

the open lands are 1.4 ^{o}C cooler than forests at night. All together, these results indicate that the daytime surface energy load is not the only process contributing to nighttime ΔT_S patterns. We found a statistically significant relationship between the nocturnal surface inversion strength and nighttime ΔT_S. This suggests that forests are able to generate turbulence in the stable nighttime atmosphere, bringing heat aloft to the surface, as was shown for wind turbines in Texas [*Zhou et al.*, 2012]. It should be noted that our results here only examine the relationship between ΔT_S and Γ under clear-sky conditions. The presence of clouds would result in increased downwelling longwave radiation, heating the surface and the overlying air. Thus, we would expect to see a reduction in the relative nighttime warming of forests under cloudy conditions. However, additional research would be needed to examine this hypothesis. In situ measurements from flux tower sites also show that the surface inversion is weaker over forest canopies and stronger over grassland sites. We found a statistically significant relationship between the nighttime ΔT_S and net radiation ($R_n = L\uparrow - L\downarrow$). We hypothesized that the latitudinal surface inversion pattern is related to the zonal pattern of $L\downarrow$. This theory is supported by the results of *Li et al.* [2016] who showed a decreasing pattern of $L\downarrow$ from the tropics to higher latitudes, where $L\downarrow$ was approximately 50 W m^{-2} near the equator and 25 W m^{-2} at 60^{o}N. Indeed, the combination of both daytime heating and the surface inversion strength was able to better explain the spatial variations in nighttime ΔT_S than either of these drivers alone.

It is interesting to note that while increased vertical mixing and heat release are both processes that contribute to the warmer nighttime temperature of forests, tropical forests are actually slightly cooler than open lands in some tropical areas (~10 – 20^{o}N). Although over mid to high latitudes, the nighttime ET flux and the difference in ET between forests and open lands is minimal, *Li et al.* [2015] showed that tropical forests maintain a higher ET than open lands at night on average by approximately 50 mm year^{-1}. While this is an order of magnitude less than the daytime difference in ET (~500 mm year^{-1}), the location of the increased nighttime ET flux

occurs directly within the region where we observe the nighttime cooling of forests relative to open lands. This persistent nighttime ET flux may be a potential reason why we observe that open lands are actually warmer than some tropical forests at night.

Our results underscore the importance of the biophysical effects of land cover change on climate. The spatial pattern and magnitude of ΔT_S are largely in agreement with previous empirical satellite data studies [*Li et al.*, 2015; *Peng et al.*, 2014]. It should be noted, however, that this study focuses on the "potential" impact of deforestation. As these results represent a slice of time, they present the impacts from hypothetical land use change around the world. A recent study by *Li et al.* [2016] compared the potential impacts of deforestation on surface temperature (using a methodology similar to the one used in this study) with the actual impacts, finding that the actual impact of deforestation in most regions is very similar to the potential impact, both in terms of sign and latitudinal pattern. *Alkama and Cescatti* [2016] examined the effects of actual deforestation on surface air temperature, inferred from MODIS LST, between 2003 and 2012, and found that the biophysical effects of forest clearing produced large increases in the annual mean maximum air temperature, and slight changes to minimum temperatures. Overall, mean warming occurred across most regions, with the exception of high latitudes. They also found that the sensitivity of surface temperature to land cover change (i.e. forest loss) was 50% greater than it was for air temperature, likely due to the satellite retrievals being limited to clear sky conditions [*Alkama and Cescatti*, 2016].

To the best of our knowledge, the role of vertical mixing in the nighttime warming of forests has not been investigated using a modeling approach, although a similar mechanism has been reported for the urban environment [*Wouters et al.*, 2013]. The results of climate modeling studies regarding the role of land cover change on local climate are generally averaged over daily timescales or longer. *Vanden Broucke et al.* [2015] highlight the importance of distinguishing between day and nighttime climate when evaluating the effects of land cover change in a regional

climate model, finding that the nighttime warming of forests in Europe is underestimated. As observations demonstrate the asymmetric diurnal response to land cover change, continued investigations into the representation of land cover change in climate models should differentiate between day and nighttime climate.

Conclusions

In this study, we examine the patterns and drivers of the day and nighttime surface temperature response to deforestation (ΔT_S) using global satellite observations, reanalysis data, and in situ observations from flux towers. We find that a diurnal asymmetry exists in both the magnitude and sign of ΔT_S. In terms of magnitude, there is a larger ΔT_S signal over most regions during mid-day than compared to at night. The sign of ΔT_S changes from positive to negative in many places around the world, with most regions showing daytime warming and nighttime cooling.

There are distinct differences in the diurnal patterns of ΔT_S across different climate zones. In the tropical region, deforestation results in strong warming during the day, but has minimal influence on nighttime ΔT_S. In contrast, deforestation in high latitudes produces a large cooling signal at night, with relatively smaller cooling during the day. The temperate region is a transitional zone, showing moderate warming during the day and moderate cooling at night. The combination of satellite and reanalysis data allowed us to compare the relative importance of two competing biophysical processes: differences in absorbed solar radiation and the latent heat flux. We also provide empirical evidence of the importance of surface roughness on both daytime and nighttime ΔT_S.

We find that daytime ΔT_S is driven by differences in absorbed shortwave radiation (ΔK_a) and latent heat flux (ΔLE). While open lands have a higher albedo, and thus lower K_a, the magnitude of ΔLE generally dominates the spatial pattern of ΔT_S resulting in surface warming from deforestation. In high latitudes, the magnitude of ΔK_a overtakes that of ΔLE, resulting in a

surface cooling response to deforestation. There is a positive relationship between the heating potential ($\Delta H_P = \Delta K_a - \Delta LE$) and daytime ΔT_S. From this relationship, we estimate that approximately 2 K is not explained by ΔK_a and ΔLE, and is likely due to the difference in surface roughness between forests and open lands. The magnitude and spatial pattern of nighttime ΔT_S is related to the strength of the nocturnal temperature inversion, which is stronger in high latitudes and weaker in the tropics. Therefore, the roughness of forests is responsible for daytime cooling (dissipating heat away from the surface) and nighttime warming (bringing warm air aloft down to the surface). Additionally, nighttime ΔT_S is positively related to the relative amount of heat stored in forests and open lands during the day.

The role of forests, including the biophysical effects deforestation and reforestation, are increasingly being discussed in terms of climate change mitigation. Because of forests' important role in the global carbon cycle, international climate agreements account for land-based climate mitigation strategies including reforestation and afforestation. However, the biophysical effects of such strategies are not yet taken into account. This study and many others show that forest management strategies for the purpose of climate change mitigation need to consider the biophysical effects, as they have a strong influence on local climate. The growing body of evidence suggests that it is necessary to consider where to implement re/afforestation as a climate mitigation strategy. Avoided deforestation and afforestation in the tropics are the most effective from a climate perspective, as they have the strongest cooling effects.

Acknowledgements

We acknowledge high-performance computing support provided by NCAR's Computational and Information Systems Laboratory, sponsored by the National Science Foundation. Some data used in this analysis were obtained from the Atmospheric Radiation Measurement (ARM) Climate Research Facility, a U.S. Department of Energy Office of Science user facility sponsored by the Office of Biological and Environmental Research. This work used eddy covariance data acquired

and shared by the FLUXNET community, including these networks: AmeriFlux, AfriFlux, AsiaFlux, CarboAfrica, CarboEuropeIP, CarboItaly, CarboMont, ChinaFlux, Fluxnet-Canada, GreenGrass, ICOS, KoFlux, LBA, NECC, OzFlux-TERN, TCOS-Siberia, and USCCC. The ERA-Interim reanalysis data are provided by ECMWF and processed by LSCE. The FLUXNET eddy covariance data processing and harmonization was carried out by the European Fluxes Database Cluster, AmeriFlux Management Project, and Fluxdata project of FLUXNET, with the support of CDIAC and ICOS Ecosystem Thematic Center, and the OzFlux, ChinaFlux and AsiaFlux offices. We would also like to acknowledge financial support from Yale University and NCAR's ASP Graduate Visitor Program. We thank two reviewers whose valuable comments and insights contributed to the quality of this manuscript. The satellite and reanalysis datasets have been made available at http://doi.org/10.5281/zenodo.400699. Please direct any questions to natalie.schultz@yale.edu.

Supporting Information

In this supplement, additional information on our methods and supplementary figures and data to support the conclusions in the main text are provided. The method we used to standardize the flux tower nocturnal gradient measurements to 10m above displacement height is discussed first. The data used to make these corrections to the original gradient measurements are provided in Tables S2-S4. Table S2.1 shows the land cover classes from the IGBP land cover classification scheme that were used in this analysis to defined "open" and "forested" land. We include two figures (Figures S2.1-S2.2) that that illustrate the spatial patterns of the drivers of daytime ΔT_S, as well as ΔK_a and ΔLE, the two terms used to calculate ΔH_P. In addition, the relationships between ΔK_a and ΔLE and ΔT_S are presented here. Figure S2.3 shows the difference in the nocturnal surface inversion at two site pairs of flux towers, and Figure S2.4 presents the relationship between R_n and ΔT_S.

Standardizing Ta at 10m

The air temperature measurement height at the flux towers varied anywhere from 1.5 to 30.6 m above displacement height, *d*. For direct comparison with the MERRA nocturnal temperature inversion, we standardized the flux tower inversion calculation (Γ) to 10 m above the *d* using:

$$\Gamma = \Gamma_{orig} + \frac{\Delta T}{\Delta z}(z - 10) \qquad \text{(S1)}$$

where Γ_{orig} is the original inversion calculation ($T_S - T_a$), $\Delta T/\Delta z$ is the average nocturnal air temperature gradient (0.07 K/m for grasslands and 0.03 K/m for forests) (Table S2.2), and *z* is the measurement height above *d* (Tables S2.3-S2.4).

As most grassland sites reported the average canopy height as < 1m, we made the simplification that the measurement height was equal to the height above *d*. For forest tower sites, we calculated *d* as 2/3 of the canopy height (Table S2.3). For the grassland tower sites, standardizing to 10 m on average changed the Γ_{orig} values by -0.39 K, ranging from -0.52 to 0.09 K (Table S2.3). For the forest tower sites, this standardization resulted in an average correction of 0.34 K, ranging from 0.02 to 0.62 K (Table S2.4).

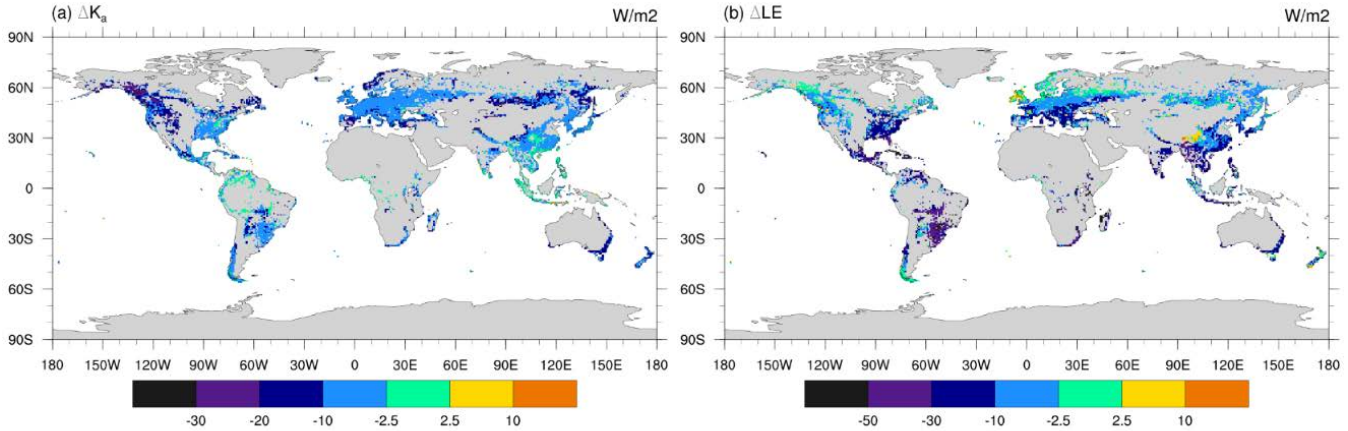

Figure S2.1. The 11-year annual mean (a) ΔK_a and (b) ΔLE

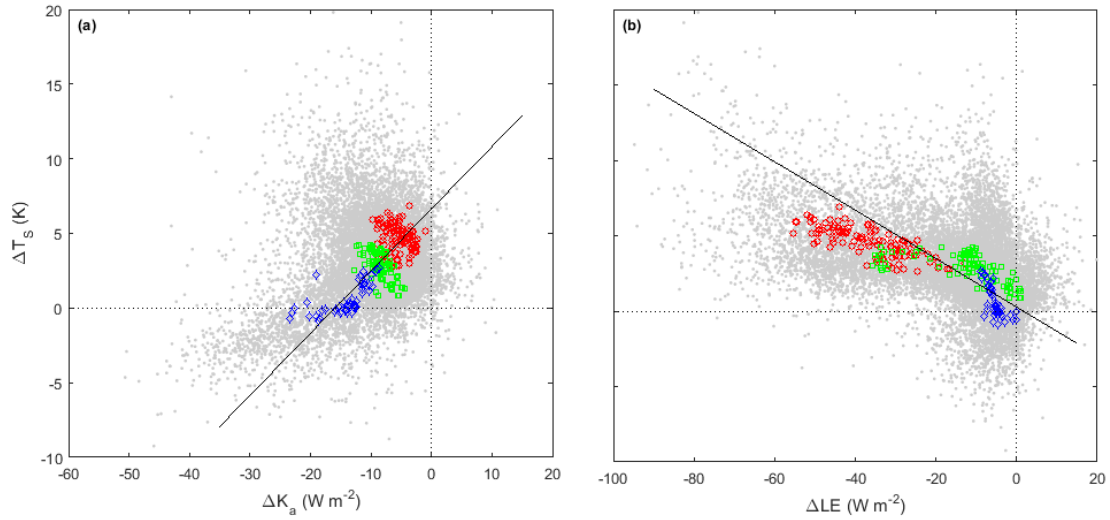

Figure S2.2. The dominant drivers of ΔT_S are (a) ΔK_a and (a) ΔLE. All sample grids are shown as the gray dots, while the zonal means of each climate zone are shown as the red circles (tropical), green squares (temperate), and blue diamonds (boreal). The black solid lines in (c) y = 0.417 (±0.006) x + 6.649 (±0.06) (R^2 = 0.17, p < 0.001) and (d) y = -0.160 (±0.002) x + 0.272 (±0.04) (R^2 = 0.22, p < 0.001) indicate the geometric mean regression for all sample grids (gray dots). Parameter bounds in the regressions are for the 95% confidence intervals.

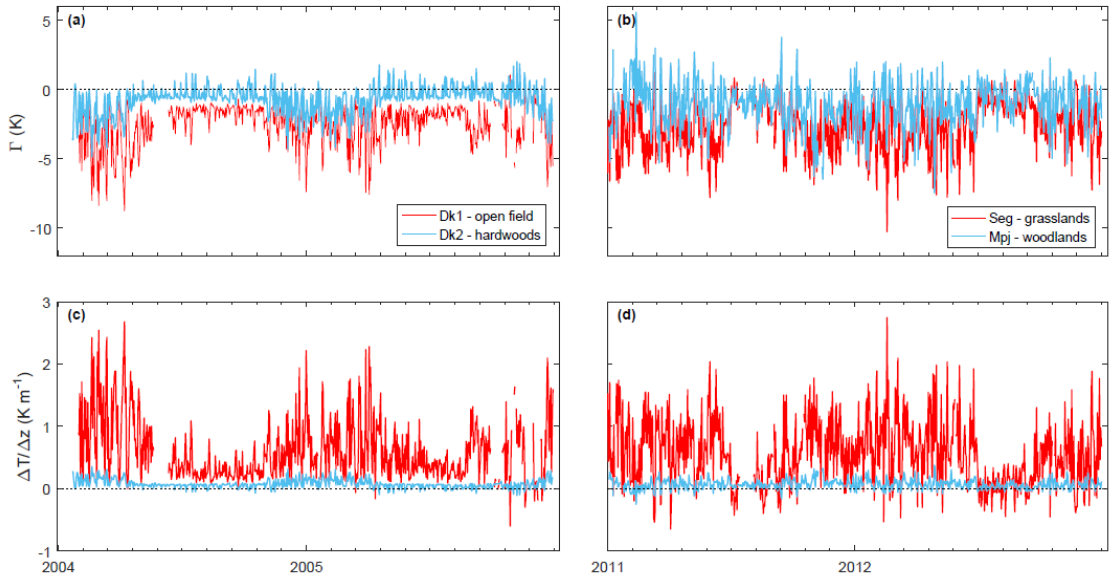

Figure S2.3. Two site pairs of flux towers used to compare the surface inversion between adjacent forested and open lands. Panels (a) and (c) show the surface inversion **Γ**, standardized to 10 m above the displacement height and the temperature gradient $\boldsymbol{\Delta T/\Delta z}$, calculated as ($T_S$ – T_a)/z, where z is measurement height for the site pair in North Carolina. Panels (b) and (d) show the same data for a site pair in New Mexico.

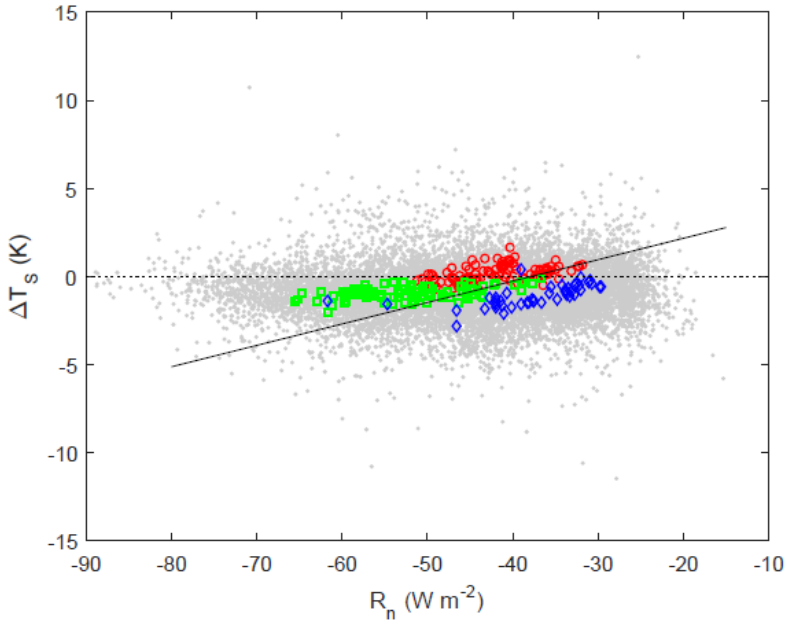

Figure S2.4. There is a positive relationship between R_n and ΔT_S (geometric mean regression: y = 0.122x (±0.002) + 4.602 (±0.08) ($p < 0.001$).

Site Name	Site ID	Land cover	h (m)	T_a low (m)	T_a high (m)	ΔT_a (K)	$\Delta T / \Delta z$ (K)	Dates	Reference
Grasslands									
ARM Lamont, OK	n/a	GRA	< 1	2	25	-2.36	0.103	2003-2013	*Turner et al.* [2016]
Santarem-Km77-Pasture	BR-Sa2	CRO	< 1	2.2	11.3	-0.325	0.036	2001-2005	*Sakai et al.* [2004]
Forests									
Western Boreal – Mature Aspen	CA-Oas	ENF	18	18	37	-3.86	0.020	1996-2006	*Blanken et al.* [1997]
Great Mountain Forest	US-GMF	MF	18.7	19.1	31.7	-0.165	0.013	1999-2000	*Lee and Hu* [2002]
Santarem-Km67-Primary Forest	BR-Sa1	EBF	40	49.75	61.94	-0.565	0.046	2002-2006	*Hutyra et al.* [2007]

Table S2.1. The average air temperature gradient, as measured from different heights at four sites (one grassland, three forested). These data were used to standardize the flux tower nocturnal inversion ($T_S - T_a$) measurements to 10 m above the displacement height. A gradient of 0.07 K/m was used for all grassland sites (average of grassland gradients), and a gradient of 0.03 K/m (average of the forest gradients) was used for forest sites.

Value	Label
0	Water
1	Evergreen needleleaf forest
2	Evergreen broadleaf forest
3	Deciduous needleleaf forest
4	Deciduous broadleaf forest
5	Mixed forest
6	Closed shrublands
7	Open shrublands
8	Woody savannas
9	Savannas
10	Grasslands
11	Permanent wetlands
12	Croplands
13	Urban and built-up
14	Cropland/natural vegetation mosaic
15	Snow and ice
16	Barren or sparsely vegetated
254	Unclassified
255	Fill Value

Table S2.2. The land cover classes from the MODIS (MCD12Q1) IGBP land cover classification scheme. We use IGBP classes 1-5 as representative of the "forest" land cover category (shaded green in the above table), and IGBP classes 9, 10, and 14 for the "open" land cover category (shaded orange in the table).

Site ID	measurement dates	original Γ (K)	gradient (K/m)	measurement height (m)	final Γ (K)
DE-RuR	2013 - 2014	-1.26	0.07	2.6	-1.78
US-FPe	2000 - 2008	-1.34	0.07	3.2	-1.82
US-KUT	2006 - 2007	-2.89	0.07	2	-3.45
US-Bkg	2008 - 2009	-0.91	0.07	3.5	-1.36
US-CaV	2009 - 2009	-1.7	0.07	3.5	-2.16
US-Var	2007 - 2014	-1.39	0.07	1.5	-1.98
US-Dk1	2004 - 2005	-1.8	0.07	3	-2.29
US-Seg	2012 - 2013	-1.97	0.07	3.5	-2.43
US-Goo	2004 - 2006	-2.36	0.07	3.5	-2.81
US-Wkg	2008 - 2015	-2.74	0.07	6.4	-2.99
US-Aud	2009 - 2010	-2.21	0.07	3.5	-2.66
BR-Sa2	2001 - 2005	-0.12	0.07	11.3	-0.11
FSM ranch	1999 - 2002	-0.02	0.07	8.3	-0.14
AU-Stp	2010 - 2011	-0.87	0.07	5	-1.22
AU-Emr	2012 - 2012	-1.36	0.07	5	-1.71

Table S2.3. The measurement details of each grassland flux tower site. The measurement height (z) was used to standardize the surface inversion to 10m above the displacement height. Because the canopy height of most sites was reported as < 1m, we approximated d as 0 m. The final Γ here are what are reported in the main text (Table 2.1).

Site ID	measurement dates	original Γ (K)	gradient (K/m)	canopy h (m)	*d* (m)	measurement height (m)	final Γ (K)
CA-Obs	2006 - 2010	-0.45	0.03	10	6.67	18.33	-0.20
CA-Oas	2005 - 2010	-1.14	0.03	21.5	14.33	24.67	-0.70
CA-Qfo	2006 - 2010	-1.51	0.03	13.8	9.20	14.8	-1.37
CA-Gro	2007 - 2011	-1.79	0.03	21.6	14.4	26.6	-1.30
US-Syv	2003 - 2005	-0.22	0.03	22	14.67	21.33	0.12
US-Wcr	2003 - 2005	-0.78	0.03	25	16.67	13.33	-0.68
US-UMB	2007 - 2014	-1.39	0.03	22	14.67	31.33	-0.75
US-Ho1	2008 - 2011	-1.14	0.03	20	13.33	15.67	-0.97
US-Blk	2007 - 2008	-1.34	0.03	21.4	14.27	20.82	-1.00
US-Slt	2005 - 2006	-0.91	0.03	20	13.33	10.67	-0.89
US-MMS	2007 - 2013	-0.36	0.03	26	17.33	28.37	0.19
US-MOz	2011 - 2013	-1.16	0.03	17	11.33	20.67	-0.84
US-Dk2	2004 - 2005	-1.10	0.03	25	16.67	23.13	-0.70
US-WBW	2003 - 2003	-0.76	0.03	17	11.33	18.67	-0.50
US-ChR	2008 - 2010	-1.53	0.03	25	16.67	23.33	-1.13
US-Mpj	2012 - 2013	-1.39	0.03	21.4	14.27	20.82	-1.07
RJ forest	1999 - 2002	-0.04	0.03	35	23.33	31.67	0.61

Table S2.4. The measurement details of each forest flux tower site. The measurement height (*z*) reported here is the measurement height above the displacement height. This height was used to standardize the original inversion values to 10 m above the displacement height. The final Γ here are what are reported in the main text (Table 2.1).

References

Alkama, R., and A. Cescatti (2016), Biophysical climate impacts of recent changes in global forest cover, *Science*, *351*(6273), 600-604.

Anderson-Teixeira, K. J., J. P. Delong, A. M. Fox, D. A. Brese, and M. E. Litvak (2011), Differential responses of production and respiration to temperature and moisture drive the carbon balance across a climatic gradient in New Mexico, *Global Change Biology*, *17*(1), 410-424, doi:10.1111/j.1365-2486.2010.02269.x.

Anderson, R. G., et al. (2011), Biophysical considerations in forestry for climate protection, *Frontiers in Ecology and the Environment*, *9*(3), 174-182, doi:10.1890/090179.

Arora, V. K., and A. Montenegro (2011), Small temperature benefits provided by realistic afforestation efforts, *Nature Geoscience*, *4*(8), 514-518, doi:10.1038/ngeo1182.

Bala, G., K. Caldeira, M. Wickett, T. J. Phillips, D. B. Lobell, C. Delire, and A. Mirin (2007), Combined climate and carbon-cycle effects of large-scale deforestation, *Proceedings of the National Academy of Sciences of the United States of America*, *104*(16), 6550-6555, doi:10.1073/pnas.0608998104.

Baldocchi, D., et al. (2001), FLUXNET: A New Tool to Study the Temporal and Spatial Variability of Ecosystem–Scale Carbon Dioxide, Water Vapor, and Energy Flux Densities, *Bulletin of the American Meteorological Society*, *82*(11), 2415-2434, doi:10.1175/1520-0477(2001)082<2415:fantts>2.3.co;2.

Bastable, H. G., W. J. Shuttleworth, R. L. G. Dallarosa, G. Fisch, and C. A. Nobre (1993), Observations of climate, albedo, and surface radiation over cleared and undisturbed amazonian forest, *international Journal of Climatology*, *13*, 783-796.

Bergeron, O., H. A. Margolis, T. A. Black, C. Coursolle, A. L. Dunn, A. G. Barr, and S. C. Wofsy (2007), Comparison of carbon dioxide fluxes over three boreal black spruce forests in Canada, *Global Change Biology*, *13*(1), 89-107, doi:10.1111/j.1365-2486.2006.01281.x.

Beringer, J. (2013), Sturt Plains OzFlux tower site, in *OzFlux: Australian and New Zealand Flux Research and Monitoring*, edited, hdl: 102.100.100/14230

Betts, R. A. (2000), Offset of the potential carbon sink from boreal forestation by decreases in surface albedo, *Nature*, *408*, 187-190.

Blanken, P. D., T. A. Black, P. C. Yang, H. H. Neumann, Z. Nesic, R. Staebler, G. den Hartog, M. D. Novak, and X. Lee (1997), Energy balance and canopy conductance of a boreal aspen forest: Partitioning overstory and understory components, *Journal of Geophysical Research: Atmospheres*, *102*(D24), 28915-28927, doi:10.1029/97jd00193.

Bonan, G. B. (2008), Forests and climate change: forcings, feedbacks, and the climate benefits of forests, *Science*, *320*(5882), 1444-1449, doi:10.1126/science.1155121.

Clark, K. L., N. Skowronski, and J. Hom (2010), Invasive insects impact forest carbon dynamics, *Global Change Biology*, *16*(1), 88-101, doi:10.1111/j.1365-2486.2009.01983.x.

Coursolle, C., et al. (2006), Late-summer carbon fluxes from Canadian forests and peatlands along an east–west continental transect, *Canadian Journal of Forest Research*, *36*(3), 783-800, doi:10.1139/x05-270.

Davis, D. J., P. S. Bakwin, C. Yi, B. W. Berger, C. Zhao, R. M. Teclaw, and J. G. Isebrands (2003), The annual cycles of CO2 and H2O exchange over a northern mixed forest as observed from a very tall tower, *Global Change Biology*, *9*, 1278-1293.

de Noblet-Ducoudré, N., et al. (2012), Determining Robust Impacts of Land-Use-Induced Land Cover Changes on Surface Climate over North America and Eurasia: Results from the First Set of LUCID Experiments, *Journal of Climate*, *25*(9), 3261-3281, doi:10.1175/jcli-d-11-00338.1.

Friedl, M. A., D. Sulla-Menashe, B. Tan, A. Schneider, N. Ramankutty, A. Sibley, and X. Huang (2010), MODIS Collection 5 global land cover: Algorithm refinements and characterization of new datasets, *Remote Sensing of Environment*, *114*(1), 168-182, doi:10.1016/j.rse.2009.08.016.

Gilmanov, T. G., L. L. Tieszen, B. K. Wylie, L. B. Flanagan, A. B. Frank, M. R. Haferkamp, T. P. Meyers, and J. A. Morgan (2005), Integration of CO2flux and remotely-sensed data for primary production and ecosystem respiration analyses in the Northern Great Plains: potential for quantitative spatial extrapolation, *Global Ecology and Biogeography*, *14*(3), 271-292, doi:10.1111/j.1466-822X.2005.00151.x.

Gu, L., T. Meyers, S. G. Pallardy, P. J. Hanson, B. Yang, M. Heuer, K. P. Hosman, J. S. Riggs, D. Sluss, and S. D. Wullschleger (2006), Direct and indirect effects of atmospheric conditions and soil moisture on surface energy partitioning revealed by a prolonged drought at a temperate forest site, *Journal of Geophysical Research*, *111*(D16), doi:10.1029/2006jd007161.

Hiller, R. V., J. P. McFadden, and N. Kljun (2010), Interpreting CO2 Fluxes Over a Suburban Lawn: The Influence of Traffic Emissions, *Boundary-Layer Meteorology*, *138*(2), 215-230, doi:10.1007/s10546-010-9558-0.

Hollinger, D. Y., et al. (2004), Spatial and temporal variability in forest-atmosphere CO2 exchange, *Global Change Biology*, *10*(10), 1689-1706, doi:10.1111/j.1365-2486.2004.00847.x.

Hutyra, L. R., J. W. Munger, S. R. Saleska, E. Gottlieb, B. C. Daube, A. L. Dunn, D. F. Amaral, P. B. de Camargo, and S. C. Wofsy (2007), Seasonal controls on the exchange of carbon and water in an Amazonian rain forest, *Journal of Geophysical Research: Biogeosciences*, *112*(G3), doi:10.1029/2006jg000365.

Jackson, R. B., et al. (2008), Protecting climate with forests, *Environmental Research Letters*, *3*(4), 044006, doi:10.1088/1748-9326/3/4/044006.

Jarvis, P. G., J. M. Massheder, S. E. Hale, J. B. Moncrieff, M. Rayment, and S. L. Scott (1997), Seasonal variation of carbon dioxide, water vapor, and energy exchanges of a boreal black spruce forest, *Journal of Geophysical Research: Atmospheres*, *102*(D24), 28953-28966, doi:10.1029/97jd01176.

Krishnan, P., T. P. Meyers, R. L. Scott, L. Kennedy, and M. Heuer (2012), Energy exchange and evapotranspiration over two temperate semi-arid grasslands in North America, *Agricultural and Forest Meteorology*, *153*, 31-44, doi:10.1016/j.agrformet.2011.09.017.

Lawrence, P. J., and T. N. Chase (2010), Investigating the climate impacts of global land cover change in the community climate system model, *International Journal of Climatology*, *30*(13), 2066-2087, doi:10.1002/joc.2061.

Lee, X., et al. (2011), Observed increase in local cooling effect of deforestation at higher latitudes, *Nature*, *479*(7373), 384-387, doi:10.1038/nature10588.

Lee, X., and X. Hu (2002), Forest-air fluxes of carbon water and energy over non-flat terrain, Boundary-Layer Meteorology, 103, 277-301.

Li, Y., N. De Noblet-Ducoudré, E. L. Davin, S. Motesharrei, N. Zeng, S. Li, and E. Kalnay (2016), The role of spatial scale and background climate in the latitudinal temperature response to deforestation, *Earth System Dynamics*, *7*(1), 167-181, doi:10.5194/esd-7-167-2016.

Li, Y., M. Zhao, S. Motesharrei, Q. Mu, E. Kalnay, and S. Li (2015), Local cooling and warming effects of forests based on satellite observations, *Nature communications*, *6*, 6603, doi:10.1038/ncomms7603.

Mahmood, R., et al. (2014), Land cover changes and their biogeophysical effects on climate, *International Journal of Climatology*, *34*, 929-953.

Malyshev, S., E. Shevliakova, R. J. Stouffer, and S. W. Pacala (2015), Contrasting Local versus Regional Effects of Land-Use-Change-Induced Heterogeneity on Historical Climate: Analysis with the GFDL Earth System Model, *Journal of Climate*, *28*(13), 5448-5469, doi:10.1175/jcli-d-14-00586.1.

Michiles, A. A. d. S., and R. Gielow (2008), Above-ground thermal energy storage rates, trunk heat fluxes and surface energy balance in a central Amazonian rainforest, *Agricultural and Forest Meteorology*, *148*(6-7), 917-930, doi:10.1016/j.agrformet.2008.01.001.

Mu, Q., M. Zhao, and S. W. Running (2011), Improvements to a MODIS global terrestrial evapotranspiration algorithm, *Remote Sensing of Environment*, *115*(8), 1781-1800, doi:10.1016/j.rse.2011.02.019.

Naudts, K., Y. Chen, M. J. McGrath, J. Ryder, A. Valade, J. Otto, and S. Luyssaert (2016), Europe's forest management did not mitigate climate warming, *Science*, *351*(6273), 597-600.

Novick, K. A., P. C. Stoy, G. G. Katul, D. S. Ellsworth, M. B. Siqueira, J. Juang, and R. Oren (2004), Carbon dioxide and water vapor exchange in a warm temperate grassland, *Oecologia*, *138*(2), 259-274, doi:10.1007/s00442-003-1388-z.

Oke, T. R. (1987), *Boundary Layer Climates*, University Press, Cambridge, UK.

Pataki, D. E., and R. Oren (2003), Species differences in stomatal control of water loss at the canopy scale in a mature bottomland deciduous forest, *Advances in Water Resources*, *26*(12), 1267-1278, doi:10.1016/j.advwatres.2003.08.001.

Peel, M. C., B. L. Finlayson, and T. A. McMahon (2007), Updated world map of the Koppen-Geiger climate classification, *Hydrology and Earth System Science*, *11*, 1633-1644.

Peng, S. S., S. Piao, Z. Zeng, P. Ciais, L. Zhou, L. Z. Li, R. B. Myneni, Y. Yin, and H. Zeng (2014), Afforestation in China cools local land surface temperature, *Proceedings of the National Academy of Sciences of the United States of America*, *111*(8), 2915-2919, doi:10.1073/pnas.1315126111.

Pielke, R. A., R. Avissar, M. Raupach, A. J. Dolman, X. Zeng, and A. S. Denning (1998), Interactions between the atmosphere and terrestrial ecosystems: influence on weather and climate, *Global Change Biology*, *4*, 461-475.

Pielke, R. A., et al. (2011), Land use/land cover changes and climate: modeling analysis and observational evidence, *Wiley Interdisciplinary Reviews: Climate Change*, *2*(6), 828-850, doi:10.1002/wcc.144.

Pitman, A. J., F. B. Avila, G. Abramowitz, Y. P. Wang, S. J. Phipps, and N. de Noblet-Ducoudré (2011), Importance of background climate in determining impact of land-cover change on regional climate, *Nature Climate Change*, *1*(9), 472-475, doi:10.1038/nclimate1294.

Pitman, A. J., et al. (2009), Uncertainties in climate responses to past land cover change: First results from the LUCID intercomparison study, *Geophysical Research Letters*, *36*(14), doi:10.1029/2009gl039076.

Post, H., H. J. Hendricks Franssen, A. Graf, M. Schmidt, and H. Vereecken (2015), Uncertainty analysis of eddy covariance CO2 flux measurements for different EC tower distances using an extended two-tower approach, *Biogeosciences*, *12*(4), 1205-1221, doi:10.5194/bg-12-1205-2015.

Rienecker, M. M., et al. (2011), MERRA: NASA's Modern-Era Retrospective Analysis for Research and Applications, *Journal of Climate*, *24*(14), 3624-3648, doi:10.1175/jcli-d-11-00015.1.

Sakai, R. K., D. R. Fitzjarrald, O. L. L. Moraes, R. M. Staebler, O. C. Acevedo, M. J. Czikowsky, R. d. Silva, E. Brait, and V. Miranda (2004), Land-use change effects on local energy, water, and carbon balances in an Amazonian agricultural field, *Global Change Biology*, *10*(5), 895-907, doi:10.1111/j.1529-8817.2003.00773.x.

Schaaf, C. B., et al. (2002), First operational BRDF, albedo nadir reflectance products from MODIS, *Remote Sensing of Environment*, *83*, 135-148.

Schmid, H. P. (2003), Ecosystem-atmosphere exchange of carbon dioxide over a mixed hardwood forest in northern lower Michigan, *Journal of Geophysical Research*, *108*(D14), doi:10.1029/2002jd003011.

Schmid, H. P., C. S. B. Grimmond, F. Cropley, B. Offerele, and H.-B. Su (2000), Measurements of CO2 and energy fluxes over a mixed hardwood forest in the mid-western United States, *Agricultural and Forest Meteorology*, *103*, 357-374.

Schroder, I. (2014), Arcturus Emerald OzFlux tower site, in *OzFlux: Australian and New Zealand Flux Research and Monitoring*, edited, hdl: 102.100.100/14249

Schultz, N. M., X. Lee, P. J. Lawrence, D. M. Lawrence, and L. Zhao (2016), Assessing the use of subgrid land model output to study impacts of land cover change, *Journal of Geophysical Research: Atmospheres*, *121*(11), 6133-6147, doi:10.1002/2016jd025094.

Snyder, P. K., C. Delire, and J. A. Foley (2004), Evaluating the influence of different vegetation biomes on the global climate, *Climate Dynamics*, *23*(3-4), doi:10.1007/s00382-004-0430-0.

Tang, J., P. V. Bolstad, A. R. Desai, J. G. Martin, B. D. Cook, K. J. Davis, and E. V. Carey (2008), Ecosystem respiration and its components in an old-growth forest in the Great Lakes region of the United States, *Agricultural and Forest Meteorology*, *148*(2), 171-185, doi:10.1016/j.agrformet.2007.08.008.

Thompson, S. E., C. J. Harman, A. G. Konings, M. Sivapalan, A. Neal, and P. A. Troch (2011), Comparative hydrology across AmeriFlux sites: The variable roles of climate, vegetation, and groundwater, *Water Resources Research*, *47*(10), n/a-n/a, doi:10.1029/2010wr009797.

Turner DD, R. E., GM Stokes, TP Ackerman, JH Mather, TS Cress, DL Sisterson, CN Long, J Verlinde, MA Miller, B Schmid, R McCord, RA Peppler, EJ Mlawer, JJ Michalsky, P Kollias, MD Shupe, SA McFarlane, A McComiskey, G Feingold, LK Berg, M Zhang, SK Krueger, DA Randall, S Ghan, M Ahlgrimm, M Haefflin, R Marchand, and E al. (2016), The Atmospheric Radiation Measurement (ARM): the First 20 Years, Online: American Meteorological Society, ISSN: 0065-9401.

Vanden Broucke, S., S. Luyssaert, E. L. Davin, I. Janssens, and N. van Lipzig (2015), New insights in the capability of climate models to simulate the impact of LUC based on temperature decomposition of paired site observations, *Journal of Geophysical Research: Atmospheres*, *120*(11), 5417-5436, doi:10.1002/2015jd023095.

von Randow, C., et al. (2004), Comparative measurements and seasonal variations in energy and carbon exchange over forest and pasture in South West Amazonia, *Theoretical and Applied Climatology*, *78*(1-3), doi:10.1007/s00704-004-0041-z.

Wan, Z. (2008), New refinements and validation of the MODIS Land-Surface Temperature/Emissivity products, *Remote Sensing of Environment*, *112*(1), 59-74, doi:10.1016/j.rse.2006.06.026.

Wickham, J. D., T. G. Wade, K. H. Riitters, and J. Peñuelas (2013), Empirical analysis of the influence of forest extent on annual and seasonal surface temperatures for the continental United States, *Global Ecology and Biogeography*, *22*(5), 620-629, doi:10.1111/geb.12013.

Wilson, T. B., and T. P. Meyers (2007), Determining vegetation indices from solar and photosynthetically active radiation fluxes, *Agricultural and Forest Meteorology*, *144*(3-4), 160-179, doi:10.1016/j.agrformet.2007.04.001.

Winckler, J., C. H. Reick, and J. Pongratz (2017), Robust Identification of Local Biogeophysical Effects of Land-Cover Change in a Global Climate Model, Journal of Climate, 30(3), 1159-1176, doi:10.1175/jcli-d-16-0067.1.

Wouters, H., K. De Ridder, M. Demuzere, D. Lauwaet, and N. P. M. van Lipzig (2013), The diurnal evolution of the urban heat island of Paris: a model-based case study during Summer 2006, *Atmospheric Chemistry and Physics*, *13*(17), 8525-8541, doi:10.5194/acp-13-8525-2013.

Xu, L., and D. D. Baldocchi (2004), Seasonal variation in carbon dioxide exchange over a Mediterranean annual grassland in California, *Agricultural and Forest Meteorology*, *123*(1-2), 79-96, doi:10.1016/j.agrformet.2003.10.004.

Zhang, M., et al. (2014), Response of surface air temperature to small-scale land clearing across latitudes, *Environmental Research Letters*, *9*(3), 034002, doi:10.1088/1748-9326/9/3/034002.

Zhao, K., and R. B. Jackson (2014), Biophysical forcings of land-use changes from potential forestry activities in North America, *Ecological Monographs*, *84*(2), 329-353.

Zhou, L., Y. Tian, S. Baidya Roy, C. Thorncroft, L. F. Bosart, and Y. Hu (2012), Impacts of wind farms on land surface temperature, *Nature Climate Change*, doi:10.1038/nclimate1505.

Chapter 3: Assessing the use of sub-grid land model output to study impacts of land cover change

Published as: Schultz, N. M., X. Lee, P. J. Lawrence, D. M. Lawrence, and L. Zhao (2016), Assessing the use of subgrid land model output to study impacts of land cover change, *J. Geophys. Res. Atmos.*, 121, 6133–6147, doi:10.1002/2016JD025094.

Abstract

Sub-grid information from land models has the potential to be a powerful tool for investigating land-atmosphere interactions, but relatively few studies have attempted to exploit sub-grid output. In this study, we modify the configuration of the Community Land Model version CLM4.5 so that each plant functional type (PFT) is assigned its own soil column. We compare sub-grid and grid cell-averaged air temperature and surface energy fluxes from this modified case (PFTCOL) to a case with the default configuration—a shared soil column for all PFTs (CTRL), and examine the difference in simulated surface air temperature between grass and tree PFTs within the same grid cells (ΔT_{GT}). The magnitude and spatial patterns of ΔT_{GT} from PFTCOL agree more closely with observations, ranging from -1.5 K in boreal regions to +0.6 K in the tropics. We find that the column configuration has a large effect on PFT-level energy fluxes. In the CTRL configuration, the PFT-level annual mean ground heat flux (G) differs substantially from zero. For example, at a typical tropical grid cell, the annual G is 31.8 W m^{-2} for the tree PFTs and -14.7 W m^{-2} for grass PFTs. In PFTCOL, G is always close to zero. These results suggest that care must be taken when assessing local land cover change impacts with sub-grid information. For models with PFTs on separate columns, it may be possible to isolate the differences in land surface fluxes between vegetation types that would be associated with land cover change from other climate forcings and feedbacks in climate model simulations.

Introduction

Land cover change influences global and local climate by altering terrestrial carbon storage and atmospheric CO_2 concentrations (biogeochemical effect) and by modifying surface radiation and turbulent fluxes (biophysical effect) [e.g. *Bala et al.*, 2007; *Bonan*, 2008; *Ciais et al.*, 2013; *Mahmood et al.*, 2014]. The biophysical effects of land cover change, which include changes to surface fluxes of radiation, heat, moisture, and momentum [*Pielke et al.*, 1998], are especially important for regional and local surface climate [*de Noblet-Ducoudré et al.*, 2012; *P J Lawrence and Chase*, 2010]. The biophysical effects of land cover change can be summarized by changes in (1) surface albedo, (2) evapotranspiration, and (3) roughness length and turbulent exchange, with their contribution on local climate quantified by changes in surface air temperature [*Bonan*, 2008; *Mahmood et al.*, 2014]. The relative importance of these three competing effects varies geographically, and may amplify or dampen changes in surface climate caused by rising atmospheric greenhouse gas concentrations.

Understanding and quantifying the biophysical effects of land cover change on local climate are important for distinguishing between different anthropogenic forcings, but this understanding is hindered by a number of methodological challenges. Observational and modeling studies tend to agree on the latitudinal pattern of the temperature response to deforestation, with cooling in high latitudes and warming in low latitudes [e.g. *Davin and de Noblet-Ducoudré*, 2010; *P J Lawrence and Chase*, 2010; *Lee et al.*, 2011; *Zhang et al.*, 2014]. However, while observational methods have helped answer some major questions, they are limited by relatively short and sporadic measurement periods. Data that can be used to robustly and directly quantify the relative impact of the various biophysical processes on temperature differences for different land cover types is sparse, and frequently suffers from some limitations such as differing underlying atmospheric conditions [*Lee et al.*, 2011; *Pielke et al.*, 2011].

Utilizing global climate models (GCMs) to assess the impact of biophysical land cover changes poses its own set of challenges [*de Noblet-Ducoudré et al.*, 2012; *Pielke et al.*, 2011; *Pitman et al.*, 2009]. Most modeling studies use two sets of simulations to evaluate the biophysical effects of historic land cover change: one with pre-industrial or potential vegetation land cover and the other with present-day land cover, isolating the biophysical effects of land cover by prescribing the same atmospheric concentrations of CO_2 and other greenhouse gases with both sets of land cover conditions [e.g. *P J Lawrence and Chase*, 2010]. Other modeling studies have taken it a step farther and applied the so-called "scorched Earth" strategy [*Pielke et al.*, 2011] in which the biophysical effects from a completely deforested world are compared to a fully forested world [e.g. *Davin and de Noblet-Ducoudré*, 2010]. Identifying and evaluating the biophysical effects of land cover change as the difference between two modeling scenarios is complicated by the need to properly establish that modeled land cover change climate signals cannot be simply explained as unforced model variability or non-local effects of land cover change such as changes to atmospheric or ocean circulation [*Pielke et al.*, 2011; *Pitman et al.*, 2009]. In addition, differences in the parameterization of vegetation types and the implementation of land cover change among land models leads to inconsistencies in biophysical effects of historical land cover change between different GCMs [*de Noblet-Ducoudré et al.*, 2012; *Pitman et al.*, 2009].

While some modeling studies have implemented land cover change as a fractional change in the distribution of vegetation within a grid cell, analyses have still focused on the grid cell-averaged difference of surface variables such as air temperature and energy fluxes [*P J Lawrence and Chase*, 2010; *Pitman et al.*, 2009]. Many terrestrial models represent land cover heterogeneity within a grid cell as a mosaic of sub-grid tiles with distinct physical, biogeochemical, and ecological properties. However, few studies have attempted to utilize the sub-grid information to assess the biophysical effects of land cover change. A notable exception is the recent study by *Malyshev et al.* [2015]. Their treatment of land cover tiles in the land component, LM3.0, of the

Geophysical Fluid Dynamics Laboratory (GFDL) Earth System Model, ESM2Mb, captures the above and below-ground heterogeneity of land cover types within a grid cell, allowing for the comparison of the response of different land cover types to the same atmospheric forcing.

Representing sub-grid land surface heterogeneity in global climate models has long been a challenging problem. In early versions of GCMs, land-surface parameters were often set to those of the dominant vegetation type within a grid cell [*Arain et al.*, 1999]. However, recognizing that significant spatial variability in vegetation and other features exist within the spatial area of a single model grid cell, new strategies for representing sub-grid land surface heterogeneity were developed. At the two extremes are the "mixture" and "mosaic" approaches. At one end of the spectrum is the "mixture" strategy, which assumes that the different vegetation types are homogenously mixed within a grid cell, and the average of the structural, ecological, and physiological attributes of the vegetation types within the grid cell are used for surface calculations. The atmospheric model then interacts with the surface fluxes computed from this vegetation composite [*Koster and Suarez*, 1992]. At the other end of the spectrum is the "mosaic" strategy, which represents different land cover types as geographically distinct regions, each interacting with the atmospheric model separately, with no interaction between the tiles. In a full mosaic approach, in addition to surface energy and water fluxes computed for each individual tile, soil temperature, moisture, and snow cover evolve independently for each vegetation tile [*Koster and Suarez*, 1992; *Li and Arora*, 2012; *Molod*, 2002].

Many current versions of GCMs use land surface heterogeneity strategies that lie between the "mixture" and the "full mosaic" approaches described above. The land surface representation within the Community Land Model (CLM), the land component of the Community Earth System Model (CESM) consists of up to 15 plant functional types (PFTs) within the vegetated "land unit" of the grid cell [*Oleson et al.*, 2013]. Biogeochemical and biophysical fluxes are computed at the PFT-level, and then aggregated (area-weighted) to the column level, in CLM nomenclature.

While the PFTs within CLM can be thought of as a tile or mosaic surface configuration, all PFTs within the naturally vegetated land unit of the grid cell share a single soil column, with shared soil (temperature, moisture) and snow properties (see *Methods* for more details). A single atmospheric forcing is applied to all PFT tiles within a grid cell. This type of land surface representation is consistent, at least broadly, with many other models in the phase 5 of the Coupled Model Intercomparison Project (CMIP5) [*Malyshev et al.*, 2015].

Sub-grid information from climate models can be a powerful tool for investigating land-atmosphere interactions, yet PFT-level output from land models has been under-utilized in land cover change studies in favor of grid cell-averaged output. In contrast, sub-grid information from non-vegetated land surface tiles has been used in CLM modeling experiments. For example, urban tiles within a grid cell have been used to investigate the contribution of local background climate to urban heat islands [*Zhao et al.*, 2014], and the sub-grid lake model has been used to study lake-atmosphere interactions and the modulating effects of lakes on regional climate [*Deng et al.*, 2013; *Subin et al.*, 2012]. Perhaps part of the reason that individual PFT tiles have not been frequently used in GCM experiments is because of the common characteristic of a shared soil column, which does not allow for the complete separation of each PFT from the others.

It is debatable whether the mixture or full mosaic strategy is a more "realistic" representation of the natural landscape in a model grid cell. The mixture approach is perhaps more appropriate for savanna-like landscapes where trees and grasses are interspersed and competing for water and nutrients. The mosaic approach may be more appropriate for regions with distinct areas of different land cover types. A potential advantage of the full mosaic approach is that it may be able to more clearly isolate the role and response of different vegetation types. Using CESM as an example, since the same atmospheric forcing is applied to PFT-tiles, the differing responses of each vegetation type to the same atmospheric forcing can be examined. By directly comparing the response of one land cover type to another within the same grid cell, the complicating factors

that arise from multiple simulations, unforced variability or non-local effects of land cover change, are no longer relevant. Additionally, analysis of sub-grid information may be useful in future climate projection simulations to help understand how local biophysical effects of land cover change compare to other large-scale forcings, like a doubling of CO_2 for example.

In this study, we modify the sub-grid PFT configuration of CLM4.5 so that it may be used to isolate the effects of land cover and land cover change on local climate. We compare the default (multiple vegetation types on a shared soil column) version to a modified version in which each PFT is given an individual soil column. Our specific objectives are to: (1) examine the effect of a shared soil column versus individual soil column configuration on sub-grid (PFT-level) and grid cell-averaged output of surface air temperature and energy fluxes, and (2) perform preliminary evaluation of the individual PFT-column configuration to determine whether it may provide an advantage over the shared-column configuration in land cover change experiments.

Methods

Model description

The Community Land Model (CLM) [*D M Lawrence et al.*, 2011; *Oleson et al.*, 2013] is the land component of the Community Earth System Model (CESM) [*Hurrell et al.*, 2013]. In CLM4.5, the latest version of CLM, the land surface is represented as a nested hierarchy of sub-grid levels. At the broadest level, the land unit, each grid cell may be divided into fractions of natural vegetation, lakes, urban areas, glaciers, and crops. The second sub-grid level for the vegetated land unit is the column, which captures variations in soil and snow variables within the land unit. The soil profile in the vegetated land unit in CLM4.5 is represented as 15 discrete layers (to a depth of 35 m, with more soil layers near the surface). Hydrology calculations are done for just the top ten layers (from the surface to the depth of 2.9 m), while soil temperature is calculated for all 15 layers. Up to five additional layers may be added for snow, depending on snow depth. The

vegetated land unit is assigned a single column, with fractional areas of all the relevant plant functional types (PFTs) for that grid cell sharing the column.

The PFT-level, or third sub-grid level, specifies the differences in the biophysical and biogeochemical processes across different vegetation types. In addition to bare ground, the vegetated land unit may be comprised of up to 15 different PFTs. PFTs differ in their optical properties, as well as their water uptake, aerodynamic, and photosynthetic parameters. The PFT parameterizations control the surface energy and biogeochemical fluxes from the vegetated surface. Fluxes from the land surface are computed at the PFT-level, and then area-weighted to the column, land unit, and then grid cell level before being passed to the atmosphere model. The same atmospheric forcing is used to force all PFTs within the grid cell.

Experimental setup

Two CLM4.5 simulations were run to investigate the effects of a shared soil column versus individual PFT columns on both the PFT-level and grid-cell level output of surface state variables and fluxes. The first simulation (CTRL) was run using the default configuration of CLM4.5, where all PFTs within a grid cell shared a single soil column. The second simulation (PFTCOL) was run using a modified version of CLM4.5, where each PFT within the vegetated land unit was assigned to its own soil column (Figure 3.1). Both the CTRL and PFTCOL simulations were run with present-day land cover conditions, with vegetation phenology [leaf area index (LAI), stem area index (SAI)] prescribed by satellite observations [*P J Lawrence and Chase*, 2007; *Myneni et al.*, 2002]. In both simulations, CLM4.5 was run offline forced with 1991-2010 CRUNCEP atmospheric forcing data [*Viovy*, 2011]. Each case was run for 81 years, with the first 60 years devoted to spinup of soil temperature and moisture. PFT-level output and grid cell averages were archived for all surface and below ground state and flux variables at monthly intervals for the first 80 years, and then at hourly intervals for the final year.

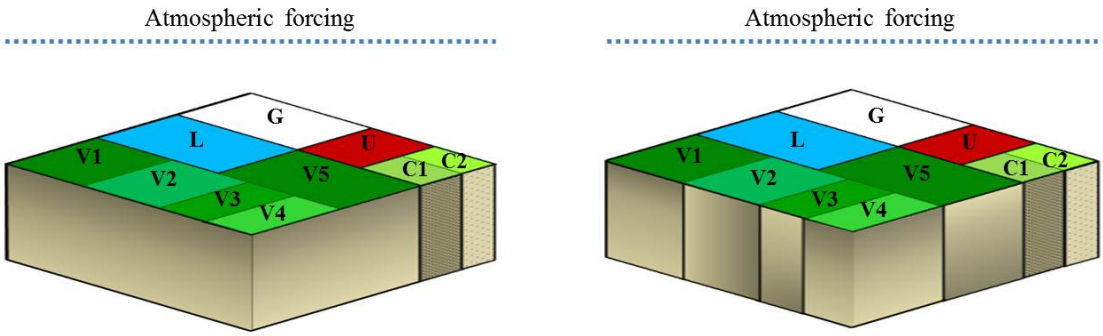

Figure 3.1. Schematic diagram illustrating the above and below-ground configuration of CLM4.5 in the (a) CTRL and (b) PFTCOL simulations. A hypothetical grid cell may contain multiple land units (G – glacier, L – lake, U – urban, V – vegetated, C – crop). By default, natural PFTs share a single soil column (CTRL). In the modified configuration (PFTCOL), each natural PFT is assigned its own soil column. For both the CTRL and PFTCOL cases, atmospheric inputs (incoming solar and longwave radiation, temperature, specific humidity, wind, pressure, and precipitation) are the same for all tiles within the grid cell.

Comparative analysis

We conducted a comparative analysis of air temperature and surface energy fluxes at both the PFT-level and grid cell-level between the PFTCOL and CTRL simulations. The purpose of this comparison was to quantify the effect of the column configuration on sub-grid and grid cell-averaged surface climate variables. For the PFT-level comparisons, we area-weighted the grass and tree PFTs within each grid cell into a single value for each of these respective land cover categories. Although some grid cells contained other PFTs, including bare soil and shrubs, our analysis focuses on tree and grass PFTs for two reasons. First, we were interested in comparing how PFTs from distinct land cover classes responded to the change in column configuration. Second, these two broad classes had the widest spatial distribution across the globe (i.e. there were more grid cells that contained both tree and grass PFTs). It should be noted that the grid cell averaged values do contain all PFTs within each grid cell, because in addition to examining PFT-level differences, we wanted to investigate whether this new configuration could affect atmospheric processes when coupled to the atmosphere model. We present the comparison as the difference (Δ) in surface climate variables between the PFTCOL and CTRL simulations (PFTCOL – CTRL). For example, ΔT_a is the difference in air temperature between the PFTCOL and CTRL cases. We also examined the difference in each term in the surface energy balance equation (Eq 1).

$$R_{net} = K\downarrow - K\uparrow + L\downarrow - L\uparrow = H + \lambda E + G \quad (1)$$

Incoming shortwave ($K\downarrow$) and longwave ($L\downarrow$) were prescribed by the atmospheric forcing data, and therefore did not vary between the PFTCOL and CTRL cases. We compared the differences in reflected shortwave ($K\uparrow$) and emitted longwave ($L\uparrow$) radiation, net radiation (R_{net}), as well as the sensible heat (H), latent heat (λE), and ground heat (G) fluxes. Our sign convention is that a flux away from the surface is positive and a flux towards the surface is negative. We first compared the PFT-level (tree and grass PFTs) and grid cell-averaged values of these surface

variables at the global scale. For a closer investigation into the temporal differences between the PFTCOL and CTRL simulations, three grid cells were selected; one grid cell from each of three distinct climate regions: tropical (grid center at 6.13ºN, 288.75ºE), temperate (35.34ºN, 282.5ºE), and boreal (66.44ºN, 222.5ºE). In each of these grid cells, the sum of tree and grass PFT area took up the majority of the grid cell; however, smaller percentages of other PFTs (bare soil or shrubs) did exist in each of these grid cells (Table S3.1). These other PFTs are ignored from the PFT-level comparisons, but are taken into account in the grid cell-averaged values. For each of these three grid cells, monthly and hourly output from the two cases was compared.

Finally, we conducted a comparison of surface air temperature between different land cover types (grass and tree PFTs) within the same grid cell in each simulation. For both the CTRL and PFTCOL cases, the 20-year mean difference in air temperature between grass and tree PFTs (grass air temperature minus tree air temperature, both at the screen height) was calculated. This air temperature difference (ΔT_{GT}) can be thought of as a proxy for a local-scale deforestation signal (i.e. the effect of local-scale deforestation on surface air temperature). While this is not a true deforestation signal, because our offline simulations do not allow the atmosphere to respond to land cover change and do not account for the variations in land cover after deforestation occurs, this method, which substitutes space for time, allows for the comparison of the land surface response of different vegetation types to the same atmospheric conditions. We chose air temperature for this initial comparison of sub-grid surface climate because the magnitude and spatial pattern of ΔT_{GT} has been relatively well established in previous observational and modeling studies [e.g. *Davin and de Noblet-Ducoudré*, 2010; *Lee et al.*, 2011; *Zhang et al.*, 2014]. This comparison of air temperature between different land cover types within the same grid cell allows a preliminary assessment of whether the modified sub-grid configuration in the PFTCOL simulation improves the land cover change signal.

In this paper, we first present the global (zonal average) differences in surface variables between the PFTCOL and CTRL simulations. The zonal average is calculated as the arithmetic mean of the difference between tree or grass PFTs across each latitude, including only grid cells that include a fraction of the PFT being averaged. We then discuss the monthly and hourly differences in surface climate variables from the three selected grid cells. The differences are shown in figures in the main text, while the monthly and hourly variations of the actual air temperature and surface energy fluxes are presented in the Supplemental Information (Figures S3.1-S3.6). Lastly, we show ΔT_{GT} for both the CTRL and PFTCOL simulations.

Results

Zonal patterns

Figure 3.2 presents the zonally-averaged difference in 2-m air temperature (ΔT_a) at the PFT-level (grass and tree PFTs) and grid cell-level between the PFTCOL and CTRL simulations (PFTCOL – CTRL). At the grid cell-level, zonal mean ΔT_a is relatively small, ranging from -0.10 K to 0.10 K. At the sub-grid or PFT-level, however, ΔT_a is an order of magnitude larger and exhibits distinct latitudinal patterns. Generally, the individual PFT columns produce lower air temperatures over grass PFTs and higher temperatures over tree PFTs in high latitudes, while the reverse is observed in middle to low latitudes (between 40°N and 40°S). The largest differences in T_a between the PFTCOL and CTRL cases for both grass and tree PFTs are observed above 40°N. Above 40°N, the ΔT_a of tree PFTs reaches 2.25 K, while the ΔT_a of grass PFTs reaches -0.79 K. However, it should be noted that the large differences at highest latitudes (> 75°N) result from averaging across a low number of grid cells. Global maps of ΔT_a are presented in Figure S3.1. This warming and cooling pattern for tree and grass PFTs in high latitudes is dominated by changes in air temperature during winter months, resulting from snow cover and albedo changes, as will be discussed in more detail in later sections.

The configuration of columns, either shared as in the CTRL case or individual as in the PFTCOL case, has a considerable effect on how surface energy is partitioned between radiative, turbulent, and ground heat fluxes at the PFT level, while only minimally affecting the grid cell-averaged values of surface energy fluxes. Figure 3.3 presents the zonally-averaged PFTCOL – CTRL grid cell-level and PFT-level differences in surface energy fluxes: net radiation (ΔR_{net}), sensible heat flux (ΔH), ground heat flux (ΔG), and latent heat flux ($\Delta \lambda E$). Global maps of these data are given in Figure S3.2. Because CLM4.5 in both the PFTCOL and CTRL cases is forced by the same atmospheric data, changes in net radiation between the two cases are due only to changes in emitted longwave and reflected shortwave radiation from the land surface. The overall zonal patterns in ΔR_{net} for tree and grass PFTs are dominated primarily by changes in emitted longwave radiation. At high latitudes, changes in albedo, and therefore reflected solar radiation, are an important contributor to ΔR_{net}, particularly for grass PFTs. The magnitude of ΔR_{net} is similar for both grass and tree PFTs. Across all latitudes, ΔR_{net} for tree PFTs ranges from is -8.6 Wm^{-2} to 4.3 Wm^{-2}, while ΔR_{net} for grass PFTs ranges from -8.6 Wm^{-2} to 7.3 Wm^{-2} for grasses. At the grid cell-level, ΔR_{net} is relatively small, ranging from -1.3 Wm^{-2} to 0.3 Wm^{-2}.

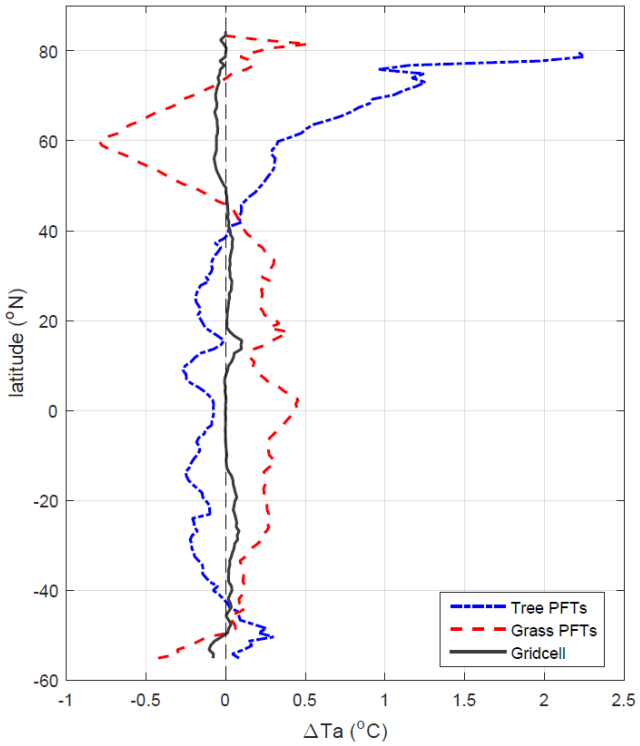

Figure 3.2. The zonal mean of the difference in 2-m air temperature between the two cases (PFTCOL – CTRL), shown at the grid cell level and PFT-level (PFTs area-weighted into "trees" and "grasses". Shown as the average of 1991-2010.

Changes in the turbulent fluxes are evident at the PFT-level, but are relatively small at the grid-cell level. Below 60°N, ΔH for tree PFTs is negative, with the largest decrease (-36 Wm^{-2}) occurring in mid-latitudes. North of 60°N, ΔH is positive for tree PFTs, reaching of 37 Wm^{-2}. The ΔH of grass PFTs is positive (up to 22 W m^{-2}) over most latitudes, becoming slightly negative at high latitudes. Compared to ΔH at the PFT-level, ΔH at the grid cell-level is quite small (less than 1 W m^{-2} in magnitude) over all latitudes. The PFT-level $\Delta\lambda E$ follows a similar pattern to ΔH, with the exception of the tropics, where there was a large increase in λE in the PFTCOL relative to the CTRL case. It was unexpected that ΔH and $\Delta\lambda E$ from each of the two PFT categories did not offset each other. Where ΔH was positive, we expected $\Delta\lambda E$ to be negative, and vice versa, particularly because the magnitude of ΔR_{net} for each of the PFT classes was less than ±10 Wm^{-2}. However, after accounting for ΔG, the surface energy budget for tree and grass PFTs was balanced.

Examining PFT-level ΔG reveals the influence of the shared versus individualized soil columns on the surface energy budget of PFTs, and why PFT-level data may be biased in the shared column configuration. The ground heat flux exhibited the largest difference of all surface energy fluxes between the PFTCOL and CTRL cases. Notably, the large ΔG at the PFT-level is due to the fact that the annual PFT-level G in the CTRL case is strongly negative or positive, by up to 50Wm^{-2} in magnitude at some latitudes, while the annual PFT-level G is the PFTCOL case is approximately zero. For tree PFTs, ΔG ranges from -71.8 Wm^{-2} to 41.7 W m^{-2}, while for grass PFTs, ΔG ranges from -47.8 Wm^{-2} to 3.0 W m^{-2}. The grid cell-averaged ΔG is very small (± 0.1 W m^{-2}) between the two cases.

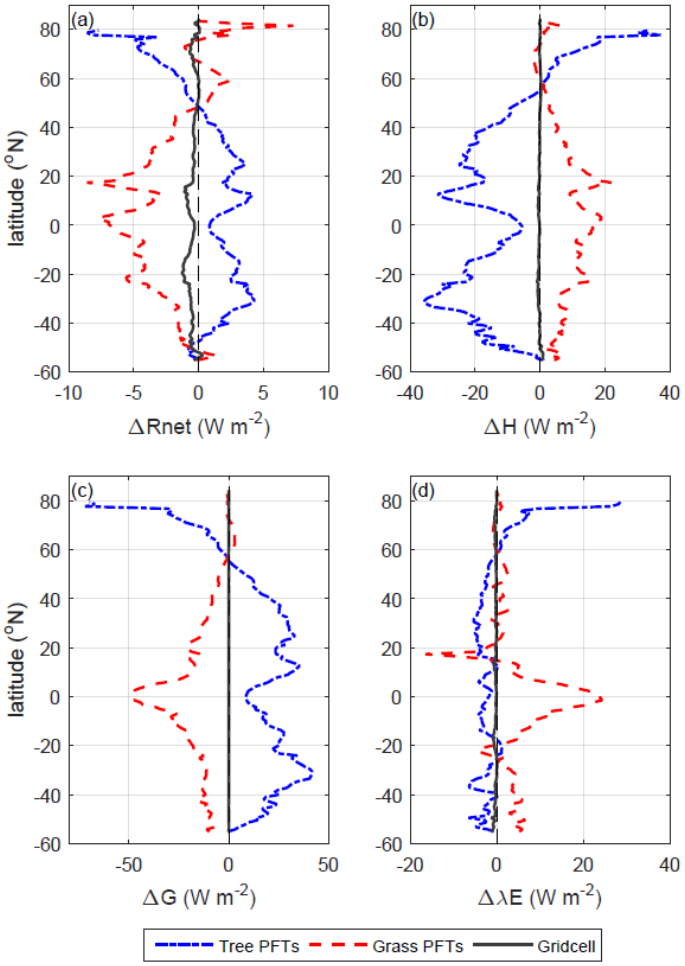

Figure 3.3. The zonal mean of the differences in (a) net radiation, (b) sensible heat flux, (c) ground heat flux, and (d) latent heat flux between the PFTCOL and CTRL cases (1991-2010).

Temporal

Here, we compare the PFT-level monthly 2-m air temperature and energy fluxes between the PFTCOL and CTRL cases for each of the three grid cells in the tropical, temperate, and boreal regions. For diurnal differences, we focus on the diurnal patterns of ΔT_a and ΔG for each of the three grid cells. A summary of the annual differences in T_a and surface energy fluxes for each of these three grid cells is presented in Table 1. The seasonality of the monthly atmospheric forcing data for each of these three grid cells is shown in Figure S3.3.

Seasonal

Figure 3.4 presents the monthly differences in 2-m air temperature and surface energy fluxes for tree and grass PFTs between the PFTCOL and CTRL simulations for the tropical grid cell. For 2-m air temperature and the radiative fluxes, the differences between the two cases exhibit little seasonality. The ΔT_a is negative for tree PFTs and positive for grass PFTs over all months, with seasonal variations in the range of only 0.15 to 0.25 K. Across all seasons, PFT-level ΔR_{net} is driven by changes to emitted longwave radiation ($\Delta L\uparrow$). The $\Delta L\uparrow$ for tree and grass PFTs follows ΔT_a: a cooling of tree PFTs in the PFTCOL case results in reduced $L\uparrow$ and thus a higher R_{net}, while the opposite is true for grass PFTs. The ΔR_{net} for tree PFTs peaked at 5.4 Wm^{-2}, ΔR_{net} for grass PFTs reached -4.8 Wm^{-2}.

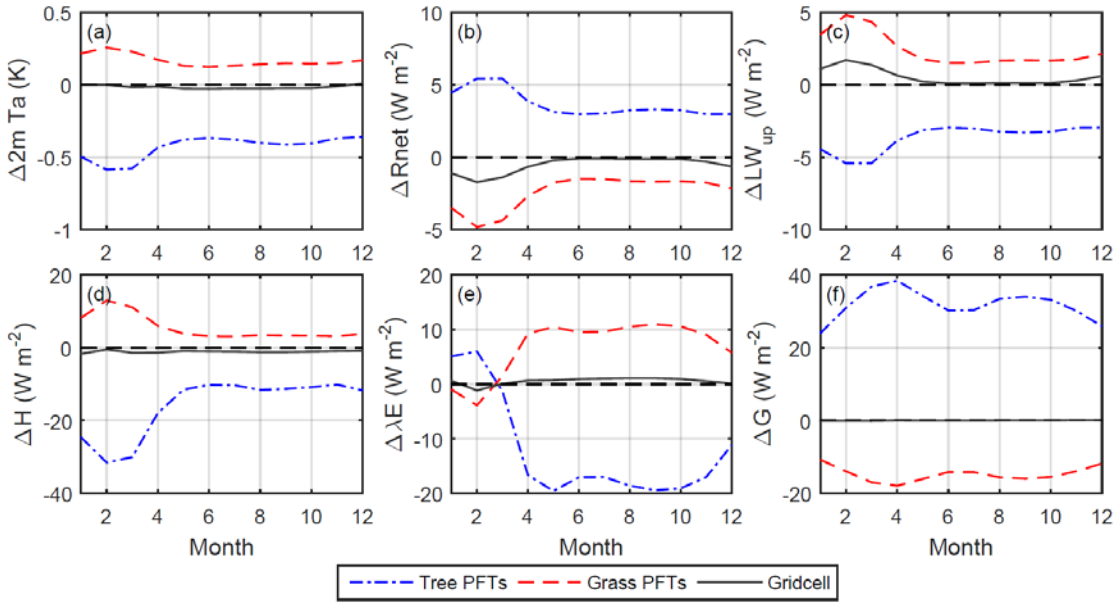

Figure 3.4. The monthly differences of (a) 2-m air temperature, (b) net radiation, (c) emitted longwave radiation, (d) albedo, (e) sensible heat flux, (f) latent heat flux, and (g) ground heat flux at the tree and grass PFT-level and grid cell-level for the tropical grid cell (6.13ºN, 288.75ºE). The monthly differences are averaged over 20 years (1991-2010).

There is some seasonality to the H and λE (Figure S3.4), due to a dry season from January to March and relatively wetter conditions from April to December. Although the sign of ΔH for both tree and grass PFTs does not change over the year, ΔH is largest in magnitude during the dry season (-31.5 Wm^{-2} for tree PFTs and13.0 Wm^{-2} for grass PFTs). In contrast to ΔH, the largest differences in λE for both tree and grass PFTs between the PFTCOL and CTRL simulations are observed during the wet season. The PFTCOL configuration results in a reduction of λE for tree PFTs and an increase in λE for grass PFTs over most of the year (March – December). The largest reduction in λE for tree PFTs between the PFTCOL and CTRL cases occurs in May: from 138.1 Wm^{-2} in the CTRL case to 118.5 Wm^{-2} (Figure S3.4) in the PFTCOL case. For grass PFTs, the $\Delta\lambda E$ peaked in September at 10.9 W m^{-2}.

In this tropical grid cell, large differences in the ground heat flux are observed between the two cases. In the CTRL case, G is positive (into the soil) year-round for grass PFTs (11.3 Wm^{-2} to 17.9 Wm^{-2}) and negative year-round for tree PFTs (-39.0 Wm^{-2} to -22.8 Wm^{-2}) (Figure S3.4). In the PFTCOL case, however, the monthly G for tree and grass PFTs ranges from -2.0 Wm^{-2} to 2.5 Wm^{-2}. Averaging over the entire year, the PFTCOL PFT-level G is nearly zero, while the CTRL case produces annual averages for G of -31.8 Wm^{-2} and 14.7 Wm^{-2} for tree and grass PFTs, respectively (Table 3.1). The largest differences are observed in April, with ΔG reaching 38.4 W m^{-2} for tree PFTs and -17.9 Wm^{-2} for grass PFTs.

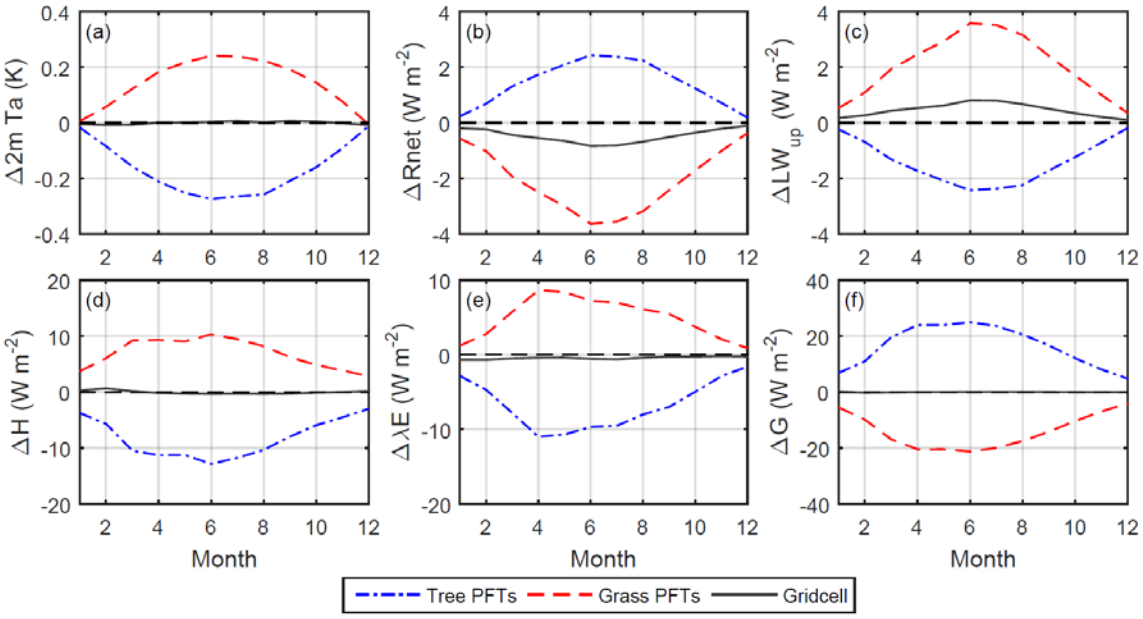

Figure 3.5. The same as Figure 3.4 except for the temperate grid cell (35.34ºN, 282.5ºE).

There is a distinct seasonality to the monthly differences between the PFTCOL and CTRL cases for the temperate grid cell, with the largest differences in all surface variables occurring during summer months (June – August; Figure 3.5). The magnitude of the differences tends to follow the seasonality of T_a and surface energy fluxes (Figure S3.5). The ΔT_a for tree PFTs is negative across all months, reaching -0.27 K in June, while ΔT_a for grass PFTs is positive for all months except December, peaking at 0.24 K. The seasonal pattern of PFT-level ΔR_{net} is driven primarily by $\Delta L\uparrow$, as at this latitude, snow cover is not yet a significant contributor to R_{net} in winter months.

The largest differences in the sensible heat, latent heat, and ground heat fluxes between the PFTCOL and CTRL cases in the temperate grid cell occur during spring and summer months, when fluxes are highest. During summer months, there was a 12 Wm^{-2} decrease in H for tree PFTs and a 10 Wm^{-2} increase for grass PFTs in the PFTCOL case relative to the CTRL case (Figure S3.5). The $\Delta\lambda E$ at the PFT-level is in the range of ±1 W m^{-2} to 11 W m^{-2} for both grass and tree PFTs.

The magnitude of ΔG is nearly double those of ΔH and $\Delta\lambda E$ for both tree and grass PFTs. In the CTRL case, the ground heat flux for tree PFTs is negative over the entire year, while G for grass PFTs is positive nine months out of the year (Figure S3.5), resulting in annual averages of -16.4 W m^{-2} and 14.0 W m^{-2} (Table 3.1). In contrast, G for each of the PFTs in the PFTCOL case exhibits a seasonal cycle (positive flux during summer months, negative flux during winter months) which averages out on an annual basis to be approximately zero (Figure S3.5, Table 3.1). Because of these differences in the seasonality of G between the PFTCOL and CTRL cases, ΔG is large, reaching 25.0 Wm^{-2} for grass PFTs and -21.2 Wm^{-2} for tree PFTs during the summer.

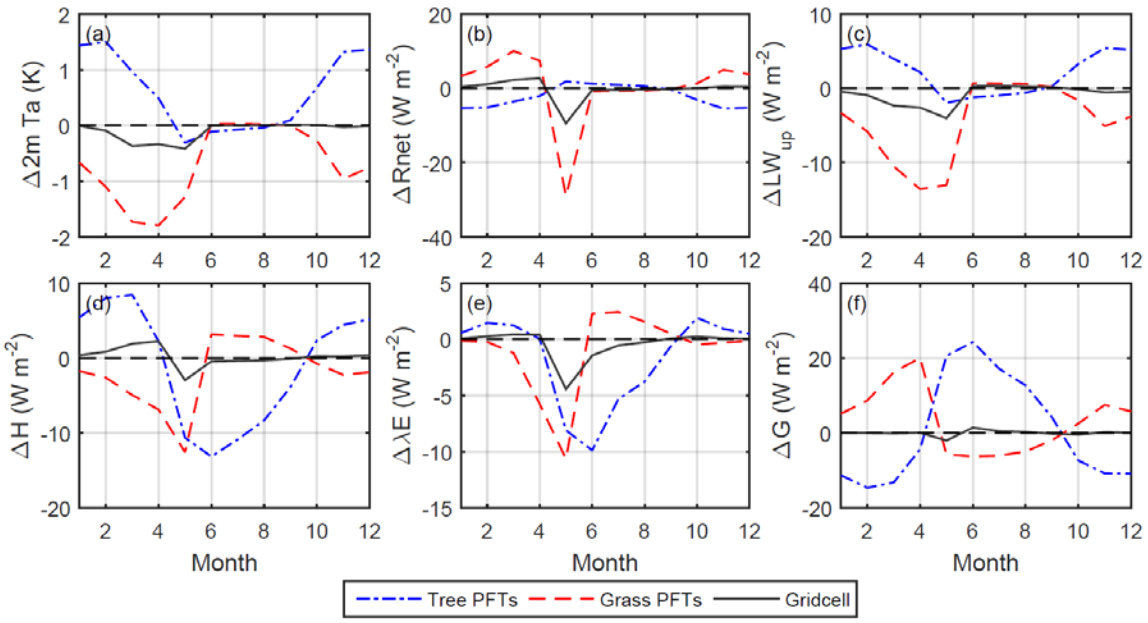

Figure 3.6. The same as Figure 3.4 except for the boreal grid cell (66.44ºN, 222.5ºE).

In the boreal grid cell, the seasonal patterns of air temperature and surface energy fluxes show two interesting differences compared to the temperate and tropical grid cells (Figure 3.6). First, the largest changes in air temperature between the PFTCOL and CTRL cases occur during winter months. In the PFTCOL case, tree PFTs become cooler during the spring/summer, and warmer during the fall and winter, with ΔT_a reaching 1.50 K in February. The ΔT_a for grass PFTs displays an opposite seasonal pattern of the tree PFTs, with slightly positive values from May through August, and negative values during the colder months of the year. The warming of grass PFTs during summer months in the PFTCOL case is minimal, but the cooling is substantial, with ΔT_a reaching -1.79 K in April.

Second, $\Delta K\uparrow$ becomes important to ΔR_{net} in the boreal grid cell. In particular, $\Delta K\uparrow$ of grass PFTs contributes significantly to ΔR_{net} in late spring. The ΔR_{net} for grass PFTs in May is -29.0 Wm^{-2}, resulting from a $\Delta L\uparrow$ of -13.0 W m^{-2} and a $\Delta K\uparrow$ of 42.0 Wm^{-2} (Figure S3.6). To put $\Delta K\uparrow$ in context with incoming shortwave radiation, the albedo of grass PFTs in May increased from 0.16 in the CTRL case to 0.27 in the PFTCOL case. Dividing the shared soil column into separate columns for each PFT affects snow depth and subsequently the vertical burial of vegetation by snow, since snow is a column-level variable. In the month of May in particular, deeper snow reduces the exposed leaf area index (LAI) of grass PFTs by 0.38 m^2 m^{-2}, while there is no change in the exposed LAI of tree PFTs.

A seasonal cycle exists for ΔH, $\Delta\lambda E$, and ΔG for tree and grass PFTs. Again, the largest change to the surface energy budget between the two cases is to the ground heat flux, with monthly ΔG for tree PFTs and grass PFTs reaching 24.3 W m^{-2} and 20.0 W m^{-2}, respectively. On an annual basis, however, ΔG is relatively small compared to the other two grid cells: 3.4 Wm^{-2} for grass PFTs and 0.5 Wm^{-2} for tree PFTs (Table 3.1).

		Grass PFTs								Tree PFTs							
grid location	case name	T_a	K↓	K↑	L↓	L↑	H	λE	G	T_a	K↓	K↑	L↓	L↑	H	λE	G
Boreal	PFTCOL	261.8	111.2	41.4	218	266.6	5.7	14.7	0.8	262.3	111.2	11.1	218	274.5	27.7	15.3	0.7
(66.44N,	CTRL	262.5	111.2	37.4	218	271.2	7.6	15.7	-2.6	261.7	111.2	11.2	218	272.2	28.6	17	0.2
222.5E)	Δ	-0.7	--	4	--	-4.6	-1.9	-1	3.4	0.6	--	-0.1	--	2.3	-0.9	-1.7	0.5
Temperate	PFTCOL	288.5	192.7	29.2	337.8	398.4	29.4	73.4	0.06	288.1	192.7	18	337.8	394.3	47.5	70.8	-0.02
(35.34N,	CTRL	288.3	192.7	29.2	337.8	396.4	22.5	68.5	14	288.3	192.7	18	337.8	395.7	55.7	77.6	-16.4
282.5E)	Δ	0.2	--	0	--	2	6.9	4.9	-13.94	-0.2	--	0	--	-1.4	-8.2	-6.8	16.38
Tropical	PFTCOL	300.6	207.3	30.7	429.2	470.8	31.7	103.3	-0.04	299.8	207.3	26.4	429.2	459.3	45.2	105.6	-0.03
(6.13N,	CTRL	300.5	207.3	30.7	429.2	468.4	26.2	96.5	14.7	300.2	207.3	26.4	429.2	463	61.2	117.7	-31.8
288.75E)	Δ	0.1	--	0	--	2.4	5.5	6.8	-14.74	-0.4	--	0	--	-3.7	-16	-12.1	31.77

Table 3.1. A summary of the annual 2-m air temperature (K) and surface energy fluxes (Wm^{-2}) for each of the three grid cells. The 20-year annual averages for the PFTCOL and CTRL simulations are shown, as well as the difference (Δ) between the two runs (PFTCOL – CTRL).

Diurnal

We focus on the diurnal patterns of ΔT_a and ΔG for each of the tropical, temperate, and boreal grid cells (Figures 3.7-3.8). The diurnal patterns and differences of these and other surface variables are given in Supplementary Figures S3.7-S3.12. The diurnal ΔT_a patterns are similar in the tropical and temperate grid cells, although they are more pronounced in the tropical grid cell (Figure 3.7). In the tropical grid cell, ΔT_a for tree PFTs is always negative, reaching -0.82 K during the night, while ΔT_a for grass PFTs is always positive, peaking at 0.25 K overnight. For the temperate grid cell, ΔT_a ranges from -0.40 K for tree PFTs and 0.32 K for grass PFTs. In the boreal grid cell, the hourly ΔT_a is always positive for tree PFTs (up to 0.73 K) and always negative for grass PFTs (up to -0.87 K).

The largest ΔG occurs during midday, when fluxes are the highest (Figure 3.8). The magnitude of ΔG overshadows those of the other surface energy fluxes, approximately double ΔH and $\Delta \lambda E$ and nearly ten times larger than ΔR_{net} (Figures S3.7-S3.12). In all three grid cells, midday G for tree PFTs is higher in the PFTCOL case relative to the CTRL case, while midday G for grass PFTs is reduced. For tree PFTs, midday ΔG peaks at 98.1 Wm^{-2}, 49.9 Wm^{-2}, and 12.4 Wm^{-2} for the tropical, temperate, and boreal grid cells, respectively. For grass PFTs, midday ΔG reaches -39.3 Wm^{-2}, -44.8 Wm^{-2}, and -2.9 Wm^{-2}.

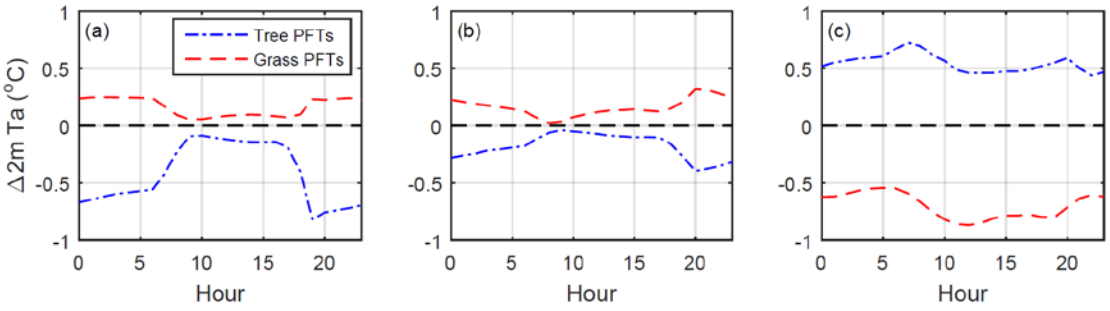

Figure 3.7. The hourly difference in 2-m air temperature for tree and grass PFTs for the (a) tropical, (b) temperate, and (c) boreal grid cells. The hourly differences are averaged over a single year (2010).

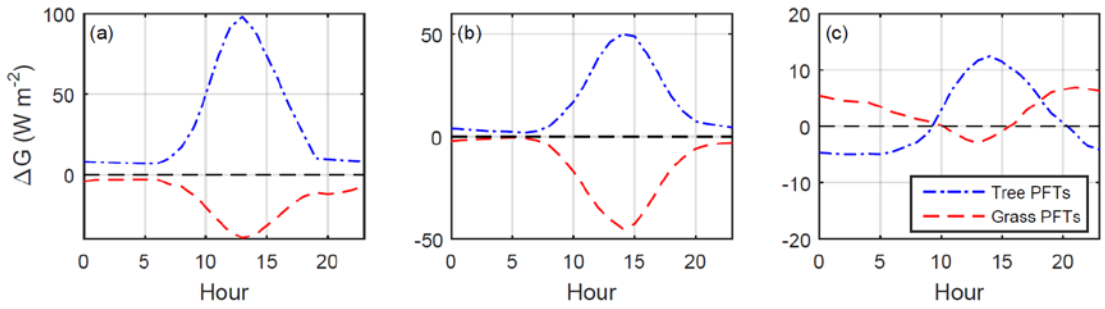

Figure 3.8. The hourly difference in the ground heat flux for tree and grass PFTs for the (a) tropical, (b) temperate, and (c) boreal grid cells. The hourly differences are averaged over a single year (2010).

Sub-grid land cover change comparison

Figure 3.9 presents the 20-year average (1991-2010) of the 2-m air temperature difference (ΔT_{GT}) between grass and tree PFTs within each grid cell for the CTRL and PFTCOL simulations. As previously stated, the ΔT_{GT} can be thought of as the effect of local-scale deforestation on surface air temperature. The PFTCOL simulation produces a latitudinal pattern of ΔT_{GT}, with a sub-grid cooling of more than 1.5 K in boreal regions and an average sub-grid warming in the tropics of approximately 0.6 K. The CTRL simulation produces a spatial pattern of ΔT_{GT} that is nearly opposite to that of the PFTCOL simulation. In the CTRL case, "deforestation" produces the largest warming in high latitudes, with regions of mild cooling scattered across the globe.

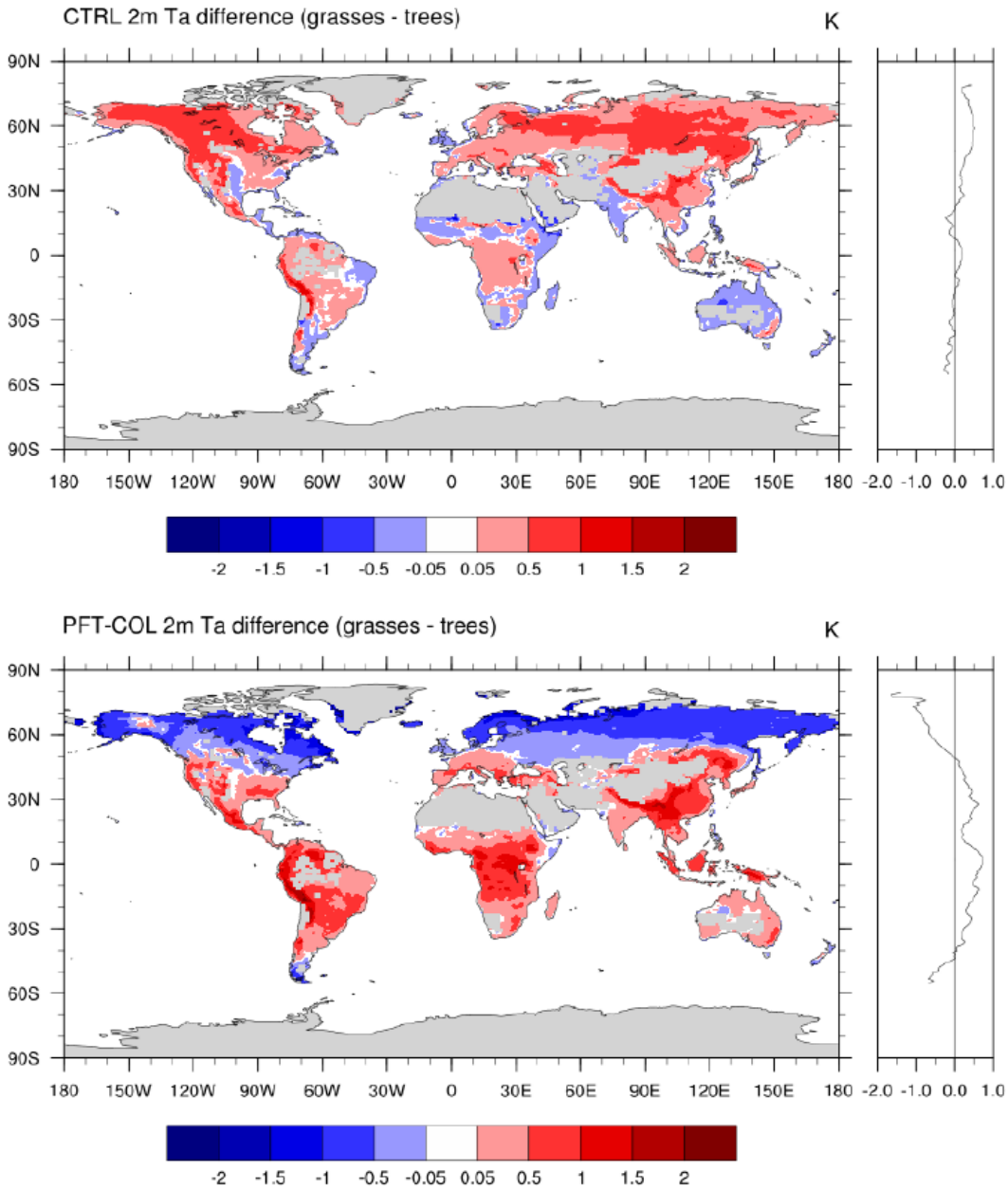

Figure 3.9. The 20-year (1991-2010) difference in 2-m air temperature (grass PFTs – tree PFTs) for the CTRL case (top) and the PFTCOL case (bottom).

Discussion

Soil column effect on sub-grid temperature

Land models typically produce a great amount of sub-grid information. The utility of PFT-level data in CLM and possibly other land models is hindered by the implicit transfer of energy through the shared soil column, and thus the inability to completely separate a single PFT from the others. By modifying the land surface configuration of CLM in such a way so that each PFT within the vegetated land unit was assigned its own soil column, we showed that each PFT is isolated from the others, allowing for analysis at the PFT-level.

The ΔT_{GT} results from the PFTCOL simulation differ substantially from the CTRL simulation, but agree closely with previous studies in both magnitude and latitudinal pattern. The PFTCOL results are in agreement with the observational studies of *Lee et al.* [2011] and *Zhang et al.* [2014] who compared surface air temperature using site pairs of measurements over forests and open lands, and found that the magnitude of cooling in high latitudes was higher than the magnitude of warming in low latitudes in both the Americas and Asia. Additionally, these initial results are in general agreement with the annual sub-grid canopy air temperature difference (crop – natural vegetation) calculated by *Malyshev et al.* [2015]. They found that, compared with natural vegetation, crops produce a local cooling in high latitudes (above approximately 45^{o}N) and warming in mid to low latitudes. The separate soil columns present a new opportunity to isolate the effects of land cover and land cover change on surface climate in GCM experiments.

Soil column effect on PFT surface energy balance

We found that soil column configuration influenced net radiation, turbulent fluxes, and the ground heat flux at the PFT level, and the difference between the PFTCOL and CTRL simulations increased as the grid cell fraction of the PFT decreased (Figure S3.13). With regard to the surface energy budget, the largest difference between the PFTCOL and CTRL simulations was found for the ground heat flux (Table 3.1). The annual mean *G* at the PFT level in the CTRL

case is significantly larger than expected in a relatively unchanging climate. By allowing the grass and tree PFTs to share the same soil column, a substantial amount of heat is entering the soil below the grass and coming out of the soil below the tree PFTs. Because there was little to no change in the column averaged soil temperature despite these large ground heat fluxes, we infer that heat was being transferred from one PFT to another through the shared soil column. Measurements of horizontal soil temperature gradients in heterogeneous landscapes are needed to understand the magnitude of horizontal ground fluxes between different land cover types. However, the CTRL and PFTCOL configurations cannot answer this question, because neither configuration allows for horizontal heat transfer between different PFTs.

The ground heat flux in CLM is calculated as the residual of the surface energy balance equation [*Oleson et al.*, 2013]. Therefore, the nonzero G in the CTRL simulation had to have been made up for by smaller or larger PFT-level sensible and latent heat fluxes. The magnitude of changes in these fluxes between the PFTCOL and CTRL cases was significant: In the tropical grid cell, for example, H and λE for tree PFTs decreased by 26% and 10%, respectively, while H and λE for grass PFTs increased by 21% and 7% (Figure 3.10, Table 3.1). We can infer that the turbulent fluxes in the CTRL case are biased at the PFT-level because large negative or positive residual ground heat fluxes are produced. Yet, these biases seem to offset each other, since there are only minimal differences in the grid cell-averages. As will be discussed in the following section, this is not to say that the PFTCOL results do not have their own biases. However, we propose that the PFTCOL configuration is useful for diagnosing model biases at their source: the PFT-level.

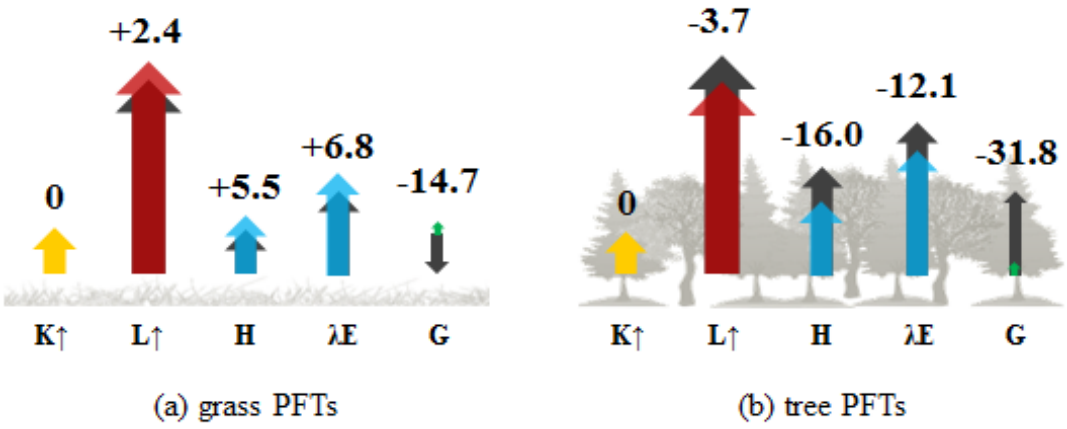

Figure 3.10. The 20-year annual mean difference (PFTCOL-CTRL) in surface energy fluxes for (a) grass PFTs and (b) tree PFTs in the tropical grid cell. The colored arrows represent fluxes from the PFTCOL case, while grey arrows represent fluxes from the CTRL case. Units are in Wm^{-2}.

Model evaluation and validation

Our results indicate that the PFTCOL land surface configuration can also be used for larger-scale evaluation and validation of PFT-level processes. The configuration of the PFTCOL case can be thought of as an expansion of CLM run in single-point mode. Single-point simulations consist of a single point with one PFT on a single column, forced with a prescribed atmospheric dataset or flux tower [*Oleson et al.*, 2013]. Often, single-point simulations are used for evaluating specific vegetation types, testing new model schemes, or running CLM over a specific site with observed data [e.g. *Bonan et al.*, 2014; *M Chen et al.*, 2015]. Because CLM calculates surface variables at the PFT-level, model evaluation at the PFT-level may be able to identify potential errors at their source and therefore improve both sub-grid and grid cell-averaged output. It should be noted, however, that the separate columns increased the computational time of the CLM simulation, with the PFTCOL case costing approximately 11% more than the CTRL case, a relatively minor slowdown when running CLM offline.

The value of this configuration for validation is highlighted through our identification of potential model biases in tropical regions. In the tropics, our PFT-level data shows that CLM does not reproduce observed differences in energy partitioning between forested and deforested areas. Comparative flux measurements by *von Randow et al.* [2004] show that the difference in the latent heat flux between a forest and pasture site ranges from 21.5 Wm^{-2} in the wet season to 44.7 Wm^{-2} in the dry season. From our PFTCOL simulation, the difference in λE between grass and forest PFTs was less than 10 Wm^{-2} across all seasons (Figure S3.1). The small contrast in λE between tropical PFTs results in an inaccurate partitioning of the biophysical effects on surface temperature. From flux tower observations, *Lee et al.* [2011] found that deforested tropical sites were nearly 2 K warmer than tropical forests, attributable in large part to changes in the Bowen ratio between the forested and open sites. In paired CLM4.5 simulations by *L Chen and*

Dirmeyer [2016], however, there was higher ET in the tropics in the deforestation scenario, resulting in a negative contribution of the Bowen ratio effect on surface temperature.

In tropical regions, observations show that forest transpiration is sustained during the dry season and the seasonal change in energy partitioning between H and λE is small [*da Rocha et al.*, 2004; *von Randow et al.*, 2004]. In contrast, observations over deforested areas show a reduced λE during the dry season, accompanied by an increase in H [*von Randow et al.*, 2004]. *von Randow et al.* [2004] show that the Bowen ratio ($\beta = H/\lambda E$) is relatively constant over a tropical forest across a year, varying between 0.3-0.4, while the seasonal β at a nearby pasture site varies from 0.55 during the wet season to 0.77 during the dry season. From the tropical grid cell in this analysis, the annual PFT-level Bowen ratios from the PFTCOL simulation are in better agreement with the measurements of *von Randow et al.* [2004]. Despite improvements in the PFTCOL case, the β of tree PFTs displayed a much larger seasonal change, from 0.33 in the wet season to 0.76 in the dry season, than those reported from field observations, showing that the energy partitioning between sensible and latent heat fluxes at the PFT-level in CLM4.5 is inconsistent with field observations.

Through the PFT-level analysis, we identified two potential areas of focus for improving PFT-level latent heat flux and energy partitioning in the tropical zone. First, such an improvement may be accomplished through an improved parameterization of below-ground processes. The vertical root distribution affects the rates at which plants extract water from different soil layers for transpiration [*Zeng*, 2001]. The effective rooting depth, defined here as the depth at 99% of the cumulative root fraction, for each of the four PFTs in the tropical grid cell (two grasses, two trees) is given in Table 3.2. Using the plant-dependent root distribution parameters adopted from *Zeng* [2001], the rooting depths of the C4 grass, C3 grass, broadleaf evergreen trees (BET), and broadleaf deciduous trees (BDT) are 2.3 m, 1.4 m, 3.8 m, and 2.3 m. The similar rooting distributions of tree and grass PFTs are unable to simulate observed differences in soil moisture

between these different land cover types. *von Randow et al.* [2004] found that water storage in the 0-2 m soil layer ranged from approximately 380 mm in the dry season to 800 mm in wet season in the forest, and from 420 mm to 700 mm in the pasture, and water storage in the 2.0-3.4 m soil layer in the forest ranged from 200 mm to 500 mm and from 400 mm to 550 mm in the pasture. The large seasonal amplitude of the 2.0-3.4 m layer soil moisture in the forest compared to the minor seasonal variations in the lower soil layer in the pasture indicates larger root uptake from below 2 m in the forest, compared to the pasture. For comparison, little contrast is seen in the modeled soil moisture between grass and tree PFTs (Table 3.2). From this analysis, extending the rooting system and improving root parameterizations of the tree PFTs may improve the seasonality of energy partitioning of the tree PFTs.

			Wet season (Jul – Sep)					Dry Season (Jan – Mar)				
	Root depth (m)		β			Soil water content (mm)		β			Soil water content (mm)	
	PFT #1	PFT #2	PFTCOL	CTRL	Δ	0 - 2.3 m	2.3 - 3.8 m	PFTCOL	CTRL	Δ	0 - 2.3 m	2.3 - 3.8 m
Grass PFTs	2.3[a]	1.4[b]	0.24	0.23	0.01	833	593	0.58	0.44	0.14	536	521
Tree PFTs	3.8[c]	2.3[d]	0.33	0.37	-0.04	835	589	0.76	1.14	-0.38	566	520

a) C4 grass, b) C3 grass/crop, c) broadleaf evergreen tree, and d) broadleaf deciduous tree.

Table 3.2. The root depth, Bowen ratio (β) and soil water content for PFTs in the tropical grid cell. All values are averaged over 20 years (1991-2010), and divided into wet and dry seasons.

Second, revisions to canopy parameterizations may improve energy partitioning of PFTs in the tropics. The empirical Ball-Berry stomatal conductance model [*Ball et al.*, 1987] is used in CLM4.5 to simulate biotic regulation of ET, but there is some uncertainty as to how to represent stomatal closure as soil moisture declines [*Bonan et al.*, 2014]. Adjusting PFT-dependent photosynthetic parameters that control stomatal resistance has been shown to reduce or offset model errors [*Bonan et al.*, 2011]. Refinement of the canopy model in CLM is another avenue for potential improvements. For example, a multi-layer canopy model by [*Bonan et al.*, 2014] performed better than the CLM Ball-Berry model in flux tower simulations, particularly during times of moisture stress. Additionally, the lack of contrast between the λE of tree and grass PFTs may be due to excessively high ground evaporation and canopy transpiration from grass PFTs [*L Chen and Dirmeyer*, 2016]. *Swenson and Lawrence* [2014] have shown that soil evaporation in CLM4.5 is biased high over sparse canopies. Revisions to soil evaporation in CLM should result in further improvements.

Column effect on coupled simulations and carbon balance

Despite large changes at the PFT-level between the PFTCOL and CTRL simulations, the grid cell-averaged differences between the two cases were minimal, because the changes in the surface variables for tree PFTs were offset by changes in the other direction for grass PFTs. Therefore, a PFTCOL configuration of CLM4.5 coupled to the atmospheric model will not significantly modify atmospheric processes. However, there is evidence that the representation of the land surface in terrestrial models affects the carbon balance at both the PFT and grid cell levels. *Li and Arora* [2012] compared the carbon balance of a land surface model using both the composite and mosaic approaches, finding that the grid cell-averaged carbon flux differed between the two approaches by as much as 41% for net primary productivity, 16% for vegetation biomass, and 46% for soil carbon mass. Additionally, *Melton and Arora* [2014] found that land model surface configuration had a significant influence on the modeled response of terrestrial carbon to land

cover change, with the composite and mosaic approaches differing by 16% in estimates of the terrestrial carbon sink. This topic has not yet been investigated using CLM; however, as with the physical surface processes, individual columns may prove as a useful tool for model evaluation.

Conclusions

We found that the spatial pattern and magnitude of ΔT_{GT} (2-m air temperature difference between grass and tree PFTs) from the PFTCOL simulation agreed closely with previously published studies, with grasses typically exhibiting lower mean annual temperatures in boreal regions and higher temperatures in the tropics than forests. The CTRL case was not able to simulate these same patterns at the sub-grid level.

Between the PFTCOL and CTRL cases, there were large differences in 2-m air temperature and the ground heat flux (G) at the PFT-level. As G is calculated as the residual of the surface energy budget, we infer that the latent and sensible heat fluxes in the CTRL case were biased either high or low depending on the large negative or positive ground heat flux. The large PFT-level ground heat fluxes in the CTRL case imply a transfer of energy between PFTs through the shared soil column, complicating the interpretation of PFT-level fluxes. This issue does not exist in the PFTCOL configuration, which presents the opportunity to both evaluate the simulation of PFT-level processes and to compare biophysical processes between different vegetation types.

Land models produce a large amount of sub-grid information; however, PFT-level data are rarely used in GCM experiments. Here, we show that the PFTCOL configuration appears to be promising for evaluation of biophysical land cover change impacts and for assessment of PFT-level representations of fluxes.

Acknowledgements

We would like to acknowledge high-performance computing support from Yellowstone (ark:/85065/d7wd3xhc) provided by NCAR's Computational and Information Systems Laboratory, sponsored by the National Science Foundation. We would also like to acknowledge financial support from Yale University and NCAR's ASP Graduate Visitor Program. The Community Earth System Model is freely available at http://www.cesm.ucar.edu/models/cesm1.2/. The modified code and data used for this analysis is available from authors upon request (natalie.schultz@yale.edu). We thank two anonymous reviewers whose comments helped us improve this paper.

Supporting Information

The supporting information for this chapter contains figures that include global maps of the PFT-level differences in air temperature and surface energy fluxes, the monthly and hourly surface temperature and energy fluxes for the PFTCOL and CTRL cases and the atmospheric forcing data for each of the three grid cells presented in the main text: tropical (grid center at 6.13^{o}N, 288.75^{o}E), temperate (35.34^{o}N,282.5^{o}E), and boreal (66.44^{o}N, 222.5^{o}E), and the relationship between PFT fraction and the difference in PFT-level variables between the two simulations. All figures were created following the methods described in the main text. Supplemental figures S1 and S2 present global maps of the data presented as zonal means in the main text. Figure S3 presents the atmospheric forcing data for each grid cell. Supplemental figures S4 to S6 present the monthly variations of surface variables from each simulation. Figures S7 to S9 present the hourly variations and differences between the two cases for each of the three grid cells. Figure S10 shows the difference in PFT-level variables as a function of grid cell fraction. Table S1 provides the PFT fractions in each of the three grid cells.

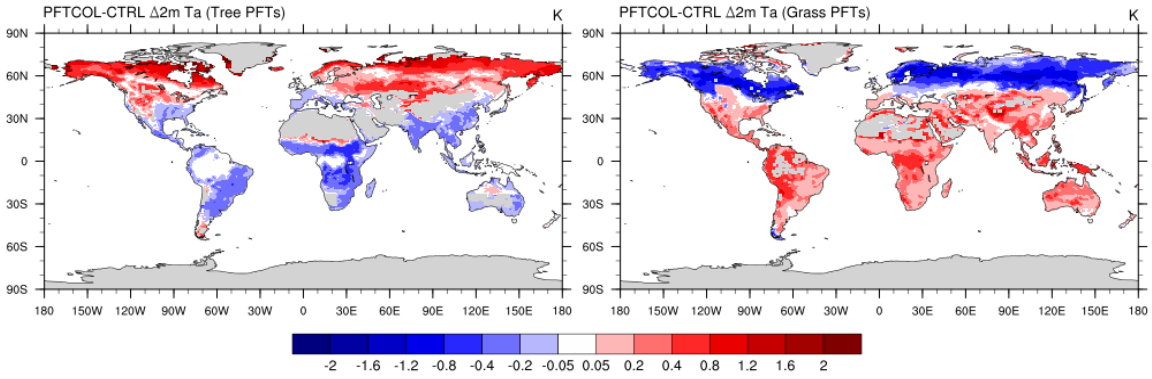

Figure S3.1. The spatial distribution of the difference in 2m surface air temperature for tree and grass PFTs between the PFTCOL and CTRL simulations. The zonal means are presented in Figure 1 in the main text.

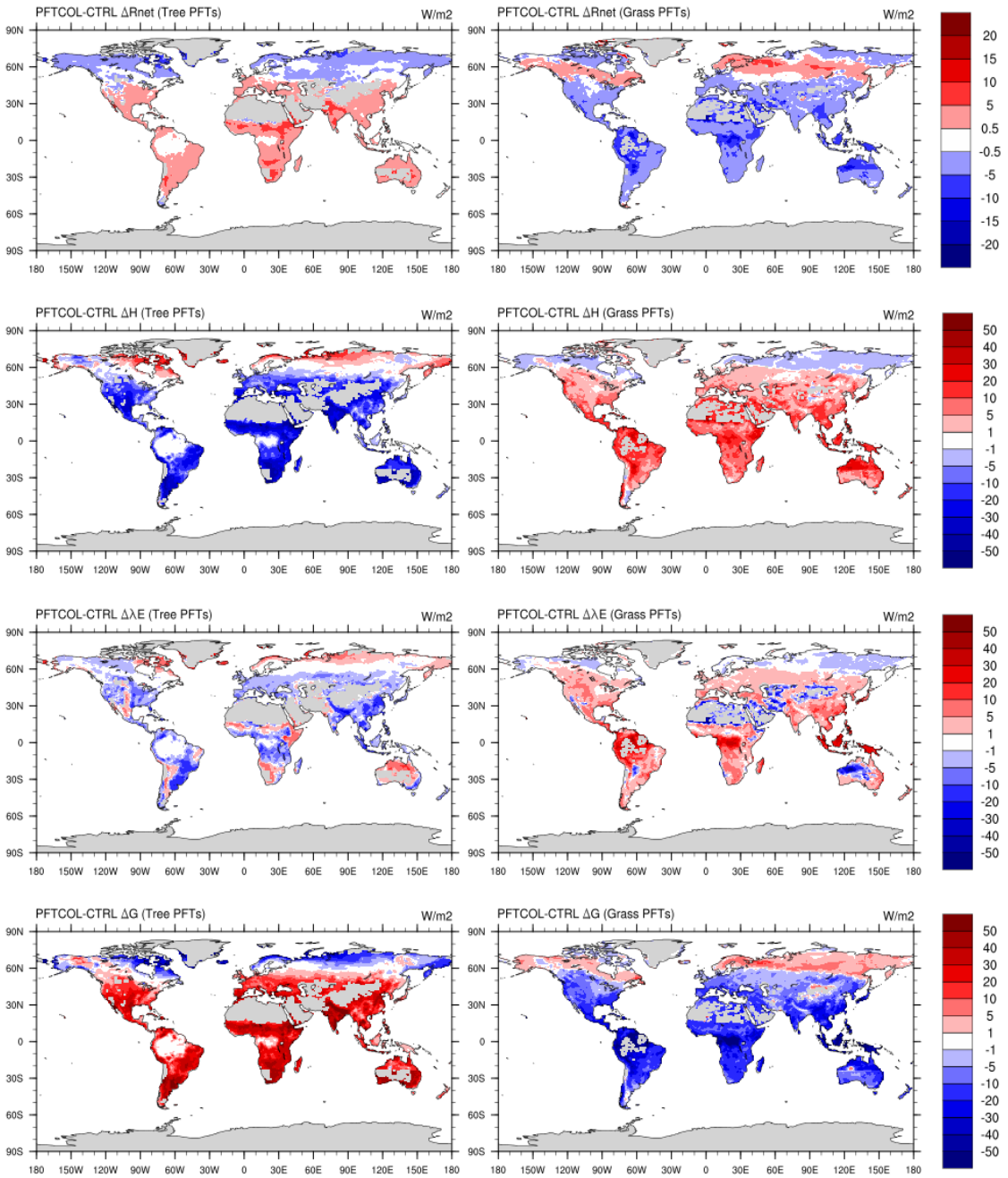

Figure S3.2. The spatial distribution of the difference in net radiation, sensible heat flux, latent heat flux, and the ground heat flux for tree and grass PFTs between the PFTCOL and CTRL simulations. The zonal means are presented in Figure 2 in the main text.

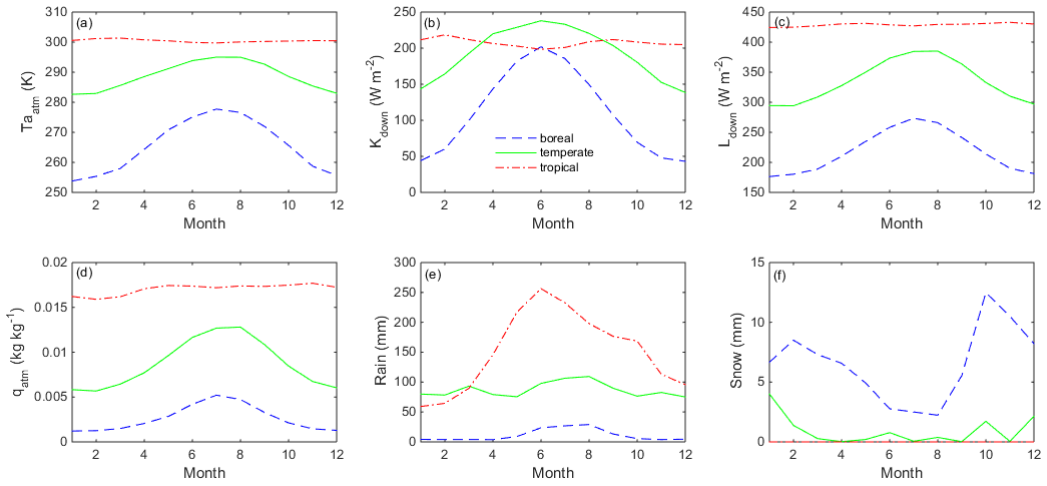

Figure S3.3. The 20-year (1991-2010) monthly mean values of the atmospheric forcing data (at reference height of 30m) used to drive CLM for each of the three grid cells.

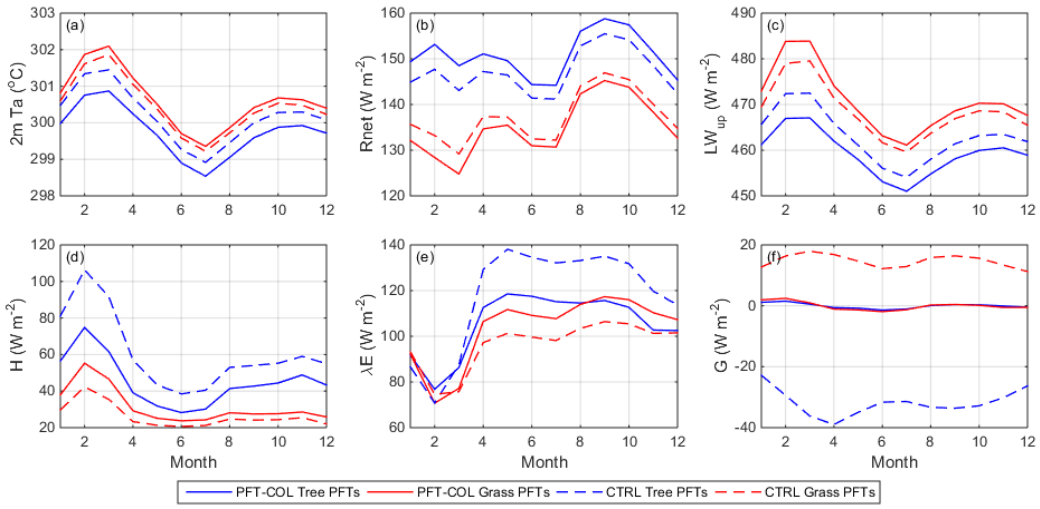

Figure S3.4. The monthly values of (a) 2-m air temperature, (b) net radiation, (c) emitted longwave radiation, (d) sensible heat flux, (e) latent heat flux, and (f) ground heat flux at the tree and grass PFT-level and grid cell-level for the tropical grid cell (6.13°N, 288.75°E). The monthly values are averaged over 20 years (1991-2010).

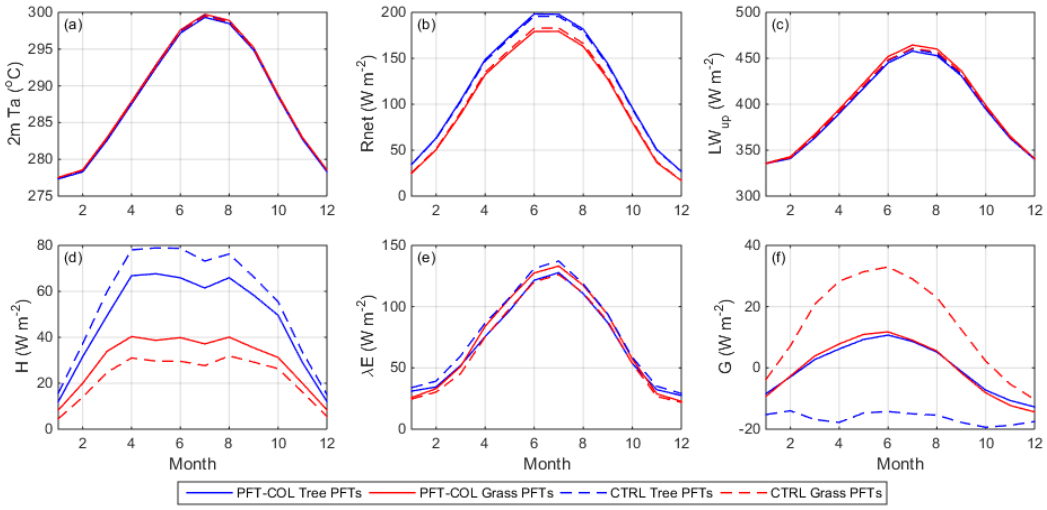

Figure S3.5. Same as Figure S3.4, but for the temperate grid cell (35.34ºN, 282.5ºE).

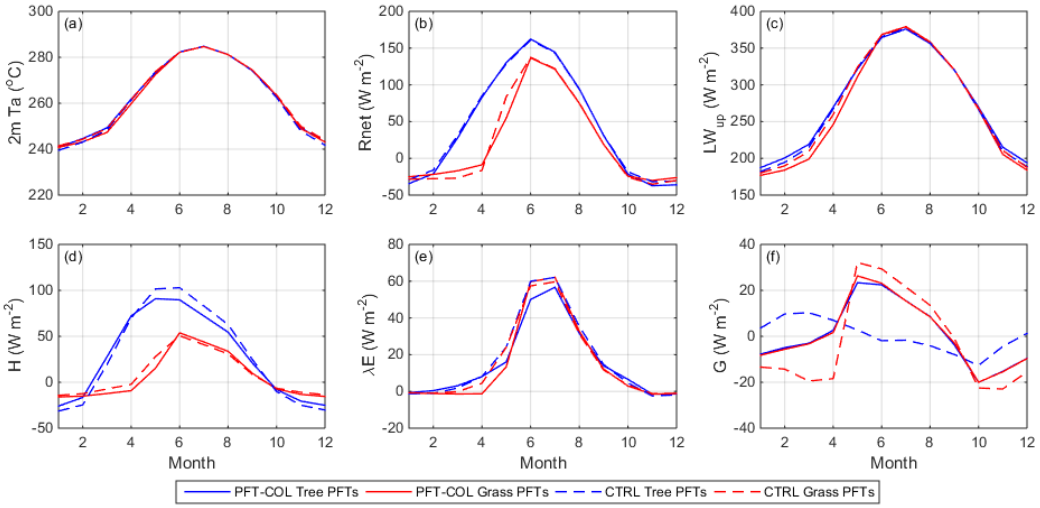

Figure S3.6. Same as Figure S3.4, but for the boreal grid cell (66.44ºN, 222.5ºE).

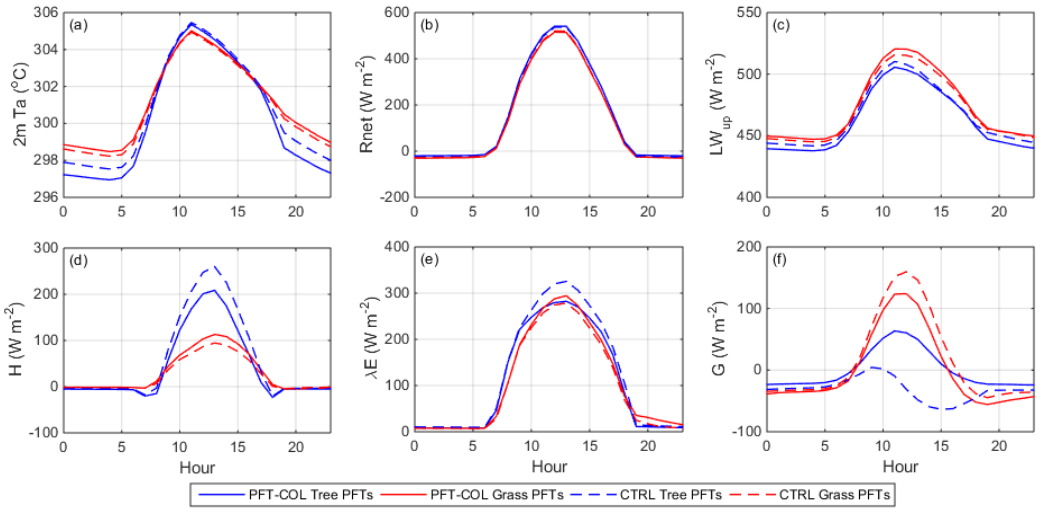

Figure S3.7. The hourly values of (a) 2-m air temperature, (b) net radiation, (c) emitted longwave radiation, (d) albedo, (e) sensible heat flux, (f) latent heat flux, and (g) ground heat flux at the tree and grass PFT-level for the tropical grid cell (6.13ºN, 288.75ºE). The hourly values are averaged over one year (2010).

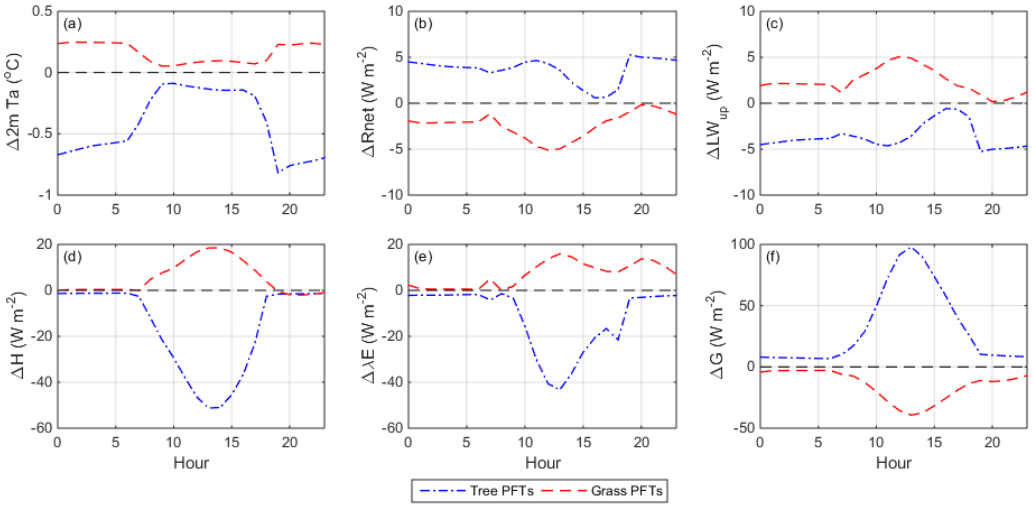

Figure S3.8. The hourly differences of (a) 2-m air temperature, (b) net radiation, (c) emitted longwave radiation, (d) albedo, (e) sensible heat flux, (f) latent heat flux, and (g) ground heat flux at the tree and grass PFT-level for the tropical grid cell (6.13°N, 288.75°E). The hourly differences are averaged over one year (2010).

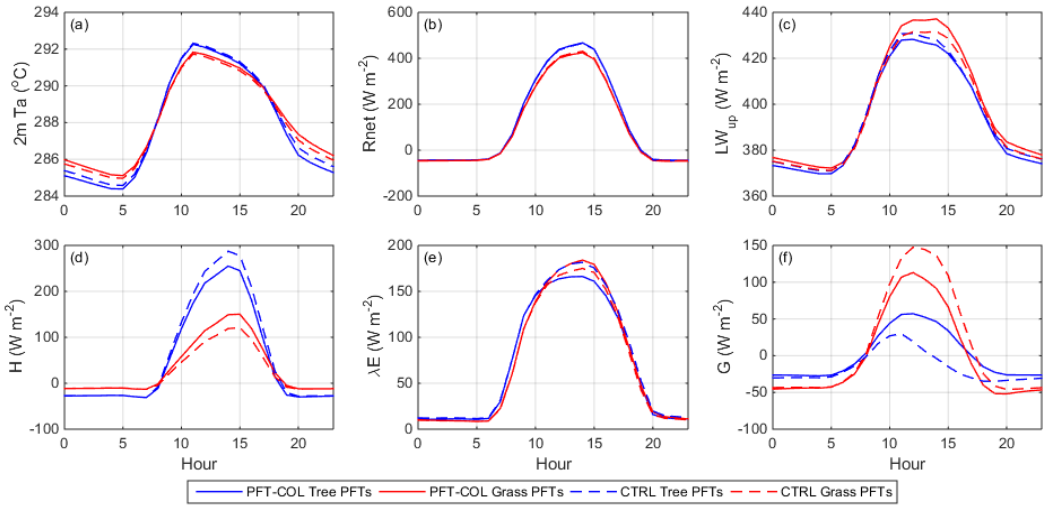

Figure S3.9. Same as Figure S3.7, but for the temperate grid cell (35.34ºN, 282.5ºE).

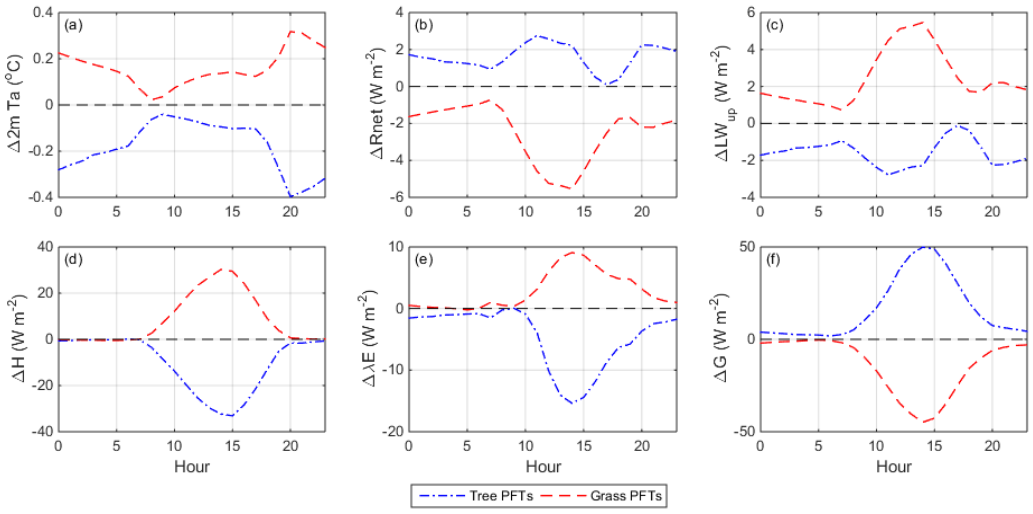

Figure S3.10. Same as Figure S3.8, but for the temperate grid cell (35.34°N, 282.5°E).

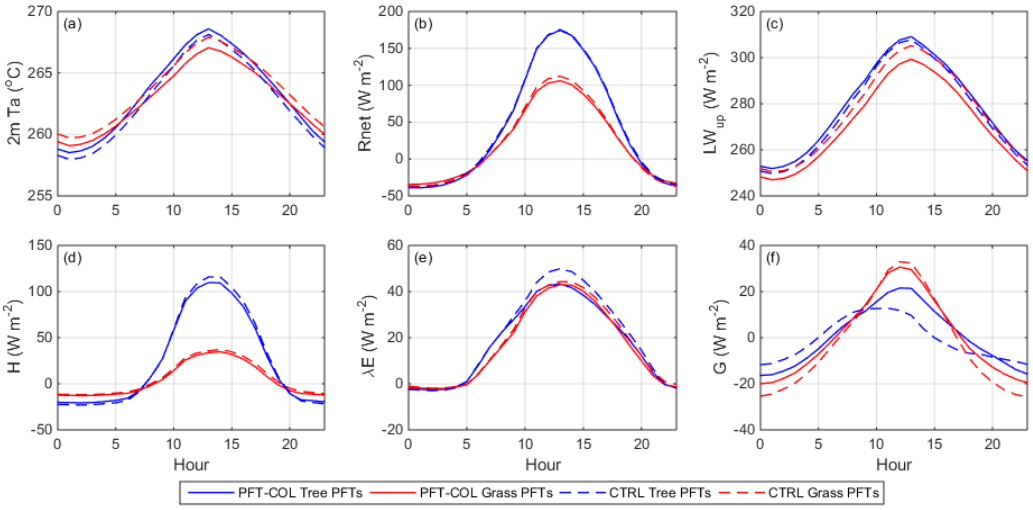

Figure S3.11. Same as Figure S3.7, but for the boreal grid cell (66.44ºN, 222.5ºE).

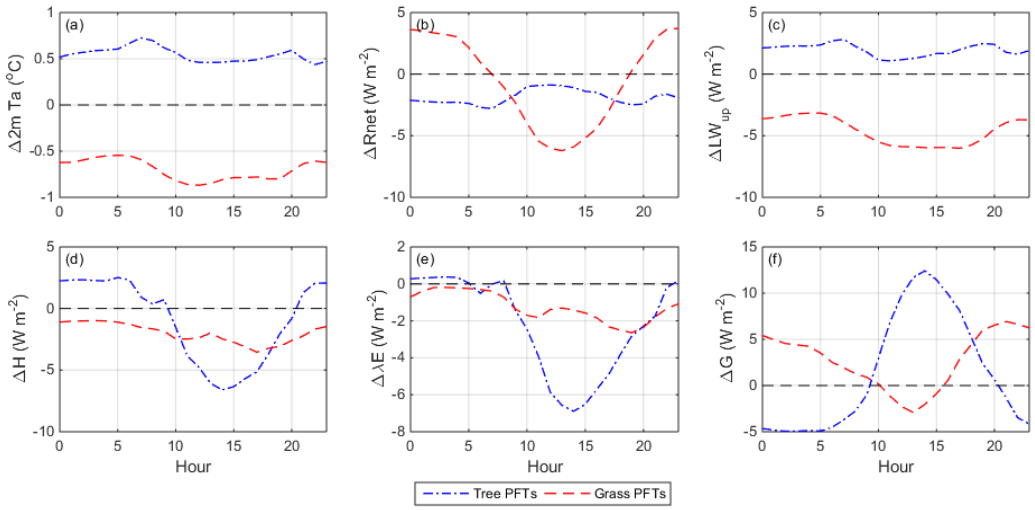

Figure S3.12. Same as Figure S3.8, but for the boreal grid cell (66.44ºN, 222.5ºE).

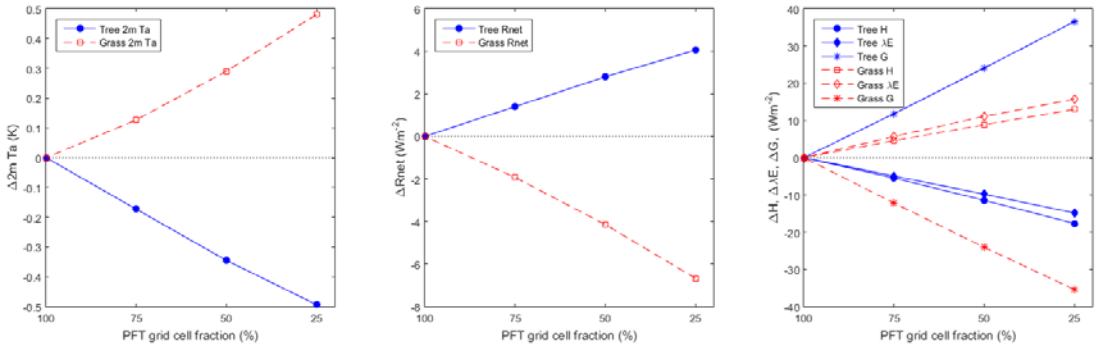

Figure S3.13. The difference in air temperature, net radiation, sensible, latent, and ground heat fluxes between the PFTCOL and CTRL simulations as a function of PFT grid cell percentage. Single point simulations were run on the tropical grid cell, with PFT fractions for grass (C4 grass) and tree (broadleaf evergreen) fractions ranging between 25 and 100%. At 100% PFT fraction, the CTRL case PFTs equaled the PFTCOL case PFTs. The differences increased as the fraction decreased.

Plant functional type	Boreal	Temperate	Tropical
Bare	0.016	0	0.004
Needleleaf evergreen, temperate	0	**0.308**	0
Needleleaf evergreen, boreal	**0.241**	0	0
Needleleaf deciduous, boreal	0	0	0
Broadleaf evergreen, tropical	0	0	**0.241**
Broadleaf evergreen, temperate	0	0	0
Broadleaf deciduous, tropical	0	0	**0.062**
Broadleaf deciduous, temperate	0	**0.152**	0
Broadleaf deciduous, boreal	**0.004**	0	0
Broadleaf evergreen shrub, temperate	0	0	0
Broadleaf deciduous shrub, temperate	0	0.001	0
Broadleaf deciduous shrub, boreal	0.410	0	0
C3 arctic grass	**0.328**	0	0
C3 non-arctic grass	0	**0.190**	0
C4 grass	0	**0.099**	**0.685**
C3 generic crop	0	**0.247**	**0.008**

Table S3.1. The fraction of PFTs in each of the three grid cells examined in this study.

References

Arain, M. A., E. J. Burke, Z.-L. Yang, and W. J. Shuttleworth (1999), Implementing surface parameter aggregation rules in the CCM3 global climate model: regional responses at the land surface, *Hydrology and Earth System Science*, *3*(4), 463-476.

Bala, G., K. Caldeira, M. Wickett, T. J. Phillips, D. B. Lobell, C. Delire, and A. Mirin (2007), Combined climate and carbon-cycle effects of large-scale deforestation, *Proceedings of the National Academy of Sciences of the United States of America*, *104*(16), 6550-6555, doi:10.1073/pnas.0608998104.

Ball, J. T., I. E. Woodrow, and J. A. Berry (1987), A model predicting stomatal conductance and its contribution to the control of photosynthesis under different environmental conditions, in *Progress in Photosynthesis Research*, edited by J. Biggins, pp. 221-224, Kluwer Academic Publishers Group, The Netherlands.

Bonan, G. B. (2008), Forests and climate change: forcings, feedbacks, and the climate benefits of forests, *Science*, *320*(5882), 1444-1449, doi:10.1126/science.1155121.

Bonan, G. B., P. J. Lawrence, K. W. Oleson, S. Levis, M. Jung, M. Reichstein, D. M. Lawrence, and S. C. Swenson (2011), Improving canopy processes in the Community Land Model version 4 (CLM4) using global flux fields empirically inferred from FLUXNET data, *Journal of Geophysical Research*, *116*(G2), doi:10.1029/2010jg001593.

Bonan, G. B., M. Williams, R. A. Fisher, and K. W. Oleson (2014), Modeling stomatal conductance in the earth system: linking leaf water-use efficiency and water transport along the soil–plant–atmosphere continuum, *Geoscientific Model Development*, *7*(5), 2193-2222, doi:10.5194/gmd-7-2193-2014.

Chen, L., and P. A. Dirmeyer (2016), Adapting observationally based metrics of biogeophysical feedbacks from land cover/land use change to climate modeling, *Environmental Research Letters*, *11*(3), 034002, doi:10.1088/1748-9326/11/3/034002.

Chen, M., T. J. Griffis, J. M. Baker, J. D. Wood, and K. Xiao (2015), Simulating crop phenology in the Community Land Model and its impact on energy and carbon fluxes, *Journal of Geophysical Research: Biogeosciences*, *120*, 310-325, doi:10.1002/.

Ciais, P., et al. (2013), Carbon and Other Biogeochemical Cycles, in *Climate Change 2013: The Physical Science Basis. Contribution of Working Group I to the Fifth Assessment Report of the Intergovernmental Panel on Climate Change*, edited by T. F. Stocker, D. Qin, G.-K. Plattner, M. Tignor, S. K. Allen, J. Boschung, A. Nauels, Y. Xia, V. Bex and P. M. Midgley, Cambridge University Press, United Kingdom, UK and New York, NY, USA.

da Rocha, H. R., M. L. Goulden, S. D. Miller, M. C. Menton, L. D. V. O. Pinto, H. C. de Freitas, and A. M. e Silva Figueira (2004), Seasonality of water and heat fluxes over a tropical forest in Eastern Amazonia, *Ecological Applications*, *14*(4), S22-S32.

Davin, E. L., and N. de Noblet-Ducoudré (2010), Climatic Impact of Global-Scale Deforestation: Radiative versus Nonradiative Processes, *Journal of Climate*, *23*(1), 97-112, doi:10.1175/2009jcli3102.1.

de Noblet-Ducoudré, N., et al. (2012), Determining Robust Impacts of Land-Use-Induced Land Cover Changes on Surface Climate over North America and Eurasia: Results from the First Set of LUCID Experiments, *Journal of Climate*, *25*(9), 3261-3281, doi:10.1175/jcli-d-11-00338.1.

Deng, B., S. Liu, W. Xiao, W. Wang, J. Jin, and X. Lee (2013), Evaluation of the CLM4 Lake Model at a Large and Shallow Freshwater Lake*, *Journal of Hydrometeorology*, *14*(2), 636-649, doi:10.1175/jhm-d-12-067.1.

Hurrell, J. W., et al. (2013), The Community Earth System Model: A Framework for Collaborative Research, *Bulletin of the American Meteorological Society*, *94*(9), 1339-1360, doi:10.1175/bams-d-12-00121.1.

Koster, R. D., and M. J. Suarez (1992), A comparative analysis of two land surface heterogeneity representations, *Journal of Climate*, *5*, 1379-1390.

Lawrence, D. M., et al. (2011), Parameterization improvements and functional and structural advances in Version 4 of the Community Land Model, *Journal of Advances in Modeling Earth Systems*, *3*(3), doi:10.1029/2011ms000045.

Lawrence, P. J., and T. N. Chase (2007), Representing a new MODIS consistent land surface in the Community Land Model (CLM 3.0), *Journal of Geophysical Research*, *112*(G1), doi:10.1029/2006jg000168.

Lawrence, P. J., and T. N. Chase (2010), Investigating the climate impacts of global land cover change in the community climate system model, *International Journal of Climatology*, *30*(13), 2066-2087, doi:10.1002/joc.2061.

Lee, X., et al. (2011), Observed increase in local cooling effect of deforestation at higher latitudes, *Nature*, *479*(7373), 384-387, doi:10.1038/nature10588.

Li, R., and V. K. Arora (2012), Effect of mosaic representation of vegetation in land surface schemes on simulated energy and carbon balances, *Biogeosciences*, *9*(1), 593-605, doi:10.5194/bg-9-593-2012.

Mahmood, R., et al. (2014), Land cover changes and their biogeophysical effects on climate, *International Journal of Climatology*, *34*, 929-953.

Malyshev, S., E. Shevliakova, R. J. Stouffer, and S. W. Pacala (2015), Contrasting Local versus Regional Effects of Land-Use-Change-Induced Heterogeneity on Historical Climate: Analysis with the GFDL Earth System Model, *Journal of Climate*, *28*(13), 5448-5469, doi:10.1175/jcli-d-14-00586.1.

Melton, J. R., and V. K. Arora (2014), Sub-grid scale representation of vegetation in global land surface schemes: implications for estimation of the terrestrial carbon sink, *Biogeosciences*, *11*(4), 1021-1036, doi:10.5194/bg-11-1021-2014.

Molod, A. (2002), A global assessment of the mosaic approach to modeling land surface heterogeneity, *Journal of Geophysical Research*, *107*(D14), doi:10.1029/2001jd000588.

Myneni, R. B., et al. (2002), Global products of vegetation leaf area and fraction absorbed PAR from year one of MODIS data, *Remote Sensing of Environment, 83*, 214-231.

Oleson, K. W., et al. (2013), Technical Description of version 4.5 of the Community Land Model (CLM)*Rep.*, National Center for Atmospheric Research.

Pielke, R. A., R. Avissar, M. Raupach, A. J. Dolman, X. Zeng, and A. S. Denning (1998), Interactions between the atmosphere and terrestrial ecosystems: influence on weather and climate, *Global Change Biology*, *4*, 461-475.

Pielke, R. A., et al. (2011), Land use/land cover changes and climate: modeling analysis and observational evidence, *Wiley Interdisciplinary Reviews: Climate Change*, *2*(6), 828-850, doi:10.1002/wcc.144.

Pitman, A. J., et al. (2009), Uncertainties in climate responses to past land cover change: First results from the LUCID intercomparison study, *Geophysical Research Letters*, *36*(14), doi:10.1029/2009gl039076.

Subin, Z. M., L. N. Murphy, F. Li, C. Bonfils, and W. J. Riley (2012), Boreal lakes moderate seasonal and diurnal temperature variation and perturb atmospheric circulation: analyses in the Community Earth System Model 1 (CESM1), *Tellus A*, *64*(0), doi:10.3402/tellusa.v64i0.15639.

Swenson, S. C., and D. M. Lawrence (2014), Assessing a dry surface layer-based soil resistance parameterization for the Community Land Model using GRACE and FLUXNET-MTE data, *Journal of Geophysical Research: Atmospheres*, *119*(17), 10,299-210,312, doi:10.1002/2014jd022314.

Viovy, N. (2011), http://dods.extra.cea.fr/store/p529viov/cruncep/V4_1901_2012/, edited.

von Randow, C., et al. (2004), Comparative measurements and seasonal variations in energy and carbon exchange over forest and pasture in South West Amazonia, *Theoretical and Applied Climatology*, *78*(1-3), doi:10.1007/s00704-004-0041-z.

Zeng, X. (2001), Global Vegetation Root Distribution for Land Modeling, *Journal of Hydrometeorology*, *2*, 525-530.

Zhang, M., et al. (2014), Response of surface air temperature to small-scale land clearing across latitudes, *Environmental Research Letters*, *9*(3), 034002, doi:10.1088/1748-9326/9/3/034002.

Zhao, L., X. Lee, R. B. Smith, and K. Oleson (2014), Strong contributions of local background climate to urban heat islands, *Nature*, *511*(7508), 216-219, doi:10.1038/nature13462.

Chapter 4: Using sub-grid land model output to evaluate the simulated effects of land cover change on local climate

Manuscript in preparation as: Schultz, N.M. et al., Using sub-grid land model output to evaluate the simulated effects of land cover change on local climate.

Abstract

Land models produce a large amount of sub-grid information, and this data is particularly well suited to evaluate the representation of the effects of land use/land cover change (LULCC) on local climate. In this study, we use sub-grid output from the Community Land Model (CLM4.5) to calculate the difference in surface temperature (ΔT_S) and other surface energy budget variables between grass and forest plant functional types (PFTs). We use global satellite observations to evaluate the sub-grid differences in surface climate variables, and examine if the accuracy of the representation of ΔT_S is related to the representation of T_S for grass and tree PFTs. Our analysis focuses on day and nighttime separately. We find that although modeled T_S and other surface climate variables for each of the PFT classes are in good agreement with observations, this does not translate to good agreement in the differences between the PFTs (e.g. ΔT_S). Our results show that the biases in daily-mean ΔT_S are small (< 0.7 K), but are due to the offsetting of errors in the day and nighttime results. In evaluating land surface models' representation of LULCC, our results highlight the importance of using the differences in surface climate variables (e.g. ΔT_S), rather than just the output of individual land cover types.

Introduction

It has been well established that the biophysical effects of land use and land cover change (LULCC) affect local to regional climates. Observational and modeling studies agree that deforestation leads to cooling in high latitudes and warming in the tropics, with some uncertainties about the sign of the change in temperature in the mid-latitudes [e.g. *Bonan*, 2008; *Davin and de Noblet-Ducoudré*, 2010; *Lee et al.*, 2011; *Li et al.*, 2015; *Mahmood et al.*, 2010; *Pielke et al.*, 2011]. Regional changes in climate caused by deforestation can be larger than the changes resulting from increases in greenhouse gas emissions [*de Noblet-Ducoudré et al.*, 2012]. However, substantial disagreement among models exists when it comes to the regional climate response to LULCC [*Pitman et al.*, 2009]. In particular, *de Noblet-Ducoudré et al.* [2012] found that there was no consistency among land surface models in their representation of the partitioning of available energy between latent and sensible heat fluxes due to LULCC, highlighting the need for rigorous evaluation of land surface models. To that end, the goal of the Land Use Model Inter-comparison Project is to develop metrics and diagnostic protocols to quantify model performance when it comes to the simulated response of LULCC [*D M Lawrence et al.*, 2016].

Often, land surface models are evaluated using single-point mode simulations for different land cover types [*Bonan et al.*, 2014; *M Chen et al.*, 2015]. Using this framework, a single point (or grid cell) is driven by local atmospheric conditions, and the response of the model is compared to observations (usually from a flux tower). *Vanden Broucke et al.* [2015] argue that this method of evaluation may not provide a complete picture of a model's ability to accurately represent the effects of LULCC. Implicit in this type of model evaluation is that if the model acceptably simulates the surface climatology of two land cover types separately, it should be able to simulate the climate response of the transition between the two land cover types. However, what may

seem like acceptable biases for individual land classes may become magnified when examining the change from one land cover type to another.

A paired-site approach has emerged to investigate the potential impacts of LULCC using in-situ or satellite observations [*Juang et al.*, 2007; *Lee et al.*, 2011; *Li et al.*, 2015; *N.M. Schultz et al.*, 2017; *Teuling et al.*, 2010]. Substituting space for time, this type of analysis compares the land surface response of different land cover types to the same atmospheric conditions. For example, two flux towers within close proximity of each other, or satellite-derived values of land surface climatology from different land cover types within a small geographic region.

In terms of model performance, flux tower site pairs have been used to evaluate the simulated effects of LULCC on surface temperature in Europe [*Vanden Broucke et al.*, 2015]. Their results highlight the importance of evaluating a land surface model's simulation of land cover change, rather than just the climatology of the different land cover types. However, the geographic distribution of paired flux towers suitable for this type of analysis is uneven, limiting the ability to investigate the effects of LULCC, and thus model evaluation, across diverse climatological regions.

On a larger scale, satellite-derived products can provide a global assessment of the effects of land cover change on surface temperature, albedo, and evapotranspiration (ET) [*Boisier et al.*, 2013; 2014; *Li et al.*, 2015; *N.M. Schultz et al.*, 2017]. In this study, we use global satellite observations to investigate the representation of LULCC on land surface temperature (T_S) in the Community Land Model (CLM4.5). Many terrestrial models, including CLM, represent land cover heterogeneity in a grid cell as a mosaic of sub-grid tiles; however, few studies have attempted to utilize the sub-grid data to assess the biophysical effects of LULCC [*Malyshev et al.*, 2015; *N. M. Schultz et al.*, 2016]. Sub-grid information from climate models can be a powerful tool for LULCC studies, allowing for the direct comparison of land surface response of different land

cover types to the same forcing from the same prescribed or modeled atmospheric conditions. Comparing data from different land cover tiles within a grid cell can be considered an analogous method to the space-for-time approach that has been conducted using satellite observations [*Li et al.*, 2015; *Peng et al.*, 2014; *N.M. Schultz et al.*, 2017; *Wickham et al.*, 2012].

Here, we use sub-grid data from CLM4.5 to evaluate the representation of LULCC on T_S and the surface energy budget. Specifically, the objectives of this research are to: (1) directly evaluate the difference in surface temperature (ΔT_S) between sub-grid land cover types, (2) examine whether the accuracy of the representation of ΔT_S is related to the representation of T_S of individual land cover types, (3) evaluate ΔT_S during daytime and nighttime, and (4) compare the representation of ΔT_S across diverse climate regimes. We use a modified version of CLM4.5, in which each sub-grid plant functional type (PFT) is assigned to an individual soil column, thus making each PFT independent from the others within the grid cell [*N. M. Schultz et al.*, 2016].

Methods

Observational data

The observational dataset is derived from global data products from the Moderate Resolution Imaging Spectrometer (MODIS) and the Modern Era Retrospective-Analysis for Research and Applications (MERRA) [*Rienecker et al.*, 2011]. The full details of the dataset are described in *N.M. Schultz et al.* [2017]. Briefly, the MODIS dataset is comprised of 0.5^o x 0.5^o grids, with the average T_S, *LE* and albedo (α) calculated for forests and open land pixels within each grid. Using the International Geosphere Biosphere Programme (IGBP) classification scheme from the MODIS land cover classification product (MCD12Q1) [*Friedl et al.*, 2010], our forest class includes pixels that are classified as the five IGBP forest classes, while our open land class includes savanna, grasslands, and cropland/natural vegetation mosaic. The MODIS white-sky albedo (MCD43B3) [*Schaaf et al.*, 2002] was used in combination with incident solar radiation data from MERRA to calculate the amount of solar radiation absorbed at the surface ($K_a = K\downarrow[1 -$

α]). Unlike the MODIS T_S product (MYD11A2) [*Wan*, 2008], which contains a day (~13:30) and nighttime (~01:30) measurement, approximating daily maximum and minimum temperatures, the K_a and *LE* (MOD16) [*Mu et al.*, 2011] products represent the daily average. All observational data products used in this evaluation (13:30 T_S, 01:30 T_S, mean T_S, *LE*, and K_a) were averaged to the same temporal scale (monthly) for the years 2003-2010.

Model description & experimental design

We evaluate a sub-grid method of representing land cover change using the Community Land Model (CLM4.5) [*D M Lawrence et al.*, 2011; *Oleson et al.*, 2013], the land component of the Community Earth System Model (CESM) [*Hurrell et al.*, 2013]. The sub-grid heterogeneity of CLM4.5 allows for the calculation of biophysical processes for each plant functional type (PFT). By default in CLM, all PFTs share a single soil column. We use a modified version, described in detail by *N. M. Schultz et al.* [2016], where each PFT is assigned its own soil column, each with independently evolving soil moisture and temperature profiles, as well as carbon/nitrogen fluxes/storage when the biogeochemistry model is active. In this modified configuration, each PFT is independent from the other PFTs within the grid cell, providing an opportunity to examine the differences in land surface response to the same atmospheric forcing.

For this study, CLM4.5 was run offline for present-day conditions using 2003-2010 CRUNCEP atmospheric forcing data [*Viovy*, 2011] at a horizontal resolution of 0.9° lat x 1.25° lon. As our focus here is on surface temperature and biophysical processes, this simulation was run without an active biogeochemistry model, with vegetation phenology instead prescribed by satellite observations [*P J Lawrence and Chase*, 2007; *Myneni et al.*, 2002]. The initial conditions for this simulation were generated by cycling through the 1991-2010 CRUNCEP dataset for 60 years, which is more than enough time for soil moisture and temperature to reach equilibrium [*N. M. Schultz et al.*, 2016]. PFT-level state and flux variables were archived at hourly intervals for the 2003-2010 model simulation period.

For direct correspondence with the observational dataset, the CLM4.5 data were regridded to 0.5º x 0.5º using bilinear interpolation. For further agreement with the MODIS clear-sky conditions, we excluded modeled data where the clearness index [*Gu et al.*, 1999] was less than 0.5 [*Zhao et al.*, 2014]. For comparison with MODIS T_S, we only included the modeled T_S data at 1:00 and 13:00 local time each day. Modeled T_S was derived from longwave radiation components,

$$T_S = \left[\frac{L_\uparrow - (1 - \varepsilon)\, L_\downarrow}{\varepsilon\sigma}\right]^{(1/4)} \quad (1)$$

where $L_\uparrow$ and $L_\downarrow$ are the upward and downward longwave radiation fluxes, ε is the surface emissivity (assumed here to be 0.98), and σ is the Stefan-Boltzmann constant (5.67×10^{-8} W m^{-2} K^{-4}). We area-weighted the grass and tree PFT data within each grid cell into a single value for each of those respective land cover categories. Finally, the modeled data was averaged to the same temporal resolution as the MODIS/MERRA data, and was masked using the spatial coverage of the observational data.

Evaluation of model performance

As we are interested in evaluating CLM's representation of the effects of land cover change, our analysis focuses primarily on the sub-grid differences in surface climate variables between land cover types, rather than the absolute values of each land cover type themselves. Therefore, for each climate variable (13:30 T_S, 01:30 T_S, mean T_S, *LE*, and K_a) from observations and CLM, we calculate the difference (Δ) as open – forest, which can be thought of as the change resulting from deforestation. Because the localized surface temperature response to deforestation exhibits spatial variability, we evaluate model performance separately for four major climate zones defined by the Köppen-Geiger climate classification system [*Peel et al.*, 2007]: tropical (A), arid/semi-arid (B), temperate (C), and continental (D).

We quantify model performance over annual and seasonal scales using conventional measures of model-observation statistics: mean bias (*MB*), spatial correlation (*r*), standard deviation (σ), and centered root mean squared error (*E'*). Given observational values (*o*) and corresponding model results (*m*), these error metrics are defined as:

$$MB = \overline{m} - \overline{o} \tag{2}$$

$$r = \frac{1}{N}\frac{\sum_{n=1}^{N}(m_n - \overline{m})(o_n - \overline{o})}{\sigma_o \sigma_m} \tag{3}$$

$$\sigma^2 = \frac{1}{N}\sum_{n=1}^{N}(x_n - \overline{x})^2 \tag{3}$$

$$E'^2 = \frac{1}{N}\sum_{n=1}^{N}[(m_n - \overline{m})(o_n - \overline{o})]^2 \tag{4}$$

where the overbar denotes the mean of the set and the prime denotes the perturbation from the mean. In equation 3, *x* represents either observational or modeled data. These statistics can be represented in the two-dimensional space of the Taylor diagram [*Taylor*, 2001] simultaneously. Normalizing *E'* and σ_m by σ_o makes it possible to plot statistics for different fields on the same diagram.

Results

Model evaluation

The modeled daily mean ΔT_S (average of 13:00 and 1:00) is in general agreement with MODIS (Figure 4.1a-c). Averaged over the 8-year analysis period, the annual mean bias (MB) is less than ±1 K within each climate zone (Figure 4.2). With only two exceptions, this agreement is maintained across the seasons in each of the four climate zones. However, the agreement in the daily mean ΔT_S between CLM and MODIS appears to result from systematic biases in the modeled hourly data. Consistent across all four climate zones, daytime (13:30) ΔT_S is

underestimated and nighttime (1:30) ΔT_S is overestimated (Figure 4.1d-i, Figure 4.2). The largest hourly biases are observed in the continental and semi-arid regions (Figure 4.2a, c), where the annual daytime (nighttime) biases are -2.4K (1.1 K) and -3.8K (2.3 K). The daytime bias exhibits some seasonality in the continental and semi-arid zones, with the most extreme biases occurring during DJF and MAM in the continental zone, and during MAM and JJA in the semi-arid zone. In the temperate and tropical regions, there is little seasonality to the bias in ΔT_S (Figure 4.2b, d).

Examining the MB of each of the land cover classes individually provides additional information about the source of the biases in ΔT_S. While the departure of modeled T_S from observations may be partially due to uncertainties in the atmospheric forcing dataset, the fact that both of the sub-grid land cover classes are forced by the same data allows us to compare their relative biases. Generally, the daytime T_S biases for forest PFTs are larger than those for grass PFTs (Figures S4.1-S4.2), which is why the modeled daytime ΔT_S is underestimated. In the semi-arid zone, for example, the forest daytime T_S is overestimated by 4.6 K, while the bias for grass PFTs is only 1.0 K.

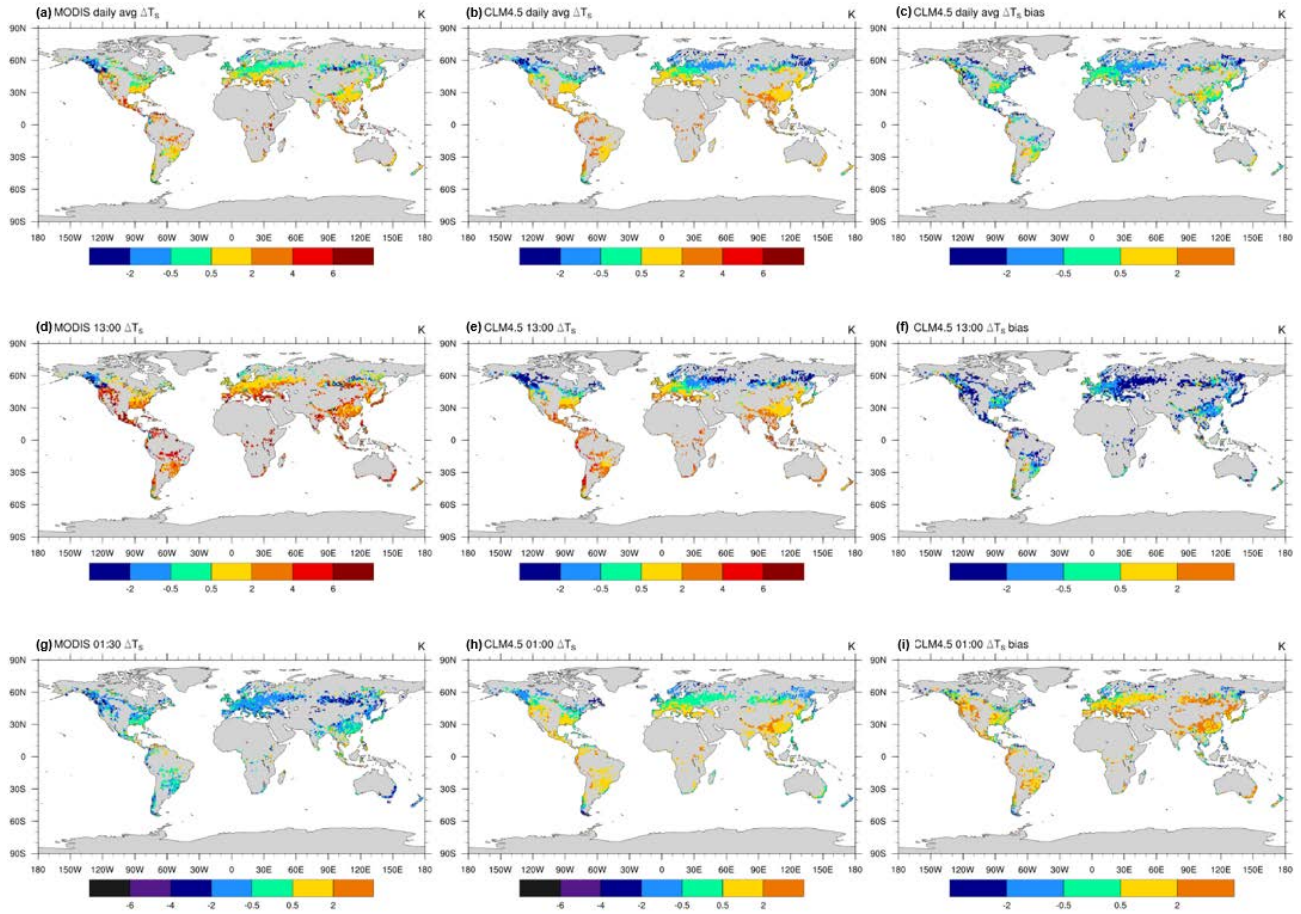

Figure 4.1. The (a-c) daily mean, (d-f) daytime (13:30 or 13:00), and (g-i) nighttime (1:30 or 1:00) ΔT_S. The ΔT_S is shown for MODIS (a, d, g), and CLM4.5 (b, e, h). The CLM ΔT_S bias is shown in panels c, f, i. All data are averaged over 2003-2010. The bias is calculated here as CLM4.5 ΔT_S – MODIS ΔT_S.

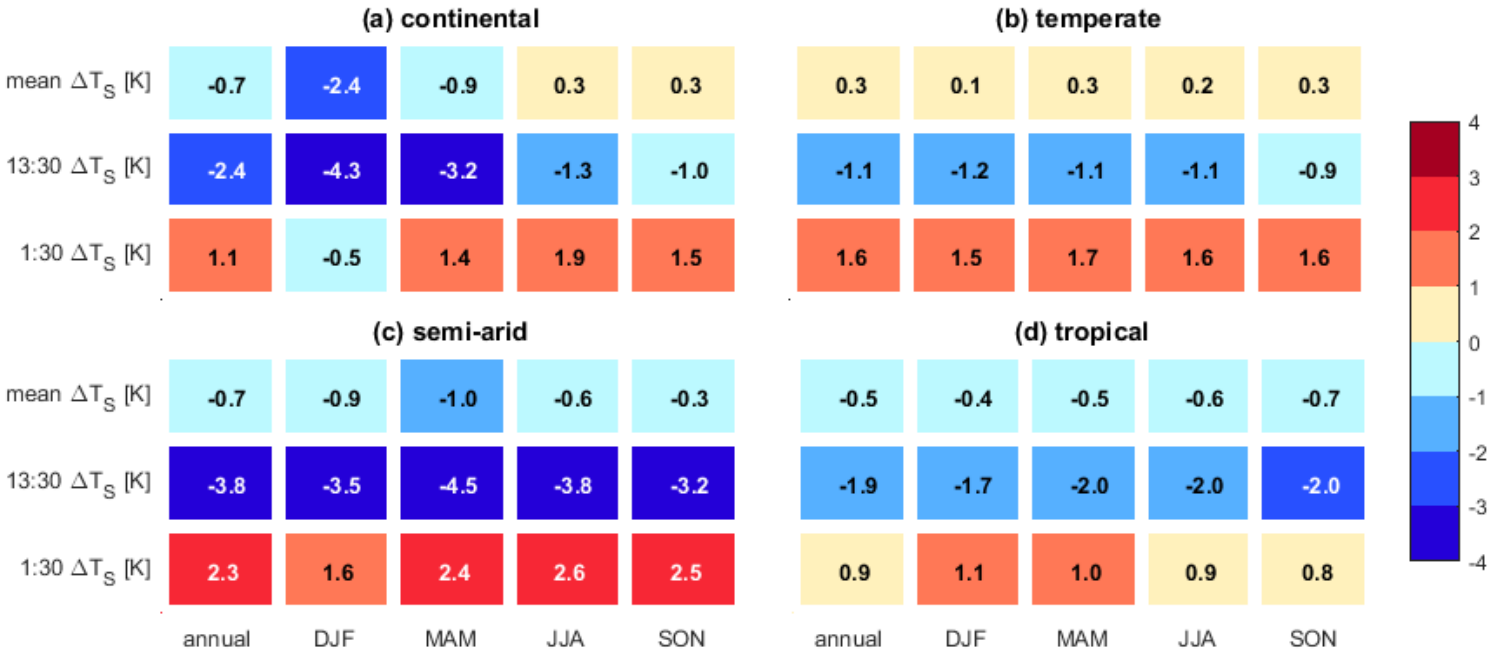

Figure 4.2. The 8-year mean bias in the daily mean, daytime (13:30), and nighttime (01:30) ΔT_S for the (a) continental, (b) temperate, (c) semi-arid, and (d) tropical climate zones.

The ΔK_a is underestimated across all four climate zones, with the most significant biases observed in the continental zone (Figure 4.3a-c, Figure 4.4a). Here, the annual ΔK_a is biased by -14.9 W m^{-2}, with the largest departure from observations occurring during MAM (-28.6 W m^{-2}). In other words, the observational data show the sub-grid difference in K_a to be -21.4 W m^{-2}, while the model produces a sub-grid difference of -50.0 W m^{-2}. In the continental zone, the MB in ΔK_a results from biases in both PFT classes. During MAM, K_a is overestimated for forest PFTs by 11 W m^{-2}, while at the same time is underestimated by 18 W m^{-2} for grass PFTs (Figures S4.3a, S4.4a). Across the other climate zones, the annual bias in ΔK_a is small (less than 5 W m^{-2}). Here, the departure in K_a from observations for forest and grass PFTs are of approximately the same magnitude.

The most significant biases in ΔLE occur in the tropical zone (Figure 4.3d-f, Figure 4.4b). In this region, the annual bias in ΔLE is 43.3 W m^{-2}, and is persistent across all seasons. These large biases in ΔLE result from the fact that MODIS data show that the *LE* of non-forested areas is 39 W m^{-2} lower than tropical forests, while the modeled results show that grass PFTs have a higher *LE* by 4.3 W m^{-2}. The bias in ΔLE results from the compounding of errors in both forest and grass PFT classes. In the tropical zone, the annual *LE* of forest PFTs is underestimated by 16.4 W m^{-2}, while the *LE* of grass PFTs is overestimated by 26.6 Wm^{-2}. Across the other climate zones, the *LE* of forest PFTs is consistently underestimated while the *LE* of grass PFTs is overestimated. However, moving away from the tropics, the forest and grass biases in *LE* are smaller, making the additive effect of errors in the individual land cover classes on ΔLE less significant.

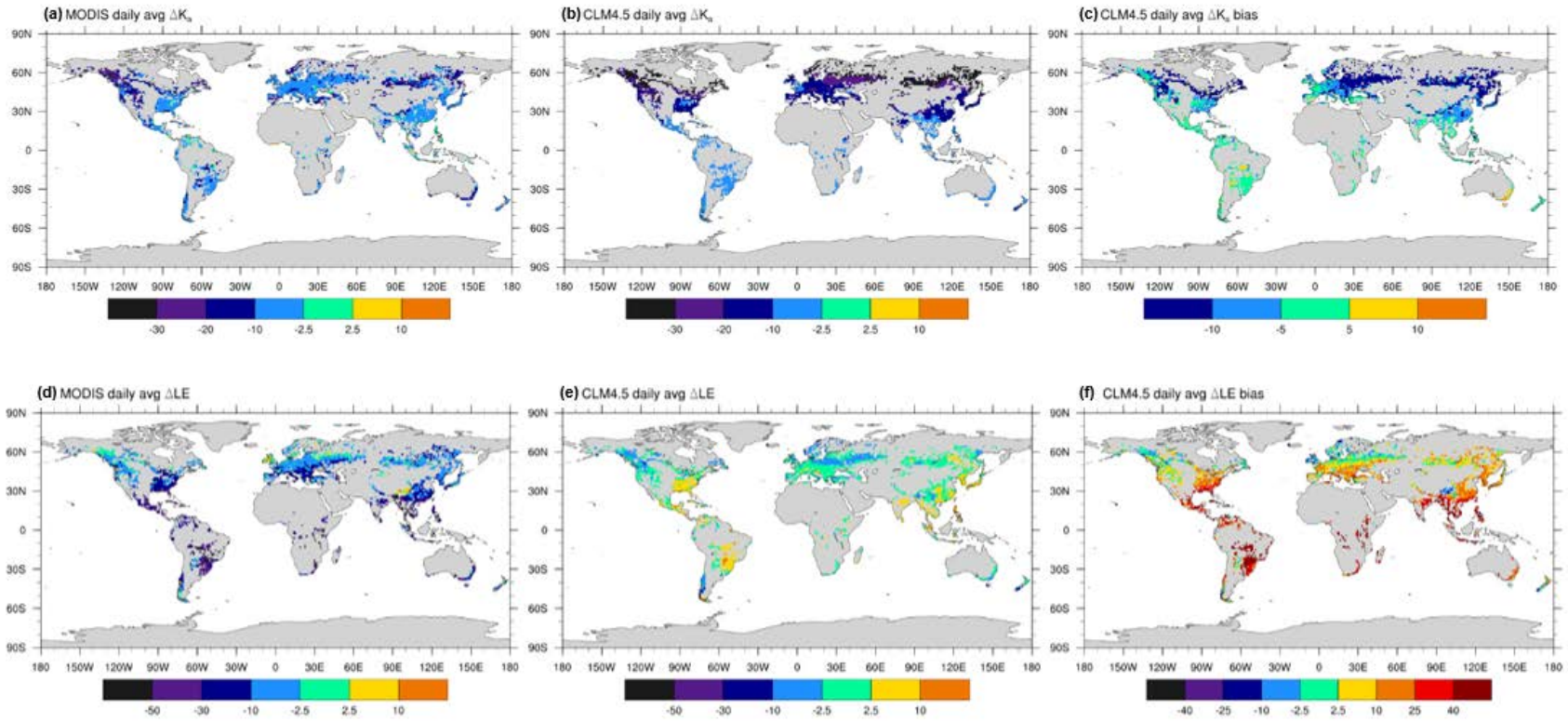

Figure 4.3. The (a) MODIS ΔK_a, (b) CLM4.5 ΔK_a, and (c) CLM4.5 ΔK_a bias (CLM-MODIS), and (d) MODIS ΔLE, (e) CLM4.5 ΔLE, and (f) CLM4.5 ΔLE bias, averaged over 2003-2010.

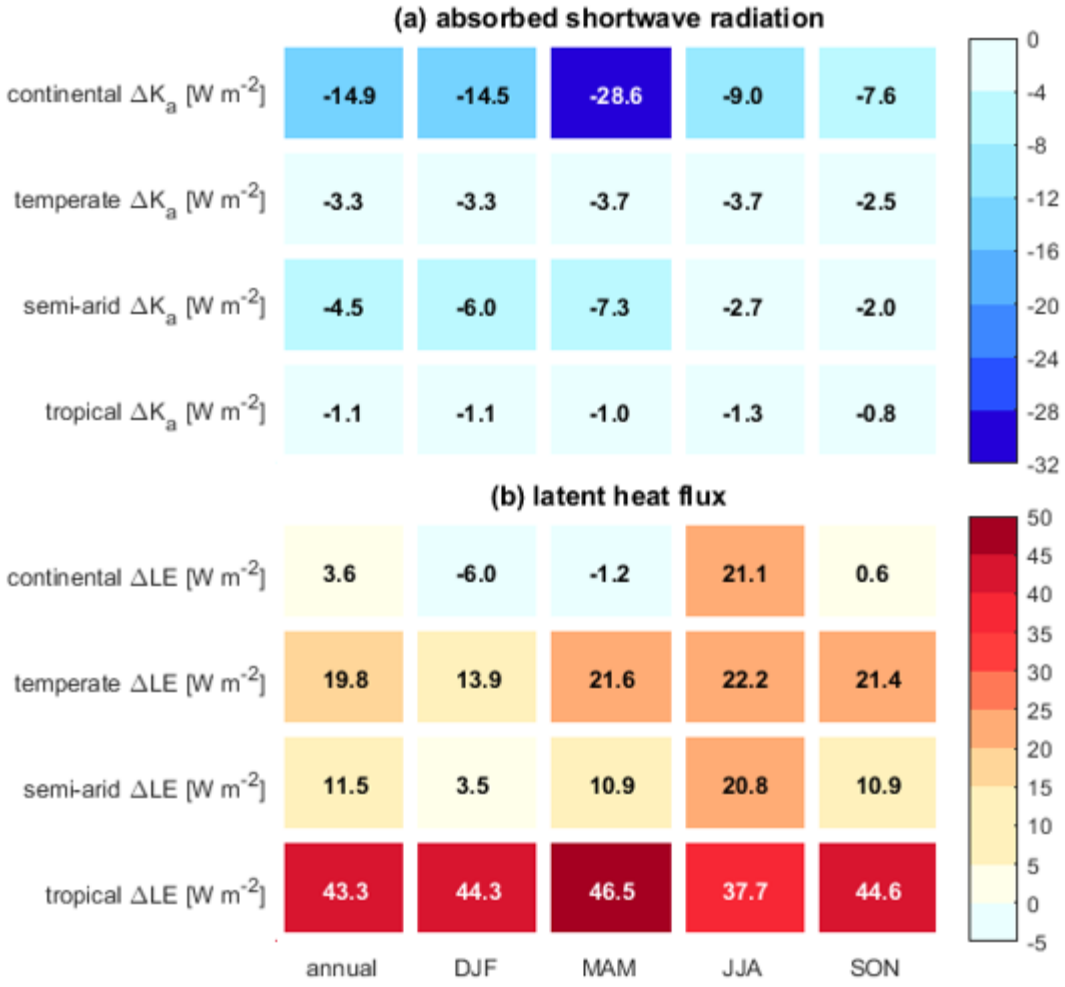

Figure 4.4. The 8-year mean bias in (a) ΔK_a and (b) ΔLE for each of the four climate zones.

Taylor diagrams illustrate the effects of modeled biases in T_S from individual PFT classes on ΔT_S (Figure 4.5). The angular dimension displays the pattern correlation of the modeled and observed data, while the radial dimension shows the normalized standard deviation (ratio of the standard deviation of simulated and observed fields). The standard deviation of the observed field is also normalized by itself. In other words, a standard deviation >1 indicates more variability in the modeled data than the observed values, and vice versa for standard deviations < 1. Were the model to agree perfectly with observations, markers on the graph would lie on the point OBS (E' = 0, r = 1, $\sigma_m = \sigma_o$). The statistics for the Taylor diagrams were computed using the 2003-2010 monthly climatology from MODIS and CLM, shown annually and seasonally for each of the four climate zones.

For the daily mean, daytime (13:30), and nighttime (1:30) T_S and ΔT_S, it is evident that the relative agreement between modeled and observed T_S does not necessarily translate to good agreement in ΔT_S (Figure 4.5a-c). For the daily mean values (Figure 4.5a), the pattern correlations of grass and forest T_S are greater than 0.95 with similar variability to observations (~1) for the continental, temperate, and semi-arid climate zones. The agreement is slightly reduced for the tropical zone, where the correlations are approximately 0.75 with slightly lower standard deviations than the MODIS data. However, when it comes to ΔT_S, the strongest correlation between simulated and observed values is 0.6, and is as low as 0.1. With a few exceptions, modeled ΔT_S across climate zones and seasons is less variable than what is observed with MODIS. The daytime values (Figure 4.5b) show similar patterns to the daily means. Again, although simulated daytime T_S is strongly correlated to and shows similar variability with observations, the statistics for ΔT_S are significantly worse, with pattern correlations ranging from 0.1 to 0.61, and normalized standard deviations ranging from 0.27 to 1.25. Although the agreement between the modeled and observed nighttime T_S (Figure 4.5c) is only slightly reduced compared to the mean or daytime values (r = 0.71-0.97, σ_m/σ_o = 0.8-1.2), the correspondence between modeled and observed ΔT_S is

significantly diminished. Model simulated results can only be plotted in the first quadrant of the Taylor diagram, as shown here, if the spatial correlation coefficient is positive. To aid visual comparison with daily mean and daytime ΔT_S (Figure 4.5a-b), negative correlations between the modeled and observed values in nighttime ΔT_S (Figure 4.5c) are plotted at $r = 0$ (on the vertical axis). The modeled nighttime ΔT_S is negatively correlated with observed values for 6 of the 20 temporal-geographic regions considered here (r ranging from -0.18 to -0.10). The semi-arid DJF ΔT_S in the semi-arid zone has the highest pattern correlation (0.3). The normalized standard deviations of the modeled nighttime ΔT_S values exhibit similar patterns to the daily mean and daytime values, ranging from 0.5 to 1.49.

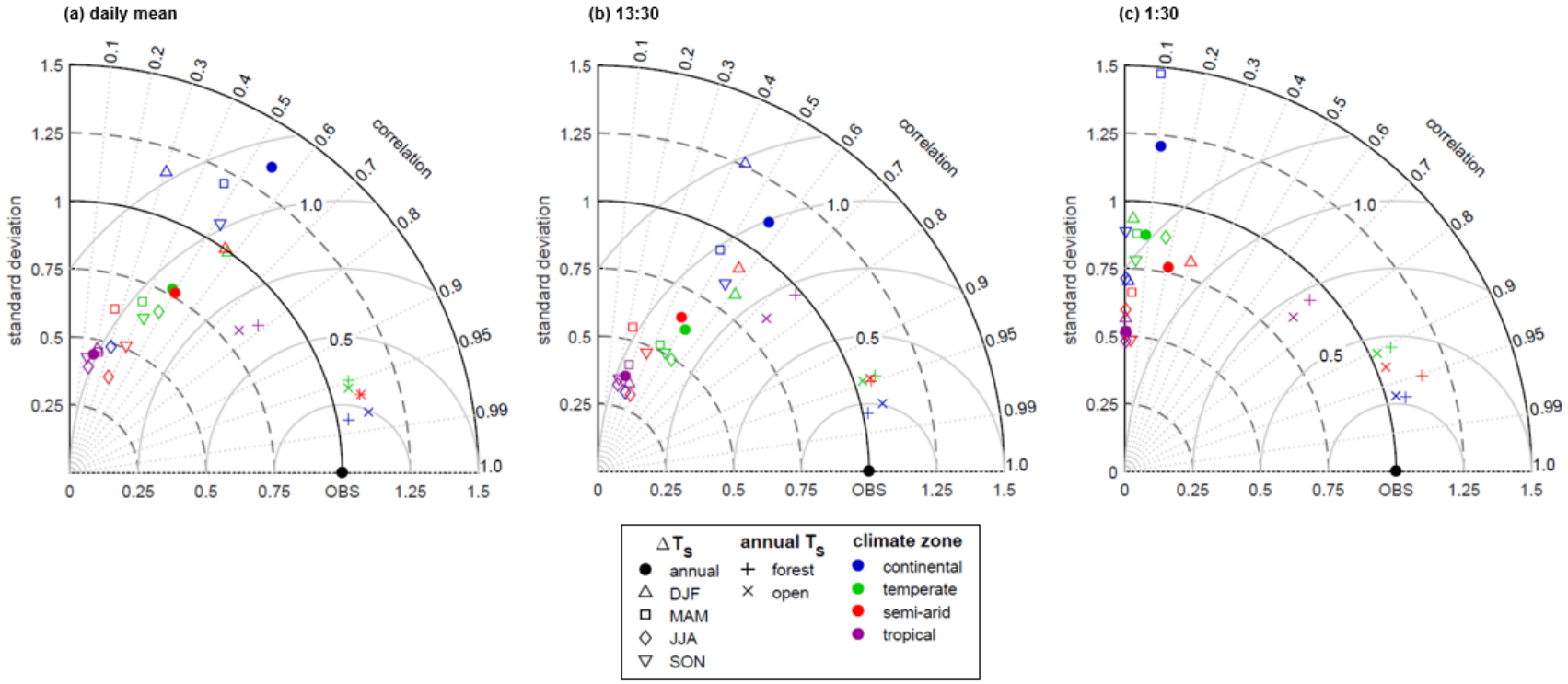

Figure 4.5. Taylor diagrams for (a) daily mean, (b) daytime (13:30) and (c) nighttime (1:30) T_S and ΔT_S.

We also use Taylor diagrams to examine the statistical relationships of absorbed shortwave radiation (K_a and ΔK_a) and the latent heat flux (*LE* and ΔLE) (Figure 4.6). The pattern correlation of K_a for forest and grass and tree PFTs ranges from 0.94 to 0.98 for the continental, temperate, and semi-arid regions, and in these regions, the model exhibits similar variability in K_a to what is observations (Figure 4.6a). The modeled K_a for the tropical regions is less variable than observed values, which results in lower correlations (0.56-0.57) for tree and grass PFTs. The K_a biases for each of the PFT classes produce ΔK_a values that have weak to medium correlation with observations (0.09 to 0.71). The modeled ΔK_a have normalized standard deviations ranging from 0.4 to 1.66.

The spatial correlation of modeled *LE* (Figure 4.6b) for the tree and grass PFTs ranges from 0.51 to 0.94, with higher correlations in the continental and temperate regions. In general, the variability of annual *LE* for tree PFTs agrees well with observations ($\sigma_m/\sigma_o \sim 1$, except for semi-arid zone). In contrast, the spatial variability in *LE* for grass PFTs is larger than the observed values ($\sigma_m/\sigma_o \sim 1.5$, except for semi-arid zone). The model-derived ΔLE exhibits negative correlations with observations in 13 of the 20 time periods/regions examined here (r ranging from -0.36 to -0.03). Where there is a positive correlation in ΔLE, r ranges from 0.04 to 0.32, with the strongest correlation for the continental zone DJF. Overall, the modeled ΔLE exhibits less variability than observations (typical $\sigma_m/\sigma_o = 0.2 – 0.35$).

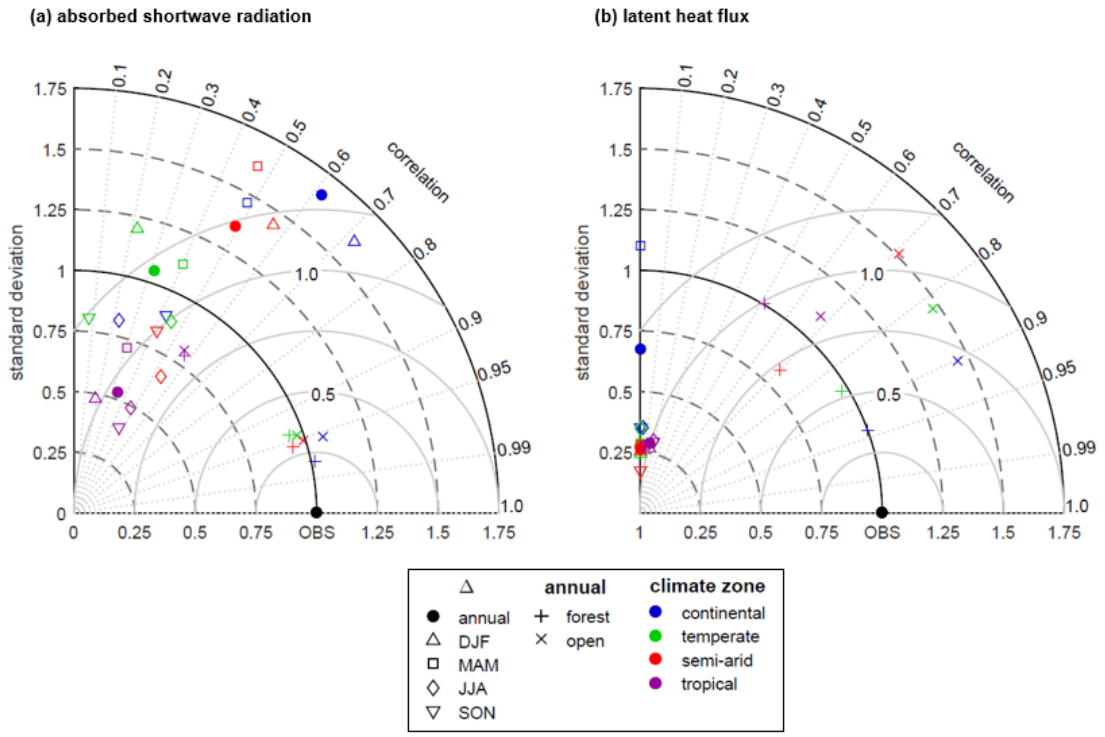

Figure 4.6. Taylor diagrams for (a) absorbed shortwave radiation and (b) the latent heat flux.

Discussion

Sub-grid LULCC difference

For the purposes of LULCC simulation, our results highlight the importance of evaluating land surface models using the differences in surface climate variables (e.g. ΔT_S), rather than relying solely on the representation of the individual land cover types (e.g. T_S). Our results show that although there was generally strong agreement between the modeled and observed values for tree and grass PFTs, this agreement did not translate to a strong agreement between the modeled and observed differences between the tree and grass PFTs. We found that the spatial correlation of modeled and observed T_S to be in the range of 0.7 to 0.98, while the correlation between modeled and observed ΔT_S was 0.6 at best, with negative correlations for nighttime ΔT_S. Over most regions and seasons analyzed here, CLM did a good job of capturing the spatial variability of T_S across each of the climate regions, but across most regions and seasons, CLM underestimated the spatial variations of ΔT_S. The worst agreement between modeled and observed T_S was in the tropical region. For absorbed shortwave radiation, CLM shows good performance for each of the grass and tree PFTs, but again did not result in overall good agreement between modeled and observed ΔK_a. Of the surface climate variables considered here, CLM was the least successful in modeling LE and ΔLE. Compared to T_S and K_a, the correlations between modeled and observed LE were lower across all regions and seasons, ranging from 0.5 to 0.93. These biases resulted in poor agreement between modeled and observed ΔLE. In fact, in most cases, there was a negative correlation between modeled and observed ΔLE.

Biases in the grass or tree PFT T_S may be attributed to deviations of the forcing data used in this simulation with observed meteorology. However, it does not necessarily follow that biases in the difference in surface climate variables between the two PFT classes can be contributed to the same reason. Therefore, for the purposes of testing land surface models of their representation of LULCC, evaluating the sub-grid difference provides a new, valuable source of information about

model performance. In terms of model development, perhaps it would be useful to take into account the differences between the different sub-grid tiles when testing new model schemes or parameterizations to ensure an accurate representation of each individual sub-grid tile or PFT.

Day and night evaluation

Although observations have shown a diurnal asymmetry in the surface temperature response to LULCC (deforestation) [*Lee et al.*, 2011; *Li et al.*, 2015; *N.M. Schultz et al.*, 2017; *Zhang et al.*, 2014], studies that evaluate the impact of LULCC in climate models rarely distinguish between day and nighttime climate [*Vanden Broucke et al.*, 2015]. Instead, the analyses are averaged over daily or longer timescales. Our results show that limiting the analysis to the daily mean obscures important information about sub-daily model performance. We found that on an annual basis, the daily mean ΔT_S across each of the four climate regions was simulated to within 0.7 K of the observed values. However, the daytime ΔT_S was overestimated by 0.8 to 2.6 K, and the nighttime ΔT_S was underestimated by 1.1 to 3.8 K. Therefore, the relative agreement of the modeled and observed daily mean ΔT_S is due to the offset of the errors in the hourly data. Using flux tower site pairs in Europe, *Vanden Broucke et al.* [2015] report a similar diurnal bias in modeled CLM ΔT_S. From their analysis, the daytime ΔT_S is underestimated by up to 3 K, while the nighttime ΔT_S is overestimated by 3 to 6 K. In their study region, this resulted in a daily mean ΔT_S that was biased high by approximately 2 K. Their analysis attributes the lack of nighttime cooling to the inability of COSMO-CLM^2 to capture the observed reduction in incident longwave radiation ($L\downarrow$), and hypothesize that the reduction in $L\downarrow$ over open lands may be due to: (1) an aerosol effect from forest VOC emissions, (2) decreased boundary layer humidity, and/or (3) increased boundary layer stability. Overall, our day and nighttime results highlight the importance of evaluating the effects on LULCC separately for day and night. Averaging to daily or longer timescales may not accurately represent the reality of the model's performance.

Diagnosing sources of error

This paper joins several recent studies seeking to evaluate and diagnose simulated changes to surface temperature and the surface energy budget in response to local land cover change in CLM. Our results are in agreement with *Chen et al, in review* [2017] who, using a paired FLUXNET site approach, found issues in CLM's ability to partition energy between *LE* and *H*, and like this study, found a slight increase in *LE* after deforestation, contrary to observations. By further investigating the three components of evapotranspiration (ground evaporation, canopy evaporation, and transpiration) in CLM4.5, they attribute a source of the *LE* bias to the soil resistance parameterization in CLM4.5, leading to the overestimation of ground evaporation over the open land (non-forested). Previous studies also have noted the excessive ground evaporation over sparse canopies in CLM4.5; however, *Swenson and Lawrence* [2014] have implemented a dry surface layer for the soil resistance parameterization to solve this issue for the new version of CLM (CLM5). Furthermore, *Meier et al, in prep* [2017] use the sub-grid configuration of *Schultz et al.* [2016] to show that four aspects of the parameterizations of vegetation transpiration (root distribution, soil moisture stress, light limitation, and the maximum rate of carboxylation) may help alleviate some of the biases in the simulation of *ET* in CLM4.5. Further evaluation of these processes should be undertaken with the upcoming CLM5.

Biophysical metrics such like the intrinsic biophysical partitioning method (IBPM) [*Lee et al., 2011*] or the decomposed temperature metric (DTM) [*Juang et al.*, 2007] can be important tools in diagnosing the impacts of LULCC in global climate model simulations, providing a measure by which to validate climate model performance [*L Chen and Dirmeyer*, 2016; *Vanden Broucke et al.*, 2015], and diagnosing the sensitivity of land surface models to LULCC for the upcoming Land-Use Model Inter-comparison Project [*D M Lawrence et al.*, 2016]. These metrics may also be used to contrast how different land cover types respond to a changing climate, including extreme events such as heat waves or droughts.

Conclusions

In this paper, we used sub-grid data from CLM4.5 to evaluate the representation of LULCC on T_S and the surface energy budget. We directly examined how the model simulated the difference in surface temperature (ΔT_S) between sub-grid land cover types, and examined if the accuracy of the representation of T_S for each sub-grid land cover type was related to the representation of ΔT_S. Further, our analysis focused on both day and nighttime surface temperature, and compared the representation of ΔT_S across different climate zones.

We found that although there was generally strong agreement between the modeled and observed values for tree and grass PFTs, it did not translate to strong agreement between the modeled and observed differences between the grass and tree PFTs. Instead, the small biases at the PFT-level were compounded into larger errors when the difference between them was calculated. Additionally, our results show that for a full understanding of model performance, it is important to evaluate the model at sub-daily scales. The modeled daily mean ΔT_S was in relative agreement with observations, but was due to the offset of errors in the hourly data, with the daytime ΔT_S systematically underestimated and nighttime ΔT_S overestimated.

Land models such as CLM produce a great deal of sub-grid information, but that data is rarely used for LULCC experiments or model evaluation. Here, we highlight the utility of sub-grid data for model evaluation using a space-for-time method. For the purposes of LULCC, our results demonstrate the importance of evaluating land surface models using the differences in surface climate variables (e.g. ΔT_S), rather than just the representation of individual land cover types. Further, we show that evaluation of the daily mean may not accurately depict the full reality of model performance, and it is important to evaluate the model separately during day and night.

The modeling framework and performance metrics developed here can be used to evaluate future versions of CLM, and can be applied to other land surface models. Because land surface models,

including CLM, calculate surface processes at the PFT-level, model evaluation at this scale is able to identify potential biases at their source and therefore improve sub-grid and grid-averaged output.

Supplementary Figures

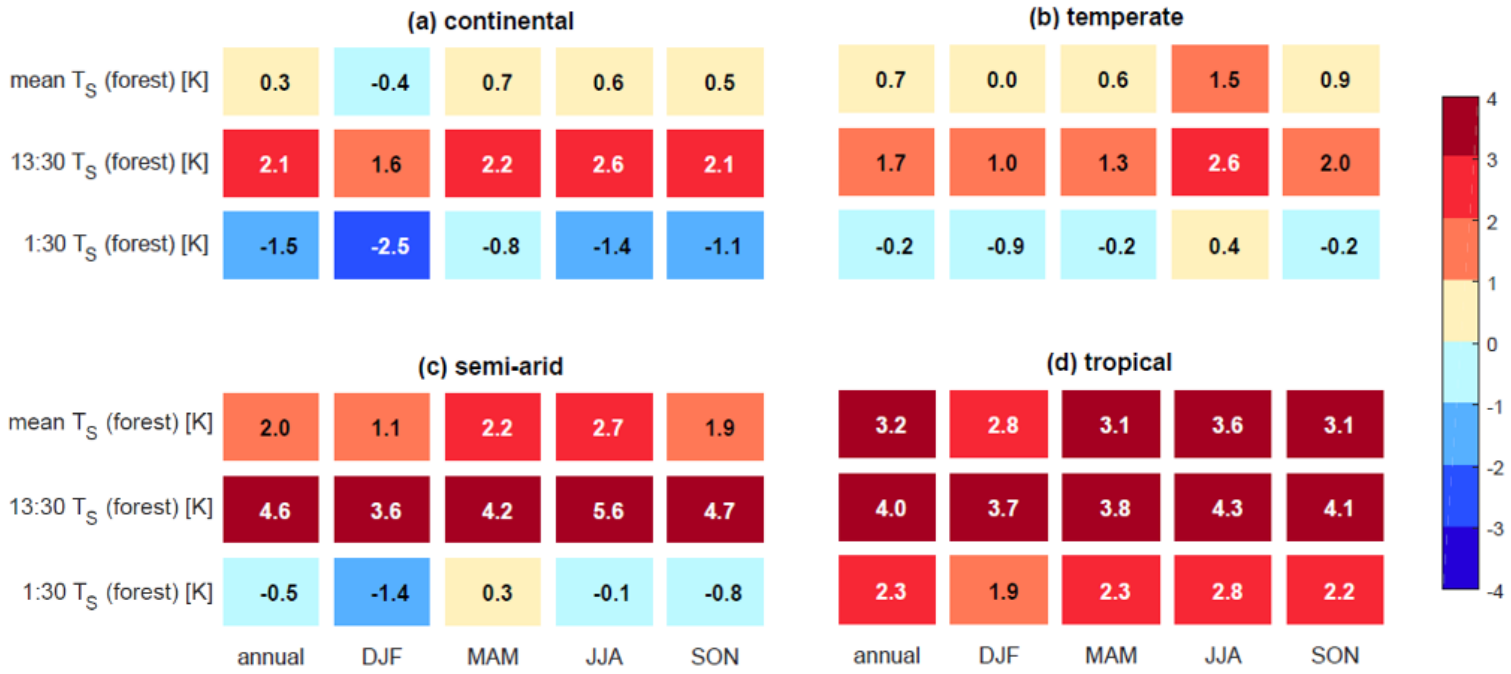

Figure S4.1. The 8-year mean bias in the daily mean, daytime (13:30), and nighttime (01:30) forest T_S for the (a) continental, (b) temperate, (c) semi-arid, and (d) tropical climate zones.

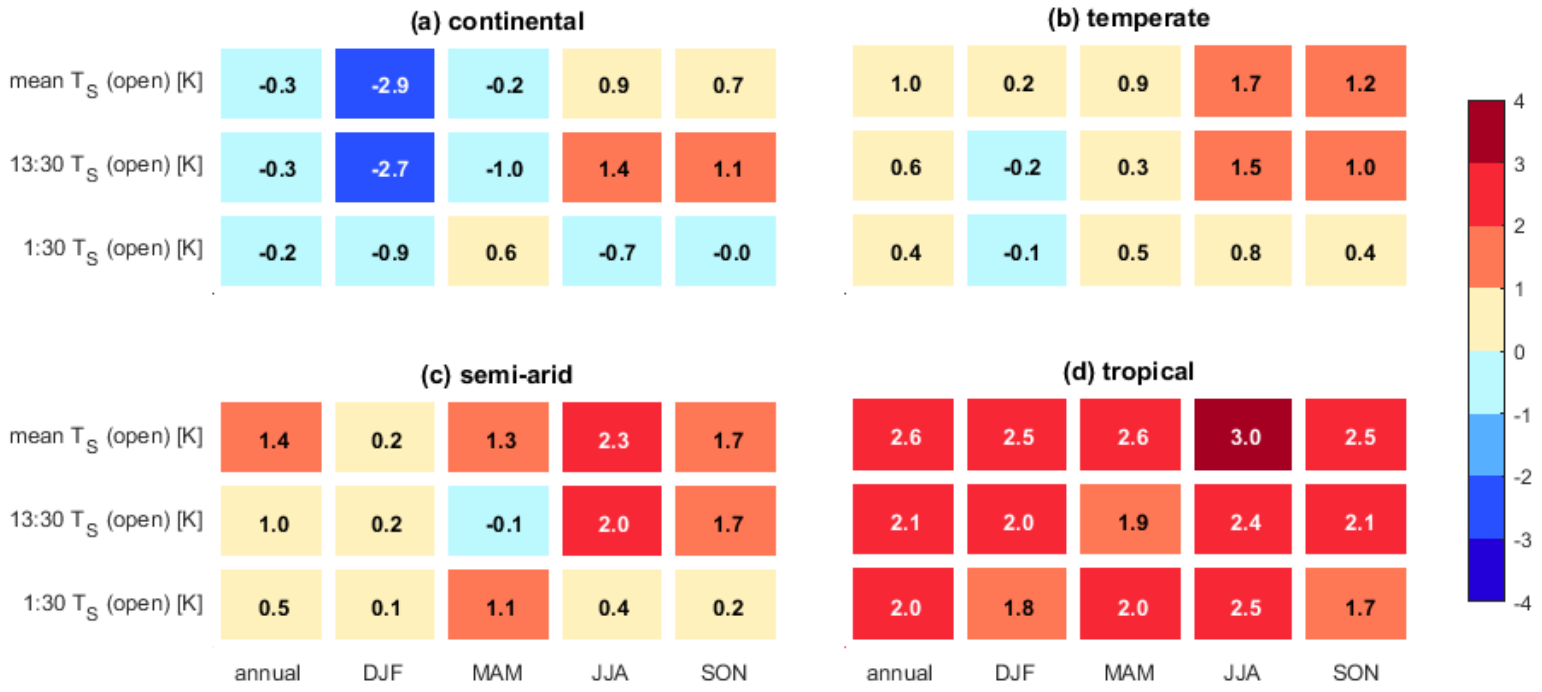

Figure S4.2. The 8-year mean bias in the daily mean, daytime (13:30), and nighttime (01:30) open land T_S for the (a) continental, (b) temperate, (c) semi-arid, and (d) tropical climate zone.

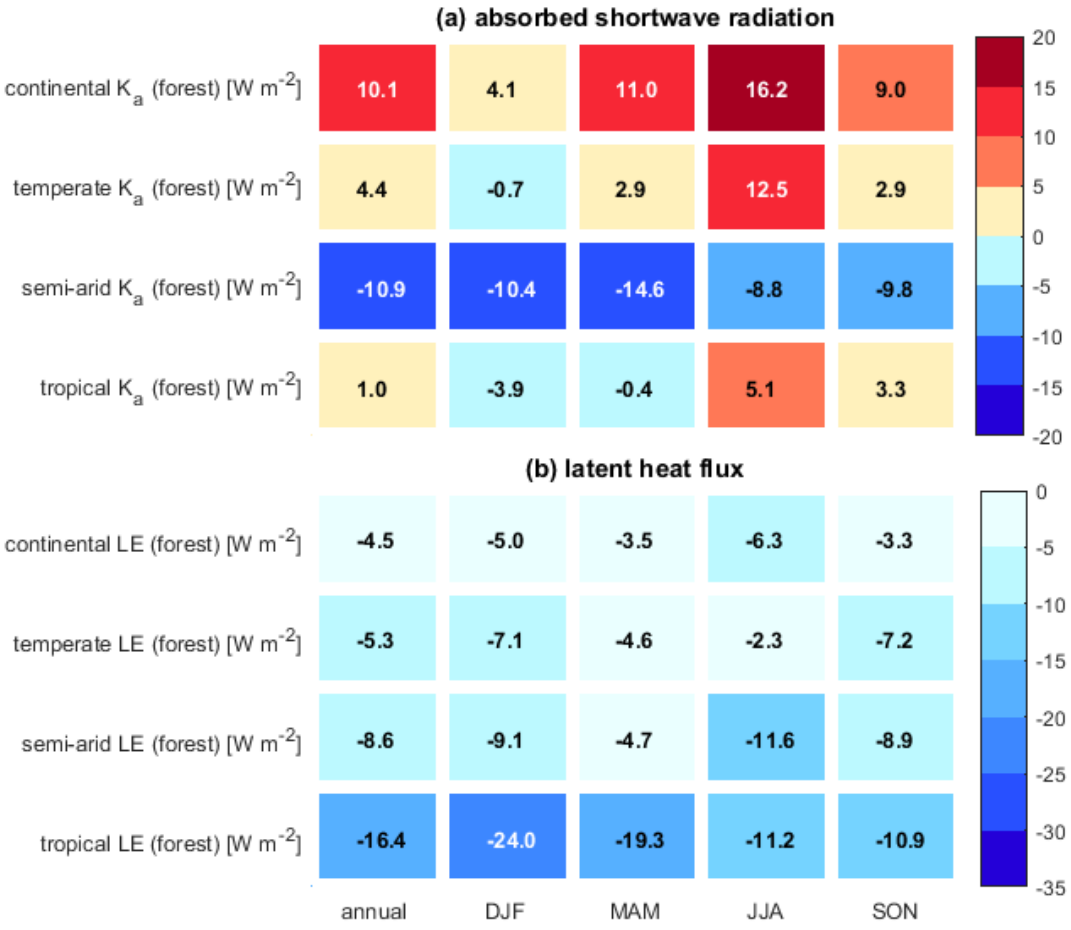

Figure S4.3. The 8-year mean bias in (a) forest K_a and (b) forest *LE* for each of the four climate zones.

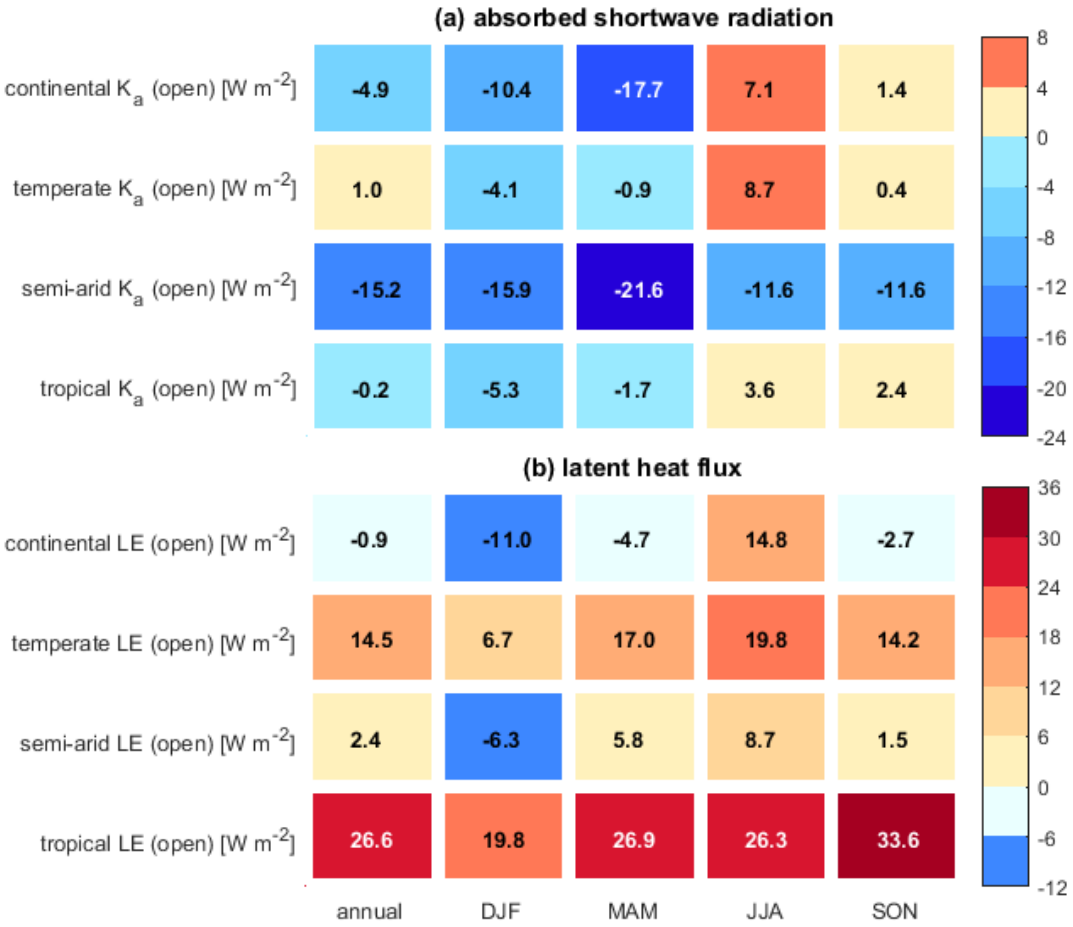

Figure S4.4. The 8-year mean bias in (a) open land K_a and (b) open land *LE* for each of the four climate zones.

References

Boisier, J. P., N. de Noblet-Ducoudré, and P. Ciais (2013), Inferring past land use-induced changes in surface albedo from satellite observations: a useful tool to evaluate model simulations, *Biogeosciences*, *10*(3), 1501-1516, doi:10.5194/bg-10-1501-2013.

Boisier, J. P., N. de Noblet-Ducoudré, and P. Ciais (2014), Historical land-use induced evapotranspiration changes estimated from present-day observations and reconstructed land-cover maps, *Hydrology and Earth System Sciences Discussions*, *11*(2), 2045-2089, doi:10.5194/hessd-11-2045-2014.

Bonan, G. B. (2008), Forests and climate change: forcings, feedbacks, and the climate benefits of forests, *Science*, *320*(5882), 1444-1449, doi:10.1126/science.1155121.

Bonan, G. B., M. Williams, R. A. Fisher, and K. W. Oleson (2014), Modeling stomatal conductance in the earth system: linking leaf water-use efficiency and water transport along the soil–plant–atmosphere continuum, *Geoscientific Model Development*, *7*(5), 2193-2222, doi:10.5194/gmd-7-2193-2014.

Chen, L., and P. A. Dirmeyer (2016), Adapting observationally based metrics of biogeophysical feedbacks from land cover/land use change to climate modeling, *Environmental Research Letters*, *11*(3), 034002, doi:10.1088/1748-9326/11/3/034002.

Chen L., P.A. Dirmeyer, Z. Guo, N.M. Schultz (2017), Pairing FLUXNET sites to validate model representations of land use/land cover change, *Hydrology and Earth System Science (in review).*

Chen, M., T. J. Griffis, J. M. Baker, J. D. Wood, and K. Xiao (2015), Simulating crop phenology in the Community Land Model and its impact on energy and carbon fluxes, *Journal of Geophysical Research: Biogeosciences*, *120*, 310-325, doi:10.1002/.

Davin, E. L., and N. de Noblet-Ducoudré (2010), Climatic Impact of Global-Scale Deforestation: Radiative versus Nonradiative Processes, *Journal of Climate*, *23*(1), 97-112, doi:10.1175/2009jcli3102.1.

de Noblet-Ducoudré, N., et al. (2012), Determining Robust Impacts of Land-Use-Induced Land Cover Changes on Surface Climate over North America and Eurasia: Results from the First Set of LUCID Experiments, *Journal of Climate*, *25*(9), 3261-3281, doi:10.1175/jcli-d-11-00338.1.

Friedl, M. A., D. Sulla-Menashe, B. Tan, A. Schneider, N. Ramankutty, A. Sibley, and X. Huang (2010), MODIS Collection 5 global land cover: Algorithm refinements and characterization of new datasets, *Remote Sensing of Environment*, *114*(1), 168-182, doi:10.1016/j.rse.2009.08.016.

Gu, L., J. D. Fuentes, H. H. Shugart, R. M. Staebler, and T. A. Black (1999), Responses of net ecosystem exchanges of carbon dioxide to changes in cloudiness: Results from two North American deciduous forests, *Journal of Geophysical Research: Atmospheres*, *104*(D24), 31421-31434, doi:10.1029/1999jd901068.

Hurrell, J. W., et al. (2013), The Community Earth System Model: A Framework for Collaborative Research, *Bulletin of the American Meteorological Society*, *94*(9), 1339-1360, doi:10.1175/bams-d-12-00121.1.

Juang, J.-Y., G. Katul, M. Siqueira, P. Stoy, and K. Novick (2007), Separating the effects of albedo from eco-physiological changes on surface temperature along a successional chronosequence in the southeastern United States, *Geophysical Research Letters*, *34*(21), doi:10.1029/2007gl031296.

Lawrence, D. M., et al. (2016), The Land Use Model Intercomparison Project (LUMIP) contribution to CMIP6: rationale and experimental design, *Geoscientific Model Development*, *9*(9), 2973-2998, doi:10.5194/gmd-9-2973-2016.

Lawrence, D. M., et al. (2011), Parameterization improvements and functional and structural advances in Version 4 of the Community Land Model, *Journal of Advances in Modeling Earth Systems*, *3*(3), doi:10.1029/2011ms000045.

Lawrence, P. J., and T. N. Chase (2007), Representing a new MODIS consistent land surface in the Community Land Model (CLM 3.0), *Journal of Geophysical Research*, *112*(G1), doi:10.1029/2006jg000168.

Lee, X., et al. (2011), Observed increase in local cooling effect of deforestation at higher latitudes, *Nature*, *479*(7373), 384-387, doi:10.1038/nature10588.

Li, Y., M. Zhao, S. Motesharrei, Q. Mu, E. Kalnay, and S. Li (2015), Local cooling and warming effects of forests based on satellite observations, *Nature communications*, *6*, 6603, doi:10.1038/ncomms7603.

Mahmood, R., et al. (2010), Impacts of Land Use/Land Cover Change on Climate and Future Research Priorities, *Bulletin of the American Meteorological Society*, *91*(1), 37-46, doi:10.1175/2009bams2769.1.

Malyshev, S., E. Shevliakova, R. J. Stouffer, and S. W. Pacala (2015), Contrasting Local versus Regional Effects of Land-Use-Change-Induced Heterogeneity on Historical Climate: Analysis with the GFDL Earth System Model, *Journal of Climate*, *28*(13), 5448-5469, doi:10.1175/jcli-d-14-00586.1.

Meier, R. et al (2017), Using observations to evaluate and improve the Community Land Model's sensitivity to deforestation, *Biogeosciences (in preparation).*

Mu, Q., M. Zhao, and S. W. Running (2011), Improvements to a MODIS global terrestrial evapotranspiration algorithm, *Remote Sensing of Environment*, *115*(8), 1781-1800, doi:10.1016/j.rse.2011.02.019.

Myneni, R. B., et al. (2002), Global products of vegetation leaf area and fraction absorbed PAR from year one of MODIS data, *Remote Sensing of Environment*, *83*, 214-231.

Oleson, K. W., et al. (2013), Technical Description of version 4.5 of the Community Land Model (CLM)*Rep.*, National Center for Atmospheric Research.

Peel, M. C., B. L. Finlayson, and T. A. McMahon (2007), Updated world map of the Koppen-Geiger climate classification, *Hydrology and Earth System Science*, *11*, 1633-1644.

Peng, S. S., S. Piao, Z. Zeng, P. Ciais, L. Zhou, L. Z. Li, R. B. Myneni, Y. Yin, and H. Zeng (2014), Afforestation in China cools local land surface temperature, *Proceedings of the National Academy of Sciences of the United States of America*, *111*(8), 2915-2919, doi:10.1073/pnas.1315126111.

Pielke, R. A., et al. (2011), Land use/land cover changes and climate: modeling analysis and observational evidence, *Wiley Interdisciplinary Reviews: Climate Change*, *2*(6), 828-850, doi:10.1002/wcc.144.

Pitman, A. J., et al. (2009), Uncertainties in climate responses to past land cover change: First results from the LUCID intercomparison study, *Geophysical Research Letters*, *36*(14), doi:10.1029/2009gl039076.

Rienecker, M. M., et al. (2011), MERRA: NASA's Modern-Era Retrospective Analysis for Research and Applications, *Journal of Climate*, *24*(14), 3624-3648, doi:10.1175/jcli-d-11-00015.1.

Schaaf, C. B., et al. (2002), First operational BRDF, albedo nadir reflectance products from MODIS, *Remote Sensing of Environment, 83*, 135-148.

Schultz, N. M., P. J. Lawrence, and X. Lee (2017), Global satellite data highlights the diurnal aymettry of the effect of deforestation on local temperature, *Journal of Geophysical Research - Biogeosciences*.

Schultz, N. M., X. Lee, P. J. Lawrence, D. M. Lawrence, and L. Zhao (2016), Assessing the use of subgrid land model output to study impacts of land cover change, *Journal of Geophysical Research: Atmospheres*, *121*(11), 6133-6147, doi:10.1002/2016jd025094.

Swenson, S. C., and D. M. Lawrence (2014), Assessing a dry surface layer-based soil resistance parameterization for the Community Land Model using GRACE and FLUXNET-MTE data, *Journal of Geophysical Research: Atmospheres*, *119*(17), 10,299-210,312, doi:10.1002/2014jd022314.

Taylor, K. E. (2001), Summarizing multiple aspects of model performance in a single diagram, *Journal of Geophysical Research*, *106*(D7), 7183-7192.

Teuling, A. J., et al. (2010), Contrasting response of European forest and grassland energy exchange to heatwaves, *Nature Geoscience*, *3*(10), 722-727, doi:10.1038/ngeo950.

Vanden Broucke, S., S. Luyssaert, E. L. Davin, I. Janssens, and N. van Lipzig (2015), New insights in the capability of climate models to simulate the impact of LUC based on temperature decomposition of paired site observations, *Journal of Geophysical Research: Atmospheres*, *120*(11), 5417-5436, doi:10.1002/2015jd023095.

Viovy, N. (2011), http://dods.extra.cea.fr/store/p529viov/cruncep/V4_1901_2012/, edited.

Wan, Z. (2008), New refinements and validation of the MODIS Land-Surface Temperature/Emissivity products, *Remote Sensing of Environment*, *112*(1), 59-74, doi:10.1016/j.rse.2006.06.026.

Wickham, J. D., T. G. Wade, and K. H. Riitters (2012), Comparison of cropland and forest surface temperatures across the conterminous United States, *Agricultural and Forest Meteorology*, *166-167*, 137-143, doi:10.1016/j.agrformet.2012.07.002.

Zhang, M., et al. (2014), Response of surface air temperature to small-scale land clearing across latitudes, *Environmental Research Letters*, *9*(3), 034002, doi:10.1088/1748-9326/9/3/034002.

Zhao, L., X. Lee, R. B. Smith, and K. Oleson (2014), Strong contributions of local background climate to urban heat islands, *Nature*, *511*(7508), 216-219, doi:10.1038/nature13462.

Chapter 5: Conclusions & Future Work

This dissertation investigated the biophysical drivers of the day and nighttime surface temperature response to deforestation in the present climate, and developed a modeling framework by which to isolate the effects of land cover change in a global climate model and to evaluate a model's simulation of the biophysical effects of land cover change. A summary of the findings are as follows:

Chapter 2: Using global satellite observations, reanalysis data, and in-situ observations from flux towers, we examined the patterns and drivers of the day and nighttime surface temperature response to deforestation (ΔT_S). We found that a diurnal asymmetry exists in both the magnitude and sign of ΔT_S. In magnitude, ΔT_S is larger during the day than during the night over most regions of the world. The sign of ΔT_S changes from positive to negative from day to night, with most regions experiencing daytime warming and nighttime cooling. We found that daytime ΔT_S is driven by differences in absorbed shortwave radiation (ΔK_a) and the latent heat flux (ΔLE). The magnitude and spatial pattern of nighttime ΔT_S is related to the strength of the nocturnal temperature inversion, which is stronger in high latitudes and weaker in the tropics. Therefore, the roughness of forests is responsible for daytime cooling (removing heat from the surface) and nighttime warming (bringing warm air aloft down to the surface). Additionally, nighttime ΔT_S is related to the relative amount of heat stored in forests and open lands during the day.

Chapter 3: The sub-grid configuration of CLM4.5 was modified such that each PFT was assigned to an individual soil column. We compared this modified version to the default configuration, where all PFTs share one soil column, and examined the difference in sub-grid and grid-averaged surface air temperature and energy fluxes. Between the modified and default configurations, there were large differences in sub-grid output, but changes in the PFT-level data offset each other such that changes to grid-averaged values were minimal. We found that the sub-grid output from the default configuration produced erroneous ground heat fluxes, thus calling

into question other surface energy balance variables. We conclude that the modified configuration is better suited to the purposes of investigating the biophysical effects of land cover change, as each PFT is independent from the others both above and below-ground. Additionally, we show the value of sub-grid data for the assessment of PFT-level representation of land surface processes.

Chapter 4: In addition to evaluating model performance at the PFT-level, we also utilized the sub-grid differences in land surface climatology between PFTs as a metric of model performance. We found good agreement between satellite observations and PFT-level data; however, that agreement did not translate to an accurate representation of the climate response of the transition between two land cover types. Instead, the small biases in PFT-level data were compounded into larger errors when the difference between them was calculated. Additionally, the results show that it is important to evaluate the model at sub-daily scales, as the daily-mean obscured information about model biases during the day and night. In this analysis, the daytime and nighttime ΔT_S were overestimated and underestimated, respectively, producing reasonable results for the daily mean ΔT_S.

Future Work

We found that the grid-averaged values were insensitive to the soil column configuration (shared versus separated). This insensitivity may be an artifact of the offline configuration, where CLM4.5 was forced by prescribed atmospheric conditions. However, in a simulation where the land and atmosphere models are fully coupled, this may not be the case, and potential changes to precipitation and runoff may cause grid-averaged quantities to change. A preliminary investigation into the effect of sub-grid configuration in CLM-CAM simulation has been conducted (Appendix A); however, this investigation was primarily focused on the near-surface temperature response to sub-grid land cover change. More work is warranted to understand

whether the sub-grid configuration may affect grid-averaged values in coupled model simulations.

The modeling framework and performance evaluation presented in this dissertation has focused on local-scale land use and investigating the response of different land cover types to the same atmospheric conditions. Implicit in this framework was the assumption that the land cover changes are small enough to not trigger changes to atmospheric dynamics. However, land cover changes at a large enough scale may affect local and regional cloud and precipitation patterns. This feedback mechanism may not be triggered through coupled simulations of this sub-grid configuration, as no prescribed changes to the land surface map are occurring. However, future work will investigate the importance of spatial scale in land cover change experiments, specifically examining the scale at which these feedback mechanisms begin to occur.

Many land models represent the heterogeneous landscape through a sub-grid tiling scheme; however, these data are rarely utilized despite their potential value. In addition to the deforestation applications described in this dissertation, the sub-grid data may be utilized to understand processes related to agricultural expansion, urbanization, and the local impacts of climate change. Future examination of sub-grid data may also provide new insights into biogeochemical cycles (Appendix A), and the discrepancies between different models' representation of land use/land cover change. The sub-grid framework may be a particularly powerful tool to understand how the biophysical effects of land cover change compare to other large-scale forcings, like, for example, a doubling of atmospheric CO_2. Future work could investigate the relative impacts of land cover change and rising greenhouse gas concentrations on local climate, as well as the response of different land cover types to extreme events, such as heat waves or droughts.

Appendix A: The effect of sub-grid model scheme on the carbon cycle and coupled CLM-CAM simulations

Introduction

The sub-grid configuration of CLM4.5 has been shown to have significant effects on the PFT-level surface air temperature and energy fluxes, while having minimal effects on the grid-averaged variables [*Schultz et al.*, 2016]. Because PFT-level values are averaged to the grid-level before being passed to the atmosphere model, we expect that the sub-grid configuration (either shared PFT soil column or individual PFT soil columns) would not introduce unintended feedbacks into coupled CLM-CAM simulations. However, it is worthwhile to confirm that the modified sub-grid scheme (PFTCOL) may be used in coupled simulations without producing biased or erroneous results. Additionally, it is unknown how the PFTCOL configuration would affect the grid-averaged carbon variables, and if this sub-grid scheme would have a significant influence on the simulated global carbon budget, via change in carbon storage/fluxes in terrestrial ecosystems.

Here, I examine how the PFTCOL configuration performs for sub-grid land cover changes experiments in a coupled model environment. Additionally, I investigate the effect of the PFTCOL configuration on the terrestrial carbon cycle, through CLM4.5 simulations with the biogeochemistry module enabled.

Methods

CLM4.5 – CAM simulation

The experimental process here is similar to that described by *Schultz, N.M., et al.* [2016]. Briefly, two simulations were run using CLM4.5. In the first simulation (CTRL), the default sub-grid configuration of CLM4.5 was used, in that all PFTs shared the same soil column. The second simulation (PFTCOL) assigned each PFT to an individual soil column. In both simulations, the vegetation phenology was prescribed by satellite observations (CLM4.5-SP) [*Lawrence and Chase*, 2007]. The simulations were run at a horizontal resolution of 0.9^{o} lat x 1.25^{o} lon.

CLM4.5 was coupled to the Community Atmosphere Model (CAM5), the atmosphere model in CESM [*Neale et al.*, 2010]. The ocean and sea ice components of CESM were inactive, rather, were prescribed by data. Each simulation was run for 14 years using present-day (year 2000) forcings, with the first 10 years devoted to spin up time for the atmosphere model. Initial conditions were provided for CLM by previous 60-year spin ups for each of the sub-grid configurations. As the coupled simulations are computationally expensive, we ended the simulations after 4 years post-spin up. The sub-grid deforestation effect on air temperate (ΔT_a = T_a [grass PFTS] – T_a [forest PFTs]) was calculated for each of the CTRL and PFTCOL simulations. The results here were then compared to the offline sub-grid analysis by *Schultz et al.* [2016].

CLM4.5-BGC simulations

A similar paired-simulation approach was also used here to examine the effect of sub-grid configuration on terrestrial carbon fluxes and storage. Here, the CTRL and PFTCOL simulations were conducted using CLM4.5 enabled with the biogeochemistry module, rather than prescribing phenology with satellite data as in previous simulations. To get CLM4.5-BGC to steady state conditions, a much longer spin-up is required for each case than is required for CLM4.5-SP. Starting from arbitrary initial conditions, each case was run for 1000 years using the "accelerated decomposition (AD) spin up" mode. The AD spin up provided the initial conditions for the final spin up (200 years), cycling through the CRUNCEP data. The final spin up then provided the initial conditions for the experimental simulations: the effect of sub-grid configuration on carbon variables.

The experimental simulations were run for 10 years, 2001-2010, using the CRUNCEP atmospheric forcing data. Here, we compared the 10-year average of grid-averaged variables of gross primary productivity (GPP), net ecosystem production (NEP), net ecosystem exchange

(NEE) and total ecosystem carbon. Additionally, we estimate the change in global carbon fluxes and storage between the PFTCOL and CTRL cases.

Results

CLM4.5 – CAM

Figure A1 presents the sub-grid difference in 2m air temperature in both the CTRL and PFTCOL simulations. For reference, the offline CLM results are also shown here. The sub-grid ΔT_a patterns from the coupled simulation are very similar to the offline simulation. In the CTRL simulation, the zonal mean of sub-grid ΔT_a shows very little variability across latitudes, averaging between 0.05 to 0.5 K in most regions of the world. In contrast, the PFTCOL simulation shows a localized cooling in high latitudes and warming in mid-latitudes and the tropics. The zonal mean of the coupled PFTCOL simulation agrees very closely in sign and magnitude to the offline simulation. Although preliminary and brief, these results confirm the explanation that the sub-grid configuration does not introduce unexpected errors into the atmosphere model

CLM4.5-BGC

Figure A2 presents the 10-year average of GPP for the PFTCOL and CTRL simulations, as well as the difference between them. Here, the grid-averaged carbon flux values are shown for each simulation. Both the PFTCOL and CTRL simulations exhibit similar spatial patterns, with highest productivity occurring, as expected, in tropical regions. A comparison of the two simulations shows that in sub-tropical regions of South America and Africa, there are increases in GPP (up to 400-600+ gC m^{-2} yr^{-1}). However, because these increases in GPP are offset by decreases in GPP in other regions of the world, the global GPP is reduced in the PFTCOL simulation by 2.8 PgC or a percentage change of -2.15% (Table A1).

The sub-grid configuration also influences grid-averaged net ecosystem production (NEP), which excludes fire, land use, and the harvest flux (Figure A3). Positive values denote a grid as a

carbon sink, and vice versa as a carbon source. The difference between the two simulations shows no coherent spatial pattern, with the largest increases in the sink capacity of ecosystems occurring in the tropical regions in the PFTCOL case, up to 80 gC m^{-2} yr^{-1}. There is an increase in NEP of 0.26 PgC in the PFTCOL simulation at the global scale, a change of 7.70% from the CTRL case (Table A1).

Net ecosystem exchange, including fire, land use, and the harvest flux, for each of the two simulations is presented in Figure A4. A positive NEE means the grid is a carbon source. In both simulations, the general pattern of NEE is similar, with tropical forests acting as sinks and the central United States acting as a net carbon source. Comparing the two sub-grid schemes, there are differences between the two simulations, ranging from -50 to 50 gC m^{-2} yr^{-1}. However, there is no coherent spatial pattern to the resulting changes in NEE. At the global scale, the PFTCOL configuration increases the NEE by 1.7%. As expected, if NEE is increased by 1.7% in the PFTCOL simulation, the total ecosystem carbon decreases by the same amount (Table A1). The largest decreases are observed in latitudes north of 60°N, with some modest increases in the sub-tropics and boreal regions (Figure A5).

Summary

Here, I investigated whether the sub-grid configuration introduces any unintended feedbacks into a coupled model simulation, and examined the effect of sub-grid configuration on grid-averaged and global terrestrial carbon fluxes and storage. The ΔT_a pattern from the coupled simulations agreed very well with the offline results. Although the column configuration affects PFT-level variables, they are averaged to the grid-level before being passed to the atmosphere model. From our previous analysis, changes in PFTs offset each other such that the grid-averaged output from the PFTCOL simulation does not significantly differ from the CTRL case. That the patterns shown here are very similar to the offline simulation suggests that the PFTCOL configuration

may be successfully integrated into coupled simulations, and be used as a methodological tool to isolate the effects of land cover/land cover change from other forcings and feedbacks in climate model simulations.

The PFTCOL configuration affected grid-averaged carbon flux and storage values, but because the changes varied from positive to negative in different regions of the world, the effect on the global carbon budget was small. Therefore, the PFTCOL configuration would have negligible effect on atmospheric CO_2 concentrations, for example, if coupled to CAM. However, although we only present grid-averaged values here, it is clear that the PFTCOL configuration does influence the carbon balance of individual PFTs, in ways that as of now are not fully investigated. It would be worthwhile to dive deeper into this analysis, and to examine the PFT-level output to better understand why we observe the changes between the two simulations. Additionally, because the PFTCOL configuration is essentially a global expansion of single-point simulations, it may be a useful tool to test and understand the influence of new model schemes or parameterizations on modeled PFT-level or grid-averaged carbon cycles.

Tables

VARIABLE	PFTCOL	CTRL	PFTCOL-CTRL	% CHANGE
GPP (PgC/yr)	127.5	130.3	-2.8	-2.15%
NPP (PgC/yr)	57.4	57.9	-0.5	-0.86%
NEP (PgC/yr)	3.64	3.38	0.26	7.70%
NEE (PgC/yr)	-0.199	-0.169	0.03	1.70%
Ecosys C (PgC/yr)	5388.4	5482.1	-93.7	-1.70%

Table A1. The global estimates of carbon flux and storage variables from the PFTCOL and CTRL simulations. Also shown are the absolute difference and % change between the two sub-grid configurations.

Figures

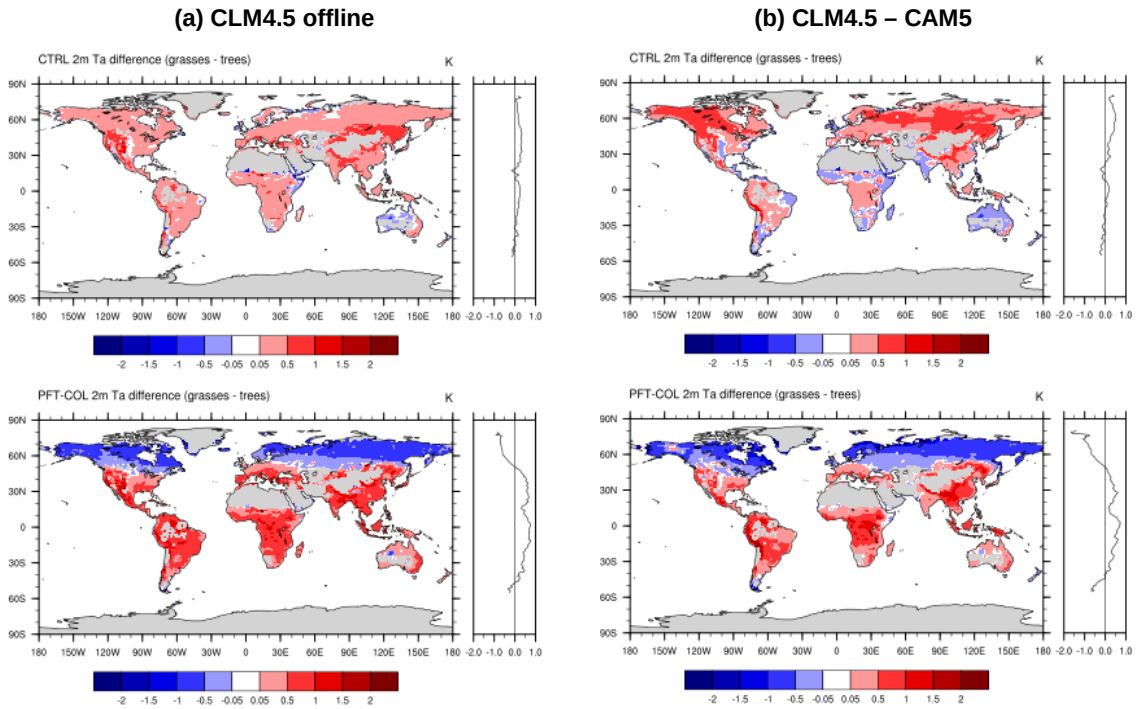

Figure A1. The sub-grid surface temperature difference between grass and tree PFTs in (a) offline CLM4.5 (reproduced from *Schultz et al.* [2016]), and (b) CLM4.5 – CAM5. The top and bottom panels show the CTRL and PFTCOL configurations, respectively.

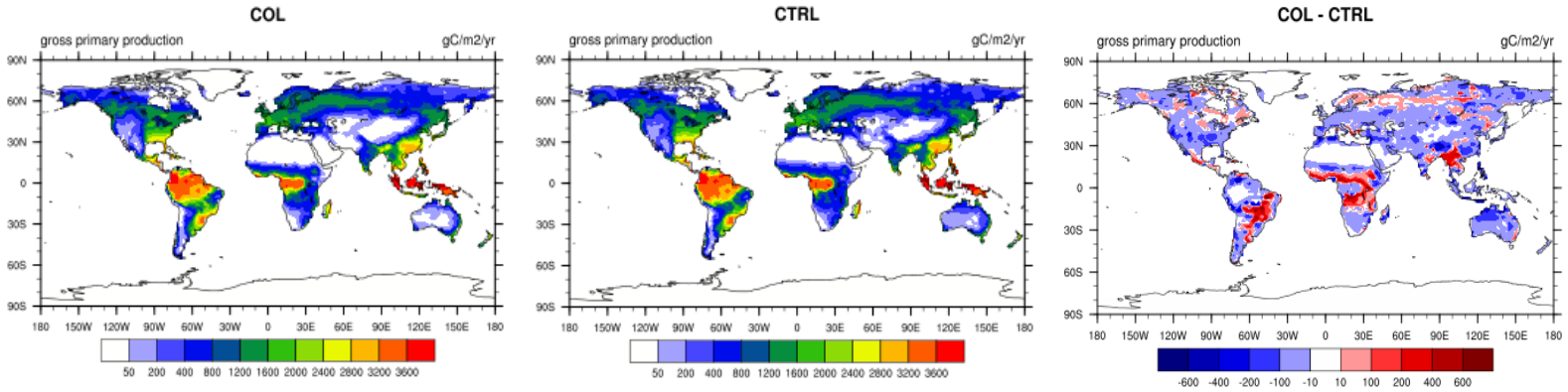

Figure A2. The 10-year average of GPP for the PFTCOL (COL) and CTRL simulations, and the difference in GPP between them.

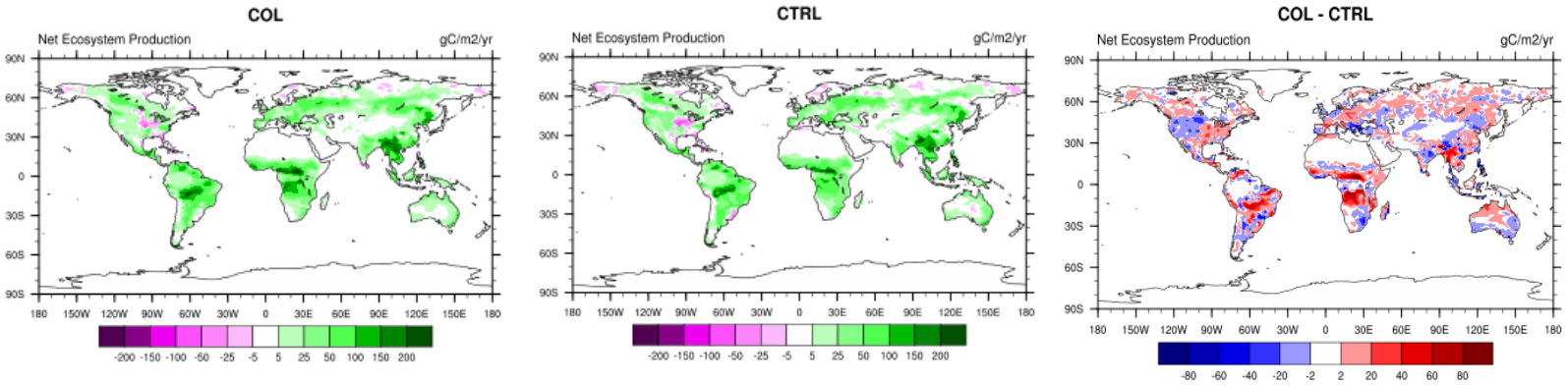

Figure A3. The 10-year average of NEP for the PFTCOL (COL) and CTRL simulations, and the difference in GPP between them.

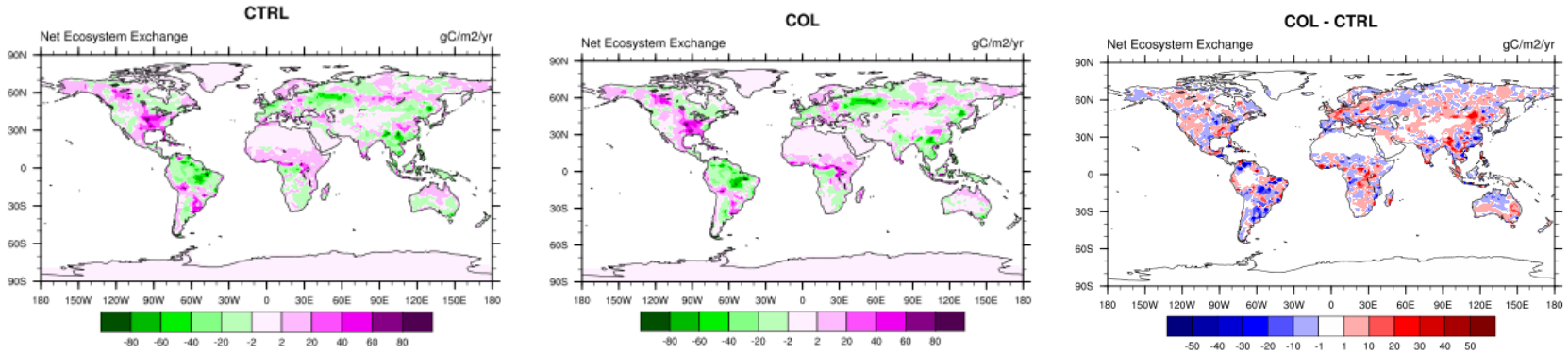

Figure A4. The 10-year average of NEE for the PFTCOL (COL) and CTRL simulations, and the difference in GPP between them.

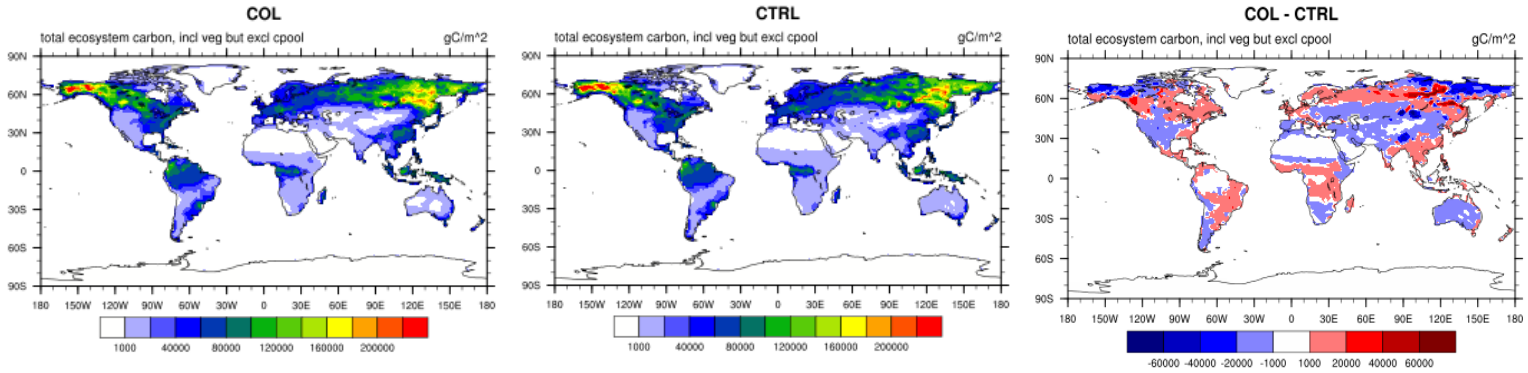

Figure A5. The 10-year average of total ecosystem carbon for the PFTCOL (COL) and CTRL simulations, and the difference in GPP between them.

References

Lawrence, P. J., and T. N. Chase (2007), Representing a new MODIS consistent land surface in the Community Land Model (CLM 3.0), *Journal of Geophysical Research, 112*(G1), doi:10.1029/2006jg000168.

Neale, R. B., A. Gettelman, S. Park, C.-C. Chen, P. H. Lauritzen, and D. L. Williamson (2010), Description of the NCAR Community Atmosphere Model (CAM 5.0)*Rep.*

Schultz, N. M., X. Lee, P. J. Lawrence, D. M. Lawrence, and L. Zhao (2016), Assessing the use of subgrid land model output to study impacts of land cover change, *Journal of Geophysical Research: Atmospheres*, *121*(11), 6133-6147, doi:10.1002/2016jd025094.